Signal Processing for Wireless Power and Information Transfer

Shan Zhong

Submitted in partial fulfillment of the
requirements for the degree
of Doctor of Philosophy
in the Graduate School of Arts and Sciences

COLUMBIA UNIVERSITY

2019

ABSTRACT

Signal Processing for Wireless Power and Information Transfer

Shan Zhong

The rapid development of the Internet of Things (IoT) and wireless sensor network (WSN) technologies enable easy access and control of a variety forms of information and data from numerous number of smart devices, and give rise to many novel applications and research areas such as smart home, machine type communications, etc. However due to the small sizes, sophisticated environment, and large number of devices in network, it is hard to directly power the devices from grid. Hence the power connectivity remains one of the major issues that needs to be addressed for related IoT applications. Wireless power transfer (WPT) and backscatter communications are provisioned to be prominent solutions to overcome the power connectivity challenge, but they suffer strong efficiency limitation which becomes the barrier to universally popularize such technologies. On the other hand, network optimization is also a research focus of such applications which significantly affects the performance of the system due to the high volume of connected devices and different features.

In this thesis we propose advanced techniques to overcome the challenges on the low efficiency and network design of the wireless information and power transfer systems. The thesis consists of two parts. In the first part we focus on the power transmitter design which addresses the low efficiency issue associated with backscatter communication and WPT. In Chapter 2, we consider a backscatter RFID system with the multi-antenna reader and propose a blind transmit and receive adaptive beamforming algorithm. The interrogation range and data transmission performance

are both investigated under such configuration. In Chapter 3 we study wireless power transfer by the beamspace large-scale MIMO system with lens antenna arrays. We first present the WPT model for the beamspace MIMO which is derived from the spatial MIMO model. By constraining on the number of RF chains in the transmitter, we formulate two WPT optimization problems: the sum power transfer problem and the max-min power transfer problem. For both problems we consider two different transmission schemes, the multi-stream and uni-stream transmissions, and we propose different algorithms to solve both problems in both schemes respectively.

In the second part we study the network optimization problems in the WPT and backscatter systems. In Chapter 4, we study the resource allocation problem for a RF-powered network, where the objective is to maximize the total data throughput of all sensors. We break the problem into two subproblems: the sensor battery energy utilization problem and the charging power allocation problem of the central node, which is an RF power transmitter that transmits RF power to the sensors. We analyze and show several key properties of both problems, and then propose computationally efficient algorithms to solve both problems optimally. In Chapter 5, we study the time scheduling problem in RF-powered backscatter communication networks, where all transmitters can operates in either backscattering mode or harvest-then-transmit (HTT) mode. The objective is to decide the operating mode of each transmitter and minimize the total transmission time of the network. We also consider both ideal and realistic transmitters based on different internal power consumption models for HTT transmitters. Under both transmitter models we show several key properties, and propose bisection based algorithms which has low computational complexity that solves the problem optimally. The results are then extended to the massive MIMO regime.

Table of Contents

List of Figures

List of Tables

Acknowledgments

First of all, I would like to express my most sincere gratitude to my advisor Prof. Xiaodong Wang, who made this thesis possible. His generous advices and strong support have guided me throughout my Ph.D. studies, and will continue to inspire me for my future career.

I also thank the thesis committee, Prof. Javad Ghaderi, Prof. Xiaofan Fred Jiang, Dr. Guido Hugo Jajamovich and Dr. Jinfeng Du for taking time to read and evaluate this thesis.

My thanks also extend to the colleagues, Dr. Ju Sun, Dr. Shang Li, Dr. Mehdi Ashraphijuo, among many others, with whom I spent precious and memorable time at Columbia University. Thank them for their friendship and kind support that filled my Ph.D. career with happy moments.

Last but not least, I owe special thanks to my beloved parents and family. It is their unconditional support that gives me the courage to walk through this journey. My gratitude and love for them are beyond words.

To my family

Chapter 1

Introduction

1.1 Background and Motivation

In the past decade, we have witnessed the rapid development of the Internet of Things (IoT) and wireless sensor network (WSN). These technologies enable easy access and control of a verity forms of information and data from numerous number of smart devices, and give rise to many novel applications and research areas such as smart home, machine type communications (MTC), etc. In fact, IoT has been recognized as one of the key applications for 5G communications, and many efforts have been made to standardize the communication interface within the Third-Generation Partnership Project and using long-term evolution (LTE) bands to address the requirements of the IoT, e.g., narrowband (NB) IoT [1]. The advantages of the IoT technology include improved coverage, support of massive number of devices, low latency, low device cost and power consumption, and optimized network architecture.

However, the new opportunity is accompanied by challenges. Due to the small sizes, sophisticated environment, and large number of devices in network, it is hard to directly power the devices from grid. Using batteries is an alternative solution, but battery recharging or replacement has the same limitations since it still requires connection to the grid, and replacing them manually can be even more problematic.

Hence the power connectivity is one of the major issues that needs to be addressed for related IoT applications.

One solution is to employ wireless power transfer (WPT) technique with radio-frequency (RF) energy harvesting transmitters. RF energy harvesting transmitters mainly consist of an energy harvesting module, an energy storage module, and a communication module, as shown in Fig. 1.1. They harvest incoming RF energy to support its internal operation in the self-sustainable way, without access to external power source. WPT has become an active research area as the technology has been provisioned to replace the traditional wired power transfer in many applications [2]. For example, WPT is able to extend the battery lifetime of energy constrained wireless sensor nodes [3] in applications such as health monitoring of patients, aircraft structural monitoring, and hazardous environment monitoring. On the other hand, WPT can also be employed to charge low power devices such as thermometers, motion sensors, and displays [4]. Even small-scale computation, sensing and communications can be powered by WPT [5]. It can be clearly seen that WPT will potentially play a significant role in IoT applications by eliminating the connecting wires, leading to higher degrees of freedom in the placement of IoT devices.

Another solution is to employ the backscatter communication technique. A backscatter system typically consists of a reader (a.k.a. interrogators), backscatter transmitters (a.k.a. transponders or tags) and data processing module. The universally used radio frequency identification (RFID) system is a practical example of backscatter system. Rather than transmitting information and data signals actively, the backscatter transmitters convey information by modulating then reflecting back the incoming signals passively from the reader, as illustrated in Fig. 1.2. In this case the transmitter features low cost and simple structure since batteries are eliminated, and latency is low due to its reflecting mechanism. Hence the backscatter system has been wildly used in many applications such as supply chain, logistics, asset tracking, etc [6–9]. Currently studies on backscatter communication have emerged, and new system archi-

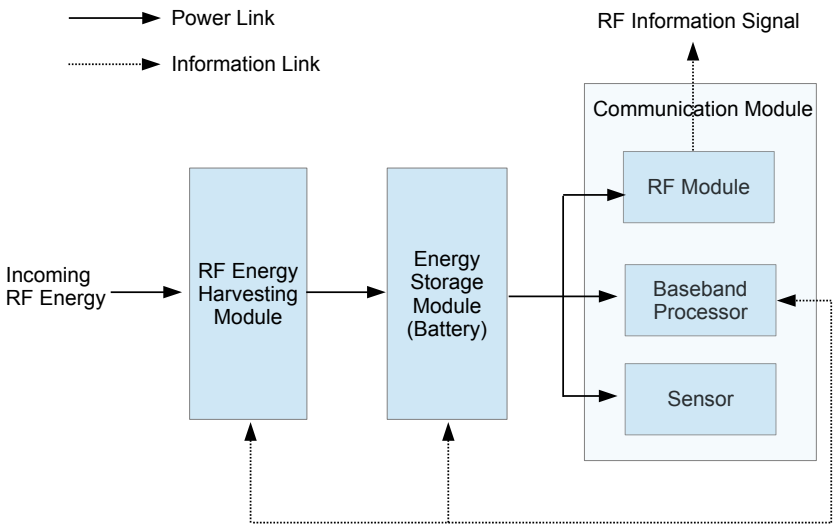

Figure 1.1: System architecture of energy harvesting transmitters.

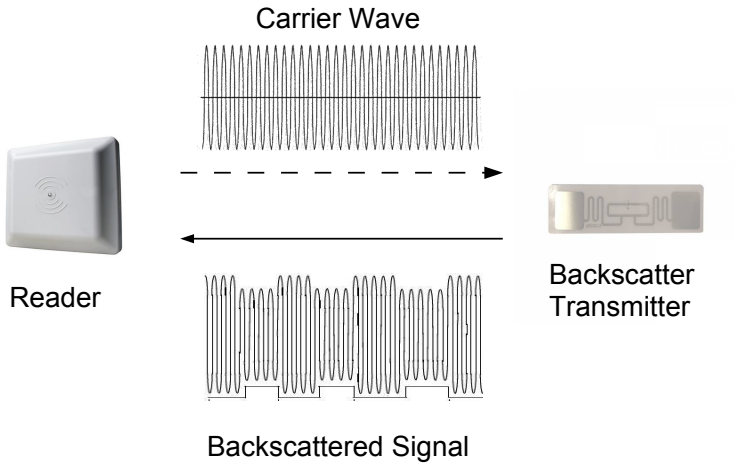

Figure 1.2: Flow diagram of backscatter communication.

tecture has been proposed such as ambient backscattering[10, 11], LoRa backscatter [12], etc.

It can be seen that both wireless power transfer and backscatter communication are prominent solutions to address the power connectivity issue and each method has unique features. WPT method is more flexible and does not require a reader to constantly provide carrier wave during its operation, while the backscatter system requires lower device cost and simple structure, and its delay is low. However, both methods suffer strong path loss and low efficiency. In WPT applications the low efficiency leads to high input power consumption and severely restricts the coverage range [13]. Similarly, in backscatter systems the interrogation range and reliability are capped. Therefore, it is clear that the low efficiency issue is the bottleneck and it strongly limits the performance of these techniques, which needs to be addressed before the popularization of the related applications. On the other hand, due to the high volume of the connected devices, the network architecture and design strongly affect the performance of the system. Hence, network optimization is also an important topic and active research area in all kinds of IoT applications [14–21].

1.2 Outline and Contributions

Motivated by the tremendously rising demand of WPT and backscatter applications, in this thesis we will present advanced techniques to overcome the challenges on the low efficiency and network design. The thesis consists of two parts. In the first part we focus on the power transmitter design which addresses the low efficiency issue associated with backscatter communication and WPT. In the second part we focus on the network optimization problems for WPT and backscatter based systems.

1.2.1 Multi-Antenna Transmitter Design for Backscatter Communication and Wireless Power Transfer

Multiple-input multiple-output (MIMO) system has been proven to be one of the key inventions in the past two decades in wireless communications. It has become an

essential element in wireless communication standards including 3G, 4G, 5G, WiFi, etc. With beamforming, MIMO system can enhance the performance of signal transmission to achieve higher transmission capacity. In this thesis, we employ the MIMO beamforming to improve the energy transmission efficiency and overcome the limitation on power delivery distances.

In Chapter 2, we consider a backscatter RFID system with the multi-antenna reader, whereas each tag has a single antenna. The interrogation range and data transmission performance are both investigated under such configuration. A blind transmit and receive adaptive beamforming algorithm is proposed. Following the basic idea in [22], a tag quantity estimator is proposed. Multiple antennas are shown to improve the estimation performance. Simulation results illustrate that without increasing the total transmit power, the interrogation range and the data transmission performance are significantly improved thanks to multiple antennas and efficient beamforming. Readers with the proposed simple adaptive beamforming scheme is able to reach reading distances close to readers with optimal beamforming, and makes the data transmission performance near-optimal even without channel estimation. A multiple-antenna half-duplex reader prototype is implemented using USRP platform. Experimental results demonstrate the interrogation range improvement over a single-antenna reader and especially the proposed blind adaptive beamforming scheme outperforms other traditional beamforming schemes.

In Chapter 3 we study wireless power transfer by the beamspace large-scale MIMO system with lens antenna arrays. We first present the WPT model for the beamspace MIMO which is derived from the spatial MIMO model. By constraining on the number of RF chains in the transmitter, we formulate two WPT optimization problems: the sum power transfer problem and the max-min power transfer problem. For both problems we consider two different transmission schemes, the multi-stream and uni-stream transmissions. For the sum power transfer problem, We theoretically show that the uni-stream scheme can achieve the same performance as the multi-stream

counterpart, and propose two algorithms for the uni-stream power transfer. For the max-min power transfer problem, we present a semidefinite relaxation (SDR)-based greedy algorithm and a Riemannian conjugate gradient algorithm for the multi-stream and uni-stream case respectively.

1.2.2 Network Optimization for Wireless Power Transfer and Backscatter Communication Systems

In the second part of the thesis we study the WPT and backscatter system from the network point of view. In Chapter 4, we study the resource allocation problem for a RF-powered network. In this network there is a central node and multiple RF powered sensor devices. The central node is an RF power transmitter (charger), and it transmits RF power to the sensors. Each sensor is equipped with a battery. The sensors harvest the RF power from the central node, and stores the energy in their batteries. On the other hand, the sensors utilize the energy stored in their batteries to transmit data to the central node. The objective is to maximize the total data throughput of all sensors, and we break the problem into two subproblems: the sensor battery energy utilization problem and the charging power allocation problem of the central node. We formulate the sensor energy utilization problem as a finite-horizon Markov decision process (MDP) problem. We show several important properties of the value function based on which we propose an optimal energy utilization algorithm with reduced search space of possible actions. We show that the total value function of the sensors under a given power allocation satisfies the M-EXC property [98]. We then propose an optimal power allocation algorithm based on the discrete steepest ascent method that has a significantly lower complexity than exhaustive search.

In Chapter 5, we study the time scheduling problem in RF-powered backscatter communication networks. We consider a system network with one single-antenna reader and multiple RF powered backscatter transmitters. The transmitters can operates in either backscattering mode or harvest-then-transmit (HTT) mode, and

the reader acts as a power transmitter and information receiver and supports both operating modes. The objective is to decide the operating mode of each transmitter and minimize the total transmission time of the network. We consider the ideal transmitters where it is assumed that no power is required for non transmission-related operations in the HTT mode, such as coding, baseband processing etc. We also consider practical transmitters under realistic power consumption model. Under both transmitter models we show several key properties, and show that the optimal transmission time of each transmitter can be calculated, and their optimal operating modes can be found by using a bisection based algorithm which has significantly lower complexity than that the exhaustive search method. We then extend the result to the massive MIMO regime, and propose an algorithm to solve the corresponding problems in linear time complexity.

Part I

Multi-Antenna Transmitter Design for Backscatter Communication and Wireless Power Transfer

Chapter 2

Multi-Antenna Backscatter Reader Design with Blind Adaptive Beamforming

2.1 Introduction

In this chapter, we consider a backscatter radio frequency identification (RFID) system with the reader equipped with multiple antennas, and design a blind adaptive beamforming algorithm which cooperates well with the existing protocol. Specifically, we consider the ultra-high frequency (UHF) RFID, which operates in the frequency range of 860-960 MHz. As an example of backscatter communication, in passive UHF RFID systems, tags absorb energy from the RF field generated by the signals transmitted by the reader to be powered up. Therefore, tags (backscatter transmitters) feature rather low cost and small size. However, the interrogation range and read reliability of the passive UHF RFID system are limited due to the lack of built-in power source of the tag, especially in fading environments.

Several works have addressed the issue of interrogation range or transmission performance improvement of passive UHF RFID with single antenna [23, 24] and with

multiple antennas [25–29]. In particular, in [25], the reverse link interrogation range of the UHF RFID is increased by employing multiple antennas at the reader, where maximal ratio combining (MRC) is adopted to achieve the optimal range improvement. Note that MRC requires the channel state information (CSI), so channel estimation should be performed before applying MRC. If the distance between the reader and tag is the maximum range that can be achieved by applying MRC, since at the beginning the reader cannot apply MRC due to the lack of CSI, the delivered power from the reader may not be sufficient to power up the tag. If the tag is not powered up, channel estimation cannot be performed and hence MRC cannot be applied. In [26], multiple RF antennas are equipped at the tag while the reader has single antenna. However, tags are supposed to be as simple and low-cost as possible, so employing multiple antennas at the tag may not be practically feasible. Bistatic RFID is considered in [29] where the reader employs multiple receive antennas and the multi-antenna receiver algorithm requires complex processing and channel estimation. Several works have discussed the feasibility of MIMO RFID systems, [27] and [28] present channel estimation methods for the MIMO RFID systems, but they also contradict to the simple and low-cost feature. However, none of the works mentioned above provides any practical solutions for improving the interrogation range that comply with existing RFID standards.

Within the interrogation zone of a reader, there may exist many tags, which are ready to communicate with the reader. The slotted ALOHA [30–33] protocol is widely used in current RFID systems for multiple access. It is known that the throughput is maximized if the frame size is set equal to the number of tags in the range. But the number of tags is unknown to the reader at the beginning, this motivates the estimation of the number of tags in the interrogation range of the reader [22, 34, 35].

In this chapter, we consider an RFID system with the reader equipped with multiple antennas, whereas each tag has a single antenna, which is an effective way to reduce the overall cost, since for typical RFID applications such as objects identifi-

cation in warehouses, there are usually hundreds or thousands of tags. The interrogation range and data transmission performance are both investigated under the new configuration. A blind transmit and receive adaptive beamforming algorithm is proposed. Following the basic idea in [22], a tag quantity estimator is proposed. Multiple antennas are shown to improve the estimation performance. Simulation results illustrate that without increasing the total transmit power, the interrogation range and the data transmission performance are significantly improved thanks to multiple antennas and efficient beamforming. Readers with the proposed simple adaptive beamforming scheme is able to reach reading distances close to readers with optimal beamforming, and makes the data transmission performance near-optimal even without channel estimation. A multiple-antenna half-duplex reader prototype is implemented using USRP. Experimental results demonstrate the interrogation range improvement over a single-antenna reader and especially the proposed blind adaptive beamforming scheme outperforms other traditional beamforming schemes.

2.2 Reader Interrogation Range

An RFID system mainly consists of a reader and a set of tags. The block diagram of the system is shown in Fig. 2.1(a), where M transmit/receive antennas are employed at the reader whereas each tag has a single antenna. In Fig. 2.1(a) the transmitter and receiver use a common set of antennas, which is referred to as a full-duplex reader, and the transmitter and receiver are connected via a circulator or a coupler [6]. On the other hand, if different sets of antennas are employed for transmitting and receiving, it is referred to as a half-duplex reader, shown in Fig 2.1(b).

For a full-duplex reader, we assume that the forward link and the corresponding reverse link observe the same channel coefficients (see Fig. 2.1(a)). On the other hand, for a half-duplex reader, forward and reverse links observe independent channel coefficients.

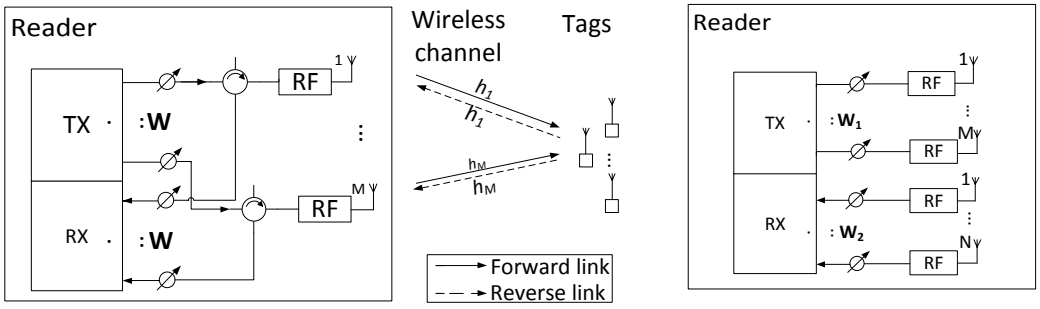

(a) (b)

Figure 2.1: (a) A passive full-duplex multiple-antenna UHF RFID system and (b) a half-duplex reader.

Before analyzing the interrogation range of the multiple-antenna RFID system, we first consider the single-antenna case.

2.2.1 Single-antenna Case

We first consider the full-duplex case. At the very beginning, the reader transmits a continuous wave (CW) to power up the passive tag in the forward link. The received power by a tag can be written as

$$P_{RX}^{tag}(d) = P_{TX} G_r G_t P_L(d) |h|^2, \tag{2.1}$$

where P_{TX} is the transmit power of the reader, G_r is the reader antenna gain, G_t is the tag antenna gain, h is the channel coefficient, $P_L(d)$ is the path loss given by

$$P_L(d) = \left(\frac{\lambda}{4\pi d}\right)^2, \tag{2.2}$$

where λ is the wavelength of the carrier and d is the distance between the reader and the tag.

In order to activate the tag, the received signal power at the tag should be no less

than the tag sensitivity P_{TS}, i.e.,

$$P_{TX}G_rG_tP_L(d)\left|h\right|^2 \geq P_{TS}, \tag{2.3}$$

which is the constraint of the forward link.

In the reverse link, after the tag is powered up, it scatters the signal back to the reader by modulating the received CW. The backscattered power received by the reader is given by

$$\begin{aligned} P_{RX}^{reader}(d) &= \eta P_{RX}^{tag}(d)\, G_rG_tP_L(d)\left|h\right|^2 \\ &= \eta P_{TX}G_r^2G_t^2P_L^2(d)\left|h\right|^4, \end{aligned} \tag{2.4}$$

where η is the backscattering modulation efficiency of the tag.

In order to successfully demodulate the backscattered signal, the received backscattered power should be no less than the reader sensitivity P_{RS}, i.e.,

$$\eta P_{TX}G_r^2G_t^2P_L^2(d)\left|h\right|^4 \geq P_{RS}, \tag{2.5}$$

which is the constraint of the reverse link.

It is clear that both constraints (2.3) and (2.5) should be satisfied to determine the reader interrogation range d. From (2.3) and (2.5), we have

$$P_L(d) \geq \left(P_{TX}G_rG_t\left|h\right|^2\right)^{-1} P_{TS} \tag{2.6}$$

$$\text{and} \quad P_L(d) \geq \left(\sqrt{\eta P_{TX}}G_rG_t\left|h\right|^2\right)^{-1}\sqrt{P_{RS}}. \tag{2.7}$$

Denote $\alpha \triangleq \left(P_{TX}G_rG_t\left|h\right|^2\right)^{-1} P_{TS}$, $\beta \triangleq \left(\sqrt{\eta P_{TX}}G_rG_t\left|h\right|^2\right)^{-1}\sqrt{P_{RS}}$, and

$$\delta \triangleq \alpha/\beta = \left(P_{TX}P_{RS}\right)^{-\frac{1}{2}}\sqrt{\eta}P_{TS}. \tag{2.8}$$

If $\delta > 1$, we have $\alpha > \beta$, so once (2.6) is satisfied, (2.7) is always satisfied. In this case, the system is forward-link-limited (FLL) which means the interrogation range is the forward link range determined by (2.6). From $\delta > 1$ and (2.8), it can be easily derived that $P_{TS} > \sqrt{\eta^{-1}P_{TX}P_{RS}}$. The interrogation range is determined by (2.6).

By substituting (2.2) into (2.6), we have $(\lambda/4\pi d)^2 \geq \left(P_{TX}G_rG_t\left|h\right|^2\right)^{-1} P_{TS}$, so it follows that the maximum interrogation range is

$$d^{FLL} = \sqrt{\left(16\pi^2 P_{TS}\right)^{-1} P_{TX}G_rG_t\lambda^2\left|h\right|^2}. \tag{2.9}$$

If $\delta < 1$, we have $\alpha < \beta$. In this case, the system is reverse-link-limited (RLL) which means the interrogation range is determined by the reverse link range. From $\delta < 1$ and (2.8), it can be easily derived that $P_{TS} < \sqrt{\eta^{-1}P_{TX}P_{RS}}$. The interrogation range is determined by (2.7). By substituting (2.2) into (2.7), we have $(\lambda/4\pi d)^2 \geq \left(\sqrt{\eta P_{TX}}G_rG_t\left|h\right|^2\right)^{-1}\sqrt{P_{RS}}$, so it follows that the maximum interrogation range is

$$d^{RLL} = \sqrt{\left(16\pi^2\sqrt{P_{RS}}\right)^{-1}\sqrt{\eta P_{TX}}G_rG_t\lambda^2\left|h\right|^2}. \tag{2.10}$$

For half-duplex readers, the forward and reverse links observe different channel gains h_1 and h_2 respectively. The forward-link-limited and reverse-link-limited maximum interrogation ranges are

$$d^{FLL} = \sqrt{\left(16\pi^2 P_{TS}\right)^{-1} P_{TX}G_rG_t\lambda^2\left|h_1\right|^2} \tag{2.11}$$

and

$$d^{RLL} = \sqrt{\left(16\pi^2\sqrt{P_{RS}}\right)^{-1}\sqrt{\eta P_{TX}}G_rG_t\lambda^2\left|h_1\right|\left|h_2\right|}, \tag{2.12}$$

respectively, under the assumption that the distance from the transmitter antenna to the tag and that from the tag to the receiver antenna are identical, which holds in practice when antennas are placed next to each other and the tag is relatively far from the antennas.

2.2.2 Multiple-antenna Case

Under full-duplex configuration, in the forward link, for the multiple-antenna case, the received power at the tag is given by

$$P_{RX}^{tag}(d) = P_{TX}G_rG_tP_L(d)\left|\mathbf{w}^H\mathbf{h}\right|^2, \tag{2.13}$$

where $\mathbf{h} = [h_1, \ldots h_M]^T$ is channel vector with h_i being the channel coefficient from the ith reader antenna to the tag antenna, M is the number of antennas, $\mathbf{w} = [w_1, \ldots, w_M]^T$ is the antenna weight vector, i.e., beamformer, with $\|\mathbf{w}\| = 1$. Thus the constraint of the forward link with multiple-antenna configuration can be expressed as

$$P_{TX} G_r G_t P_L(d) \left|\mathbf{w}^H \mathbf{h}\right|^2 \geq P_{TS}. \tag{2.14}$$

In the reverse link, the received backscattered power at the reader is given by

$$\begin{aligned} P_{RX}^{reader}(d) &= \eta P_{RX}^{tag}(d) G_r G_t P_L(d) \left|\mathbf{w}^H \mathbf{h}\right|^2 \\ &= \eta P_{TX} G_r^2 G_t^2 P_L^2(d) \left|\mathbf{w}^H \mathbf{h}\right|^4. \end{aligned} \tag{2.15}$$

So we have the constraint of the reverse link for the multiple-antenna case as

$$\eta P_{TX} G_r^2 G_t^2 P_L^2(d) \left|\mathbf{w}^H \mathbf{h}\right|^4 \geq P_{RS}. \tag{2.16}$$

Similar to the single-antenna case, we have that the system is forward-link-limited if $P_{TS} > \sqrt{\eta^{-1} P_{TX} P_{RS}}$, with the corresponding maximum interrogation range

$$d_{MA}^{FLL} = \sqrt{\left(16\pi^2 P_{TS}\right)^{-1} P_{TX} G_r G_t \lambda^2 \left|\mathbf{w}^H \mathbf{h}\right|^2}. \tag{2.17}$$

And the system is reverse-link-limited if $P_{TS} < \sqrt{\eta^{-1} P_{TX} P_{RS}}$, with the corresponding maximum interrogation range

$$d_{MA}^{RLL} = \sqrt{\left(16\pi^2 \sqrt{P_{RS}}\right)^{-1} \sqrt{\eta P_{TX}} G_r G_t \lambda^2 \left|\mathbf{w}^H \mathbf{h}\right|^2}. \tag{2.18}$$

From (2.9), (2.10), (2.17), and (2.18), it can be derived that the interrogation range gain of the multiple-antenna case over the single-antenna case is $\frac{\left|\mathbf{w}^H \mathbf{h}\right|}{|h|}$ for both FLL and RLL systems. Similarly, the maximum interrogation ranges for half-duplex systems are

$$d_{MA}^{FLL} = \sqrt{\left(16\pi^2 P_{TS}\right)^{-1} P_{TX} G_r G_t \lambda^2 \left|\mathbf{w}_1^H \mathbf{h}_1\right|^2} \tag{2.19}$$

and

$$d_{MA}^{RLL} = \sqrt{\left(16\pi^2 \sqrt{P_{RS}}\right)^{-1} \sqrt{\eta P_{TX}} G_r G_t \lambda^2 \left|\mathbf{w}_1^H \mathbf{h}_1\right| \left|\mathbf{w}_2^H \mathbf{h}_2\right|} \tag{2.20}$$

respectively, where $\mathbf{w}_1$ and $\mathbf{w}_2$ are antenna weights for the transmitter and receiver, respectively.

The proper choice of the antenna weights $\mathbf{w}$ or $(\mathbf{w}_1, \mathbf{w}_2)$ increases the interrogation range. There are several beamforming schemes in common use: equal-weight beamforming (EBF), random beamforming (RBF), and optimal beamforming (OBF). For EBF, the weight vectors are a normalized all-one vector i.e., $\mathbf{w} = \mathbf{w}_1 = \mathbf{w}_2 = \frac{1}{\sqrt{M}}[1, \cdots, 1]^T$ where M is the number of antennas. For RBF, the weight vectors are generated randomly following certain distribution and then normalized, e.g., $\tilde{\mathbf{w}} \sim \mathcal{N}_c(\mathbf{0}, \mathbf{I}_M)$, $\mathbf{w} = \tilde{\mathbf{w}}/\|\tilde{\mathbf{w}}\|$. Both EBF and RBF are simple to implement, but their performances may be far from the optimum since they do not make use of the channel state information $\mathbf{h}$ or $(\mathbf{h}_1, \mathbf{h}_2)$. On the other hand, the optimal beamformers are channel-matched, i.e., the OBF is given by $\mathbf{w} = \mathbf{h}/\left\|\mathbf{h}\right\|$ for full-duplex and $\mathbf{w}_1 = \mathbf{h}_1/\left\|\mathbf{h}_1\right\|, \mathbf{w}_2 = \mathbf{h}_2/\left\|\mathbf{h}_2\right\|$ for half-duplex. Therefore, the OBF requires perfect knowledge of the channel state which is unavailable at the reader at the startup of the system but is typically obtained by estimating the channel based on the reply signal from the tag. In other words, the tag must have been powered up before the reader is about to estimate the channel. In this sense, it is clear that there is no need to estimate the channel in order to improve the interrogation range since the tag has been powered up and the distance between the reader and tag has been physically determined. Moreover, introducing the channel estimation functionality will significantly increase the complexity of the RFID system. In next section, we propose a blind adaptive beamforming (BABF) technique [36, 37] that exploits the channel state information but does not perform explicit channel estimation.

Algorithm 2.1 - Blind adaptive beamforming algorithm for full-duplex systems

1: Initialize $n = 0$ and $\mathbf{w}^{(0)} \sim \mathcal{N}_c(\mathbf{0}, \mathbf{I}_M)$;

Repeat

2: $n = n + 1$;

3: Generate K_p perturbation vectors $\mathbf{p}_i \sim \mathcal{N}_c(\mathbf{0}, \mathbf{I})$, $i = 1, \ldots, K_p$;

4: Form K_p new weight vectors $\tilde{\mathbf{w}}_i = \frac{\mathbf{w}^{(n-1)} + \beta \mathbf{p}_i}{\left\| \mathbf{w}^{(n-1)} + \beta \mathbf{p}_i \right\|}$, $i = 1, \ldots, K_p$;

5: Measure the received power $P_{RX,i}^{reader} = \eta P_{TX} G_r^2 G_t^2 P_L^2 \left| \tilde{\mathbf{w}}_i^H \mathbf{h} \right|^4$, $i = 1, \ldots, K_p$;

6: Update $\mathbf{w}^{(n)} = \tilde{\mathbf{w}}_I$, where $I = \arg \max_i P_{RX,i}^{reader}$;

7: **Until** $\left| P_{RX}^{reader} \left(\mathbf{w}^{(n)} \right) - P_{RX}^{reader} \left(\mathbf{w}^{(n-1)} \right) \right| < \varepsilon$, where ε is the threshold.

2.3 Blind Adaptive Beamforming for RFID Reader

2.3.1 Full-duplex Reader

The goal for the BABF algorithm is to find the antenna weight vector that enables the reader to probe the tags at a given distance, and maximizes the received backscattered power from the tag. In full-duplex systems, the BABF scheme starts by sending the CW from the reader for *probing* the tag, i.e., evaluating the backscattered power from the tag. At the nth iteration, given the weight vector $\mathbf{w}^{(n-1)}$, K_p perturbation vectors $\mathbf{p}_i$ are generated where $\mathbf{p}_i \sim \mathcal{N}_c(\mathbf{0}, \mathbf{I}_M)$, $i = 1, \ldots, K_p$ to form K_p new weight vectors

$$\tilde{\mathbf{w}}_i \Leftarrow \frac{\mathbf{w}^{(n-1)} + \beta \mathbf{p}_i}{\left\| \mathbf{w}^{(n-1)} + \beta \mathbf{p}_i \right\|}, \quad i = 1, \ldots, K_p \tag{2.21}$$

where β is the weight adaptation step size. Then for each of these K_p generated weight vectors, the corresponding received backscattered power (2.15) is measured at the reader. Finally, the weight vector is updated as the one that has the largest backscattered power among the K_p vectors in (2.21). The iteration terminates when the received backscattered power fluctuates below a tolerance threshold. The algorithm is summarized as Alg. 2.1.

Algorithm 2.2 - Blind adaptive beamforming algorithm for $M \times N$ half-duplex systems

1: Initialize $n \Leftarrow 0$ and $\mathbf{w}^{(0)} \sim \mathcal{N}_c(\mathbf{0}, \mathbf{I}_{M+N})$;

Repeat

2: $n = n + 1$;

3: Generate K_p perturbation vectors $\mathbf{p}_i \sim \mathcal{N}_c(\mathbf{0}, \mathbf{I}_{M+N})$, $i = 1, \ldots, K_p$;

4: Form K_p new weight vectors $\tilde{\mathbf{w}}_i \Leftarrow \mathbf{w}^{(n-1)} + \beta \mathbf{p}_i$, $i = 1, \ldots, K_p$;

5: Partition and normalize weight vectors:

$$\tilde{\mathbf{w}}_{1,i} \Leftarrow \frac{\tilde{\mathbf{w}}_i[1:M]}{\|\tilde{\mathbf{w}}_i[1:M]\|}, \quad \tilde{\mathbf{w}}_{2,i} \Leftarrow \frac{\tilde{\mathbf{w}}_i[M+1:M+N]}{\|\tilde{\mathbf{w}}_i[M+1:M+N]\|}, \quad i = 1, \ldots, K_p;$$

6: Measure $P_{RX,i}^{reader} = \eta P_{TX} G_r^2 G_t^2 P_L^2 \left|\tilde{\mathbf{w}}_{1,i}^H \mathbf{h}_1\right|^2 \left|\tilde{\mathbf{w}}_{2,i}^H \mathbf{h}_2\right|^2$, $i = 1, \ldots, K_p$;

7: Update $\mathbf{w}^{(n)} \Leftarrow [\tilde{\mathbf{w}}_{1,I}; \tilde{\mathbf{w}}_{2,I}]$, where $I = \arg \max_i P_{RX,i}^{reader}$;

8: **Until** $\left|P_{RX}^{reader}\left(\mathbf{w}^{(n)}\right) - P_{RX}^{reader}\left(\mathbf{w}^{(n-1)}\right)\right| < \varepsilon$, where ε is the threshold.

2.3.2 Half-duplex Reader

The BABF algorithm for half-duplex systems updates both $\mathbf{w}_1$ and $\mathbf{w}_2$ simultaneously, and it is a variant of Alg. 2.1. Suppose that the half-duplex reader has M transmit antennas and N receive antennas. Then we will use Alg. 2.1 to generate $(M + N)$-dimensional weight vectors, and break them into an M-dimensional transmit beamformer and an N-dimensional receive beamformer. At the nth iteration, K_p new weight vectors are formed. The blind adaptive beamforming algorithm for half-duplex systems is shown in Alg. 2.2.

Note that the BABF algorithm can not only extend the interrogation range, but also improve the ID data transmission reliability, which will be discussed in Chapter 2.4.

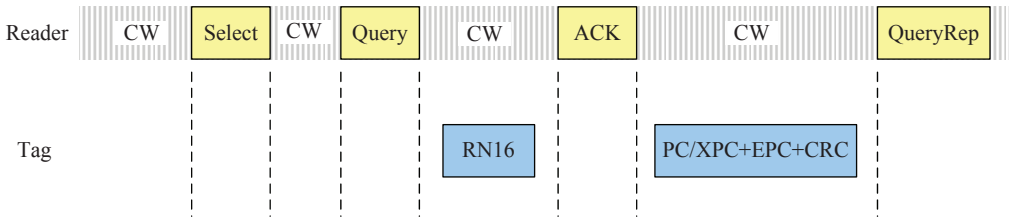

Figure 2.2: Interactions between the reader and the tag.

2.4 Data Backscattering Transmission

After the tag has been powered up by the CW, the reader sends commands (e.g., *Query*) to communicate with the tag. The tag replies to the reader based on the backscattering modulation of the received CW. Fig. 2.2 illustrates the interaction between the reader and the replying tag during the inventory process. The *Select* command is used to select a tag population. An inventory process starts by the reader sending a *Query* command to the tag, which broadcasts a frame consisting of F time slots. After receiving the *Query* command, each tag randomly selects a slot. The tag that picks the *0*th slot replies to the reader with RN16, which is a sequence of 16 bits randomly generated. Then, the reader decodes the received RN16, and sends the decoded 16 bits as the *ACK* to the tag. Next, the tag extracts the 16 bits from the *ACK*. If the extracted 16 bits are the same as the originally generated RN16, the tag then sends its ID, i.e., the electronic product code (EPC) to the reader. After receiving the ID of the current tag, the reader will send the *QueryRep* command to read the next tag. In this section, we assume that the process before the tag replying its EPC is perfectly done, and we focus on the EPC transmission performance of the tag. Note that the EPC is incorporated in a packet during the transmission and besides the EPC, the whole packet, which is 128-bit long, also includes protocol control / extended protocol control (PC/XPC) and cyclic redundancy check (CRC) [38]. In the following, PC/XPC+EPC+CRC is denoted as ID for simplicity. For simplicity, only the full-duplex system is considered in this section.

In the baseband, a tag encodes the backscattered data using the FM0 encoding

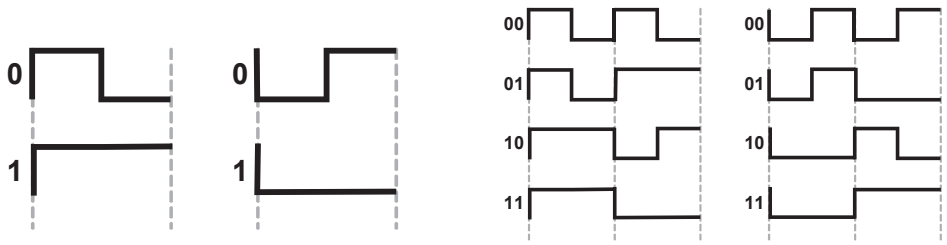

(a) (b)

Figure 2.3: (a) FM0 symbols and (b) FM0 sequences.

scheme illustrated in Fig. 2.3. For FM0 encoding, there is always one phase inverse at every symbol boundary, and an extra phase inverse appears in the middle of symbol 0. Thus, the FM0 sequence is decoded by judging whether there is a phase inverse in the middle of each symbol.

2.4.1 Single-Antenna Case

Let $r^{(ID)}(t)$ denote the received complex baseband FM0 encoded ID signal by the reader after passing through the direct-conversion receiver filter:

$$r^{(ID)}(t) = hs^{(ID)}(t) + n^r(t), \tag{2.22}$$

where $s^{(ID)}(t)$ is the complex baseband FM0 encoded ID signal replied from the tag and $n^r(t)$ is the complex Gaussian noise of the reverse link. Since the tag replies the signal to the reader by modulating the received CW sent by the reader, in the baseband, $s^{(ID)}(t)$ could be expressed as

$$s^{(ID)}(t) = \sqrt{\eta} f^{(ID)}(t) \left(h + n^f(t)\right), \tag{2.23}$$

where $f^{(ID)}(t)$ is the FM0 encoded ID and $n^f(t)$ is the complex Gaussian noise of the forward link.

Suppose the timing synchronization is perfect and the sampling rate is $\frac{2}{T}$. To decode the kth bit replied by the tag, the reader receiver performs the following

differential demodulation operation:

$$y^{(ID)}(k) = \mathrm{Re}\left\{r^{(ID)}(kT + T/4)[r^{(ID)}(kT + 3T/4)]^*\right\}, \tag{2.24}$$

where $\mathrm{Re}\{x\}$ denotes the real part of x, * is the conjugation operator, k is the symbol index, and T is the symbol duration of the backscattered signal.

Then the symbol $a(k)$ is decoded according to the following:

$$\hat{a}(k) = \begin{cases} 1, & \text{if } y^{(ID)}(k) > 0 \\ 0, & \text{if } y^{(ID)}(k) \leq 0 \end{cases}. \tag{2.25}$$

2.4.2 Multiple-antenna Case

For the multiple-antenna case, (2.23) can be rewritten as

$$s^{(ID)}(t) = \sqrt{\eta} f^{(ID)}(t)\left(\mathbf{w}^H \mathbf{h} + n^f(t)\right). \tag{2.26}$$

Thus, the received complex baseband signal at the ith antenna of the reader after passing through the filter is represented as

$$r_i^{(ID)}(t) = h_i s^{(ID)}(t) + n_i^r(t), \tag{2.27}$$

where $n_i^r(t)$ is the complex Gaussian noise at the ith antenna of the reverse link. Similar to (2.24), for the multiple-antenna case, the receiver computes

$$\begin{aligned} y^{(ID)}(k) &= \mathrm{Re}\left\{\sum_{i=1}^{M}\left[w_i r_i^{(ID)}\left(kT+\frac{T}{4}\right)\right]\left[w_i r_i^{(ID)}\left(kT+\frac{3T}{4}\right)\right]^*\right\} \\ &= \mathrm{Re}\left\{\sum_{i=1}^{M}|w_i|^2\, r_i^{(ID)}\left(kT+\frac{T}{4}\right)\left[r_i^{(ID)}\left(kT+\frac{3T}{4}\right)\right]^*\right\}, \end{aligned} \tag{2.28}$$

where w_i denotes the receive beamforming weight. Finally, the symbol $a(k)$ is decoded according to (2.25).

We now consider the choice of the antenna weight w_i. Although the OBF would be the best choice, it requires channel estimation which is hard to implement under the current RFID standard. Therefore, the BABF algorithm can also improve the data

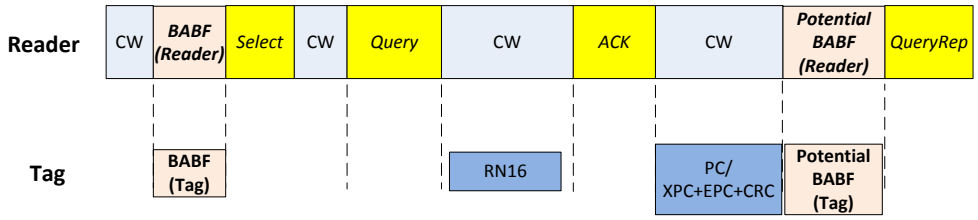

Figure 2.4: A MIMO RFID protocol with BABF algorithm.

transmission effectively as an approximation to the OBF weights. The beamformer vector $\mathbf{w}$ should be chosen to maximize the received SNR at the reader receiver, or equivalently, to maximize the received backscattered power (2.15) from the tag.

To this end, we need to point out that the BABF algorithm is a reader-tag interaction process that needs to be appended to the current RFID standard [38]. Specifically, the BABF algorithm should be executed before the *Select* command for tag activation and initial reading. In case that the channel state information changes during the communication with a tag, another round of weight updates can also be carried out before sending the *QueryRep* commands. A MIMO RFID protocol framework with the BABF algorithm that is compatible with the current RFID standard is shown in Fig. 2.4.

2.5 Tag Quantity Estimation

Upon interrogating the tags, the reader starts by broadcasting an initial frame consisting F time slots. Then each tag selects a slot at random from [0, F-1]. If more than one tag select the same slot, these tags will collide, so no tag could be read successfully. Since the number of tags to be identified is unknown to the reader in the initial interrogation round, if the issued frame size (i.e., the total number of slots) is much larger than the tag quantity, more slots of the frame will be empty which wastes the limited channel resource and decreases the system throughput; if the frame size

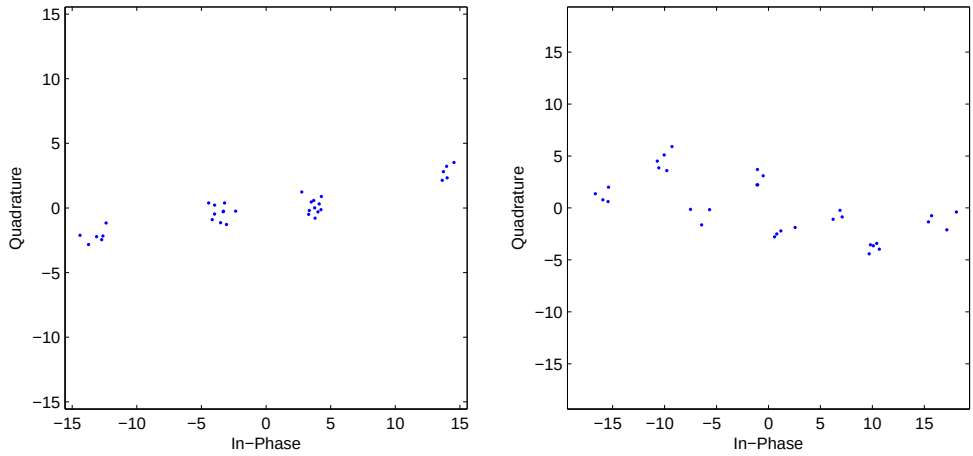

(a) (b)

Figure 2.5: RCS plots based on the reception of the replied RN16s of tags: (a) two tags replying simultaneously resulting in four clusters and (b) three tags replying simultaneously resulting in eight clusters.

is much smaller than the tag quantity, more collisions will occur which also decreases the system throughput. It is known that the system achieves the optimal throughput when the assigned frame size equals to the number of tags in the interrogation range.

A number of works have addressed the estimation of the tag quantity. A collision ratio estimation (CRE) algorithm is proposed in [34] by searching the number of tags to make the actual collision ratio equal to the expected one. Three Bayesian methods are proposed in [35] to estimate the tag quantity with reduced complexity. In [22] the number of tags in a collision slot is estimated according to the tag's radar cross-section (RCS) plot.

After the initial interrogation round, the reader may experience three kinds of time slots: empty slot where there is no tag replying, single-tag slot where there is only one tag replying, and collision slot where there are more than one tag replying simultaneously. Since those unsuccessfully read tags due to the erroneous transmission in the single-tag slot or due to the collision in the collision slot will participate in

the next interrogation round, if the number of those unsuccessfully-read tags in the current frame could be estimated, the frame size of the next interrogation round could be determined according to the estimation result so as to maximize the system throughput. Suppose that the current frame contains N unsuccessfully-read slots due to the erroneous transmission or the collision. At each slot, the reader estimates the number of tags replying, say n_i for the ith slot. Then the total number of the tags participating in the next interrogation round could be estimated as $n_1 + \ldots + n_N$, and the frame size of the next interrogation round could be set accordingly. For simplicity we consider only full-duplex systems.

In the following, we assume that the reader knows there is one tag in each unsuccessfully-read single-tag slot and we focus on the estimation of the number of tags in each collision slot based on the collided signal.

Instead of the tag ID, it is a sequence of FM0 encoded random 16 bits (RN16) that is firstly replied to the reader by the tag upon receiving the *Query* command. The reader should be able to successfully receive and decode this sequence to enable the subsequent communication. But if collision happens, which means multiple RN16s from different tags are sent to the reader simultaneously, the reader is unable to decode the received overlapped RN16s. Thus the collided tags cannot be read successfully and will reply in the next available interrogation round.

It is noticed that one tag's response RN16 signal contributes two clusters in the RCS plot [22], and R simultaneously replying tags produce 2^R clusters in the plot ideally, as illustrated in Fig. 2.5, where the sampling rate is two samples per bit. Consequently, if the reader is able to estimate the number of clusters, the number of the collided tags can be easily derived. Based on this idea, we next develop a tag quantity estimator.

2.5.1 Single-antenna Case

In this subsection, we propose a clustering algorithm to estimate the number of tags involved in the collision slots. We focus on the single receive antenna case first. The clustering algorithm is described as follows.

We consider a specific collision slot. Let $r^{(RN16)}(t)$ denote the received overlapped complex baseband RN16 signal in this slot after passing through the filter, which can be expressed as

$$r^{(RN16)}(t) = \sum_{n=1}^{N_{tag}} h_n s_n^{(RN16)}(t) + n^r(t), \tag{2.29}$$

where $N_{tag} \geq 2$ is the number of tags replying in the slot, h_n is the channel coefficient from the nth tag to the reader and $s_n^{(RN16)}(t)$ is the replied RN16 signal from the nth tag, which is given as

$$s_n^{(RN16)}(t) = \sqrt{\eta} f_n^{(RN16)}(t) \left(h_n + n^f(t)\right), \tag{2.30}$$

where $f_n^{(RN16)}(t)$ is the FM0 encoded RN16 generated by the nth tag.

Suppose the timing synchronization is perfect and the sampling rate is $\frac{2}{T}$ at the reader receiver. Then the received signal sample set in this collision slot is

$$\mathcal{S} = \left\{ r^{(RN16)}\left(\frac{2k+1}{4}T\right), k = 0, ..., 31 \right\}. \tag{2.31}$$

After obtaining $\mathcal{S}$, the reader starts clustering the samples by first selecting one element in $\mathcal{S}$ at random. Then the distances between the selected element and all other elements are calculated. Those elements with distances from the selected element being no larger than r form a cluster together with the selected element, where $r = \rho\sigma$ and ρ is a parameter. Next, the reader repeats the above clustering steps for the elements which have not been clustered until all elements in $\mathcal{S}$ are clustered. Finally, the number of tags in this slot can be derived by counting the number of clusters N_c in $\mathcal{S}$. The proposed tag quantity estimator is summerized in Alg. 2.3.

Algorithm 2.3 - Tag quantity estimation algorithm

1: **For** $j = 1, ..., M_{cs}$, where M_{cs} is the number of collision slots in the current frame;
2: $N_c = 0$;
3: Obtain $\mathcal{S}$ according to (2.31) in the jth slot;
4: **While** $\mathcal{S}$ is not empty, **DO**:
5: Randomly pick one element $s_k \in \mathcal{S}$;
6: Calculate $d_h = |s_k - s_h|$, where $h = 1, ..., |\mathcal{S}|$;
7: Choose elements $\{s_g : d_g \leq \rho\sigma\}$ to form a cluster and remove them from $\mathcal{S}$;
8: $N_c = N_c + 1$;
End While
9: Estimate the number of tags in the jth collision slot as $\lceil \log_2 N_c \rceil$;
End For

2.5.2 Multiple-antenna Case

Although the reader could observe 2^R clusters with R tags involved in a collision slot ideally, it is possible that the actual number of observed clusters is less than 2^R. The reason is that the clusters may overlap with each other due to the impact of channel and noise. For example, the reader may observe only four clusters due to the overlapping effect, albeit there are three tags replying simultaneously and $2^3 = 8$ clusters are supposed to be observed ideally.

Multiple receive antennas may help overcome the overlapping effect. Supposing that multiple antennas are spatially well separated, while one antenna observes overlapped and indistinguishable clusters, other antennas may observe well-separated clusters.

For the multiple-antenna case, (2.30) can be rewritten as

$$s_n^{(RN16)}(t) = \sqrt{\eta} f_n^{(RN16)}(t) \left(\mathbf{w}^H \mathbf{h}_n + n^f(t) \right), \tag{2.32}$$

where $\mathbf{h}_n = [h_{1n}, ..., h_{Mn}]^T$ is the channel vector with h_{in} being the channel coefficient

from the ith reader antenna to the nth tag. And (2.29) now becomes

$$r_i^{(RN16)}(t) = \sum_{n=1}^{N_{tag}} h_{in} s_n^{(RN16)}(t) + n_i^r(t), \tag{2.33}$$

which is the received overlapped complex baseband RN16 signal in a collision slot from the ith receive antenna after passing through the filter. Stacking the received RN16 signals (2.33) of each antenna, we have the vector

$$\mathbf{r}^{(RN16)}(t) = \mathbf{H}\mathbf{s}^{(RN16)}(t) + \mathbf{n}^r(t), \tag{2.34}$$

where $\mathbf{r}^{(RN16)}(t) = [r_1^{(RN16)}(t), ..., r_M^{(RN16)}(t)]^T$, $\mathbf{s}^{(RN16)}(t) = [s_1^{(RN16)}(t), ..., s_{N_{tag}}^{(RN16)}(t)]^T$, $\mathbf{n}^r(t) = [n_1^r(t), ..., n_M^r(t)]^T$, and

$$\mathbf{H} = \begin{bmatrix} h_{11} & \cdots & h_{1N_{tag}} \\ \vdots & \ddots & \vdots \\ h_{M1} & \cdots & h_{MN_{tag}} \end{bmatrix}. \tag{2.35}$$

Then, the signal sample set in (2.31) becomes

$$\mathcal{S} = \left\{ \mathbf{r}^{(RN16)} \left(\frac{2k+1}{4} T \right), k = 0, ..., 31 \right\}. \tag{2.36}$$

The clustering algorithm is similar to Alg. 2.3, except that it is now applied to the vector samples in (2.36) and the corresponding distances between vectors are used.

2.6 Simulation Results

In this section, simulation results are presented. The system parameters are set as follows. Carrier frequency $f_c = 915$ MHz, the total transmit power $P_{TX} = 1W$ (30 dBm), reader antenna gain $G_r = 2$ dBi, tag antenna gain $G_t = 0$ dBi, reader sensitivity $P_{RS} = 3.16 \times 10^{-8}$ mW (-75 dBm), modulation efficiency $\eta = 0.25$, weight adaptation step size $\beta = 0.05$, the number of tags in the reader interrogation range is uniformly distributed in [50, 500] and the initial frame size $F_{init} = 256$. Finally, the Rician channel with the Rician factor $K = 2.8$ dB is adopted as [39].

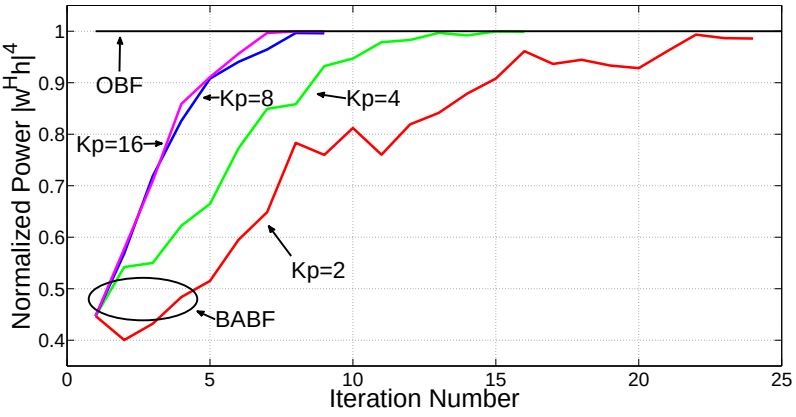

Figure 2.6: The convergence of the proposed BABF algorithm with different values of K_p in full-duplex setting, $M = 2$.

2.6.1 Interrogation Range Performance

We first illustrate the convergence of the proposed BABF algorithm. Fig. 2.6 shows the received power metric $\left|\mathbf{w}^H\mathbf{h}\right|^4$ as in (2.15) versus the iteration number in one simulation for a full-duplex system with the number of antennas $M = 2$. The performance of OBF with ideal CSI is also plotted as a benchmark. It can be observed that the performance of the proposed BABF approaches that of OBF, and the convergence rate increases with the number of perturbations K_p. A similar plot for the half-duplex system with $M = N = 2$ is given in Fig. 2.7. In this setting, the number of antenna weights that need to be optimized doubles, so a larger K_p and more iterations are needed to achieve the benchmark OBF performance.

The tag sensitivity varies from tag to tag. In the following simulations, we fix the reader sensitivity and vary the tags with different sensitivities. Assume there is only one tag in in each round of interrogation range simulation.

2.6.1.1 Interrogation Range for Full-duplex Systems

For full-duplex systems, we choose the tag sensitivity $P_{TS} = 0.04$ mW (-14 dBm) so that $P_{TS} > \sqrt{\eta^{-1} P_{TX} P_{RS}}$ and the system is FLL. Fig. 2.8(a) shows the average

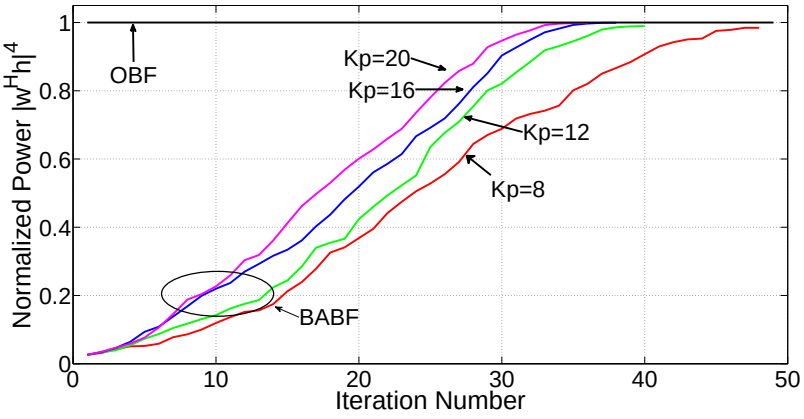

Figure 2.7: The convergence of the proposed BABF algorithm with different values of K_p in half-duplex setting, $M = N = 2$.

interrogation range versus the number of antennas under this setup. Although only BABF, EBF and RBF can be employed in practice as they do not require the channel state information, as a performance upper bound, we also present OBF performance assuming the reader has the channel state information at the startup of the system. It can be observed that OBF is able to read at the longest distances. While the interrogation range generally increases with the number of antennas, the reader with BABF has the closest performance to that of OBF among others. Specifically, the interrogation range is increased from 4.76 m ($M = 1$) to 6.84 m ($M = 2$), then to 10.05 m ($M = 4$) and to 14.11 m ($M = 8$) for BABF; and for EBF, the interrogation range is increased from 4.76 m ($M = 1$) to 5.83 m ($M = 2$), then to 7.76 m ($M = 4$) and to 10.73 m ($M = 8$). Interestingly, unlike other beamforming schemes, for RBF the average interrogation range decreases slightly as the number of antennas increases.

Next, we choose the tag sensitivity $P_{TS} = 0.01$ mW (-20 dBm) so that $P_{TS} < \sqrt{\eta^{-1} P_{TX} P_{RS}}$ and the system is RLL. Fig. 2.8(b) shows the average interrogation range versus the number of antennas under this setup. We observe similar range improvements as in FLL systems. Moreover, under the same antenna configuration,

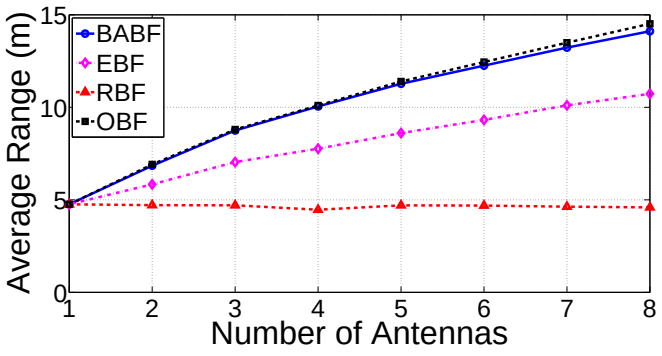

(a) FLL system

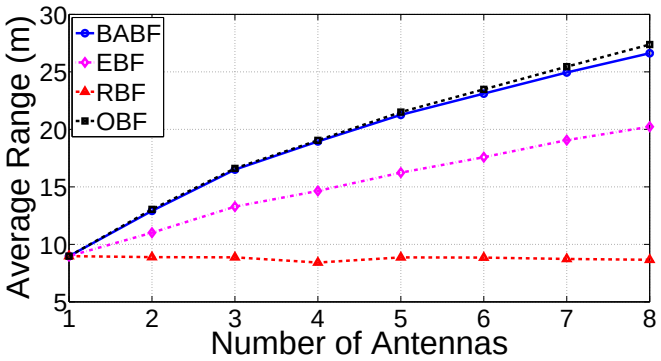

(b) RLL system

Figure 2.8: Average interrogation range versus number of antennas under full-duplex setting.

the interrogation range of the RLL system is larger than that of the FLL system. This is due to the improvement of the tag sensitivity in RLL systems, which enables the tags to detect weaker signals.

2.6.1.2 Interrogation Range for Half-duplex Systems

In the half-duplex setting, the channel state information at the transmitter and receiver is not balanced, and the power transfer efficiency is not equivalent for the forward link and reverse link. Therefore, using tags with 0.01 mW tag sensitivity does not simply imply that the system is absolute RLL anymore. In this case, though for most of the time the system is still RLL, there is a small portion of instances that it is FLL. It is the same case for tags with 0.04 mW sensitivity. Hence, we continue using 0.04 mW and 0.01 mW tag sensitivities in the simulation, but the results are not classified as FLL and RLL here.

We observe similar pattern in the average interrogation range plot shown in Fig. 2.9 for symmetric half-duplex systems, which means the numbers of transmit and receive antennas are the same. For the OBF scheme, the average ranges of half-duplex readers are close to those of full-duplex readers. The average ranges for the BABF scheme are not as long as those in full-duplex configuration, but they are still much better than EBF. Finally, RBF does not show interrogation range improvement as the number of antennas grows for the half-duplex setting as well.

Table 2.1 presents the numerical results for half-duplex readers with asymmetric settings. In all antenna settings, BABF has the best performance in interrogation range as expected. One feature that can be drawn from this table is that when the total number of antennas are fixed, readers with more antennas on the transmitter outperform readers with more antennas on the receiver. For instance the 2×1 and 3×2 settings in Table 2.1, all the beamforming schemes have longer reading distances than those in the 1×2 and 2×3 settings.

In mobile environment where Doppler drift is considered, the proposed MIMO

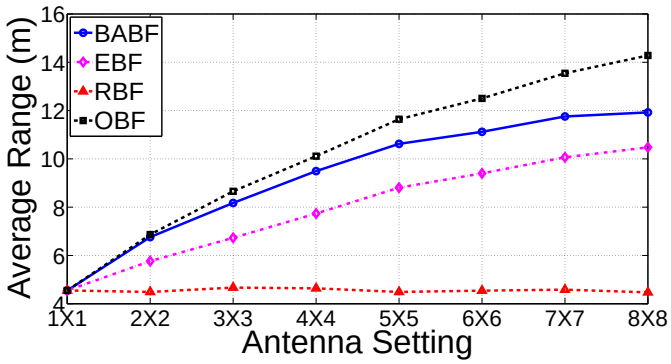

(a) $P_{TS} = 0.04$ mW

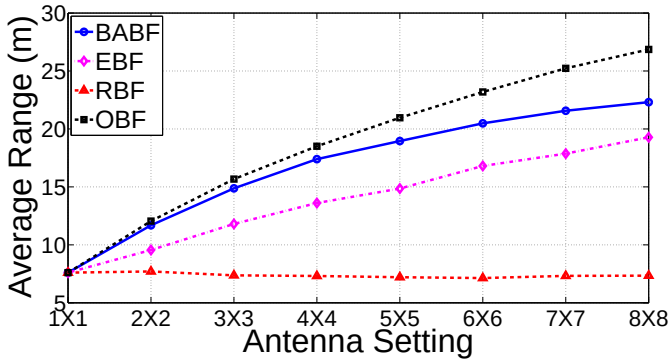

(b) $P_{TS} = 0.01$ mW

Figure 2.9: Average interrogation range versus number of antennas under half-duplex setting.

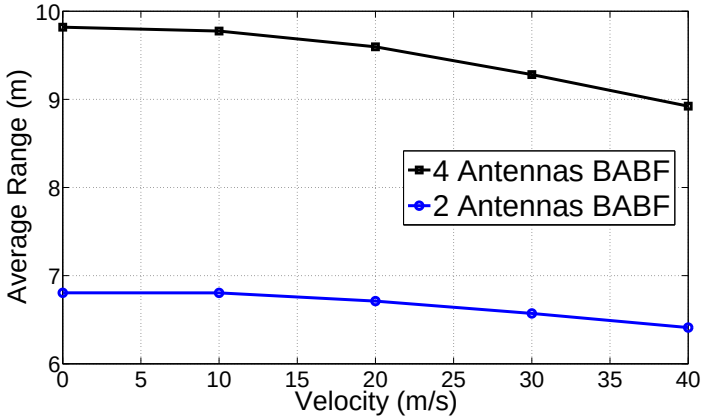

Figure 2.10: Interrogation range in mobile environment.

Table 2.1: Average interrogation range for different numbers of antennas and BF schemes in half-duplex systems.

Antenna setting	BF scheme	Tag sensitivity	
		0.04 mW	0.01 mW
1×2	OBF	4.6541	8.9858
	BABF	4.6528	8.9487
	EBF	3.7925	7.6469
	RBF	4.5888	7.6469
2×1	OBF	6.8128	9.9277
	BABF	6.7124	9.7842
	EBF	6.5830	8.8297
	RBF	4.6682	7.5358
2×3	OBF	7.1437	12.9182
	BABF	6.9281	12.5044
	EBF	5.3290	9.3442
	RBF	4.6033	7.4134
3×2	OBF	8.6924	14.1891
	BABF	8.3997	13.6904
	EBF	7.4709	11.3799
	RBF	4.4826	7.6450

RFID reader system with BABF shows stable result as well. Fig. 2.10 presents the average interrogation range as a function of the velocity of the reader for a 2-antenna and a 4-antenna system. $P_{TS} = 0.04$ mW is considered for both systems. It is observed that the range declines when the velocity increases, but the interrogation range can always be maintained and more than 90% of the reading range in the stationary environment can be achieved. The range reduction of the 4-antenna reader is greater than that of the 2-antenna system, which can be explained by the fact that every antenna link is slow varying, and therefore the total channel variation is stronger for the 4-antenna system. In practice, considering a scenario that the RFID reader is carried by a technician and makes readings with walking speed, the interrogation range is almost constant according to Fig. 2.10.

2.6.2 Data Transmission Performance

Once a tag successfully receives the *ACK* command sent by the reader, it will reply to the reader using a 128-bit packet that includes PC/XPC, EPC, and CRC. If the packet is not received successfully by the reader, the tag will then enter the arbitration state to wait for replying to the reader in the next interrogation round. In this subsection, instead of the bit error rate (BER) performance (e.g., [12] [13]), the more appropriate packet error rate (PER) performance of the system is evaluated and the performance gain of employing multiple antennas is examined.

Fig. 2.11 shows the PER performance versus the transmit signal-to-noise ratio (SNR) for data transmission. For BABF, we set $K_p = 8$ and the number of iterations is 30. It can be observed that the PER performance is significantly improved as the number of antennas M increases. With $M = 2$, BABF has better PER performance than RBF and EBF. The performance offered by BABF is very close to the optimum, i.e., OBF with perfect CSI. One can also observe that the proposed BABF scheme offers about 21 dB gain over the single-antenna case at the PER of 10^{-2} with $M = 2$.

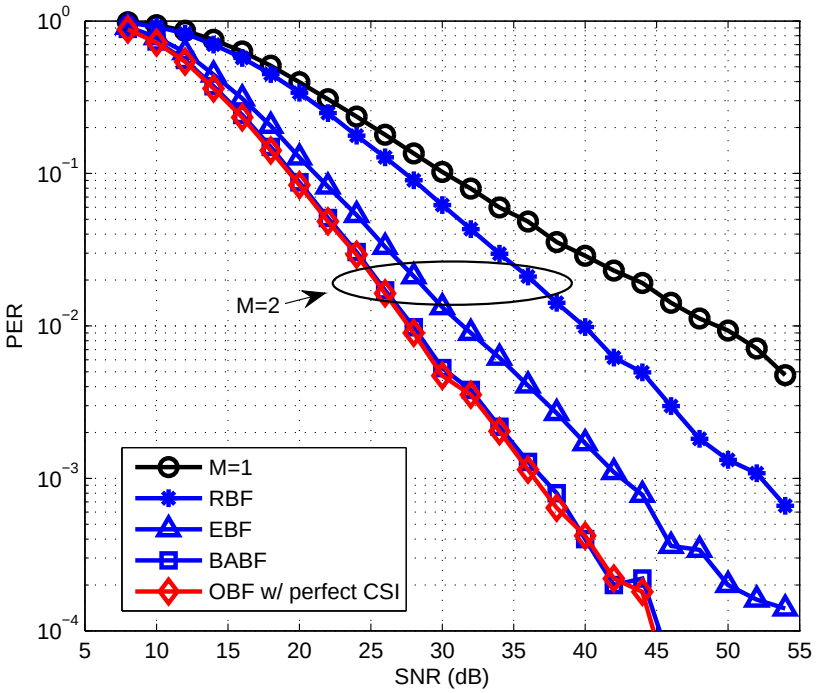

Figure 2.11: PER performance in a Rician fading channel ($K = 2.8$ dB) for different BF schemes.

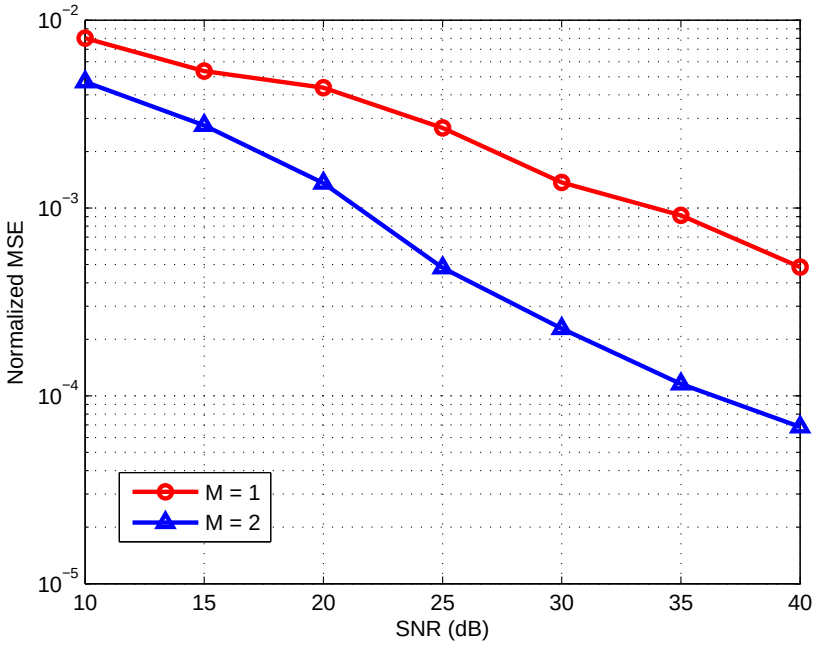

Figure 2.12: Normalized MSE of the estimated number of tags versus SNR.

2.6.3 Tag Quantity Estimation Performance

We suppose that the reader has the knowledge of the noise variance σ^2 and the collided tags have the same distance from the reader. In Alg. 2.3, ρ should be specified in advance. We resort to simulations to find the optimal value of ρ by making 5000 simulation runs to evaluate the performance for each ρ value in the interval of $[1.5, 5.5]$ with step size 0.1.

Fig. 2.12 shows the normalized MSE of the estimation versus SNR. It is seen that the multiple-antenna configuration ($M = 2$) leads to much more accurate estimation than the single-antenna one.

2.7 Experimental Validation

To evaluate the performance of the multiple-antenna RFID system, a number of experiments have been carried out. The goal of these experiments is to show the readability

of the different beamforming schemes at various interrogation ranges, and compare it with that of the single antenna system. Since commercially available RFID readers do not support MIMO or beamforming functionality, a 2×1 half-duplex reader prototype is built using the Universal Software Radio Peripheral (USRP) with SBX daughterboards. The setup has a wide bandwidth that cover 400 to 4400 MHz, and it can provide up to 100 mW of output power. This prototype consists of three S9028PCR circular polarity panel antennas by Larid Technologies : two for transmitting, and one for receiving. The antennad have a gain of 8 dBic. Each antenna is connected to an Ettus Research USRP N210. All the USRPs are connected to a computer, and LabView 2014 is the software used to control and interface. The reader operates at carrier frequency of 915 MHz, IQ rate of 1 MHz, and LabView program gain of 17. The RFID tag tested in this experiment is a UPM Raflatac FROG tag. Note that all the measurements in our experiments should be collected from the tag responses to the EPC commands in the current EPC standard [38], which is the only protocol the commercial tag complies with. In our case, *Query* commands are transmitted, then the RN16 responses are recorded as measurements.

The experiments are set up in a lab environment shown in Fig. 2.13. In order to compare the different beamforming schemes together with the single antenna reader, the tag is read at a series of distances, and its responses are recorded at each position. Specifically, eight evenly spaced points are selected along the center line illustrated in Fig. 2.14. The tag is placed and pointed horizontally to the antennas with a line of sight path in between.

In real RFID readings it takes at least a timeout interval [38] to judge if the tag has been activated. Hence it is not practical to find the exact maximum interrogation range within limited time like in Fig. 2.9. The power received by the tag is also largely affected by the channel state which varies from rounds to rounds. Therefore, in this experiment a large number of readings are tested at each marked location in Fig. 2.14. For each setting, the number of the RN16 tag responses and the total number

Figure 2.13: Experiment setup.

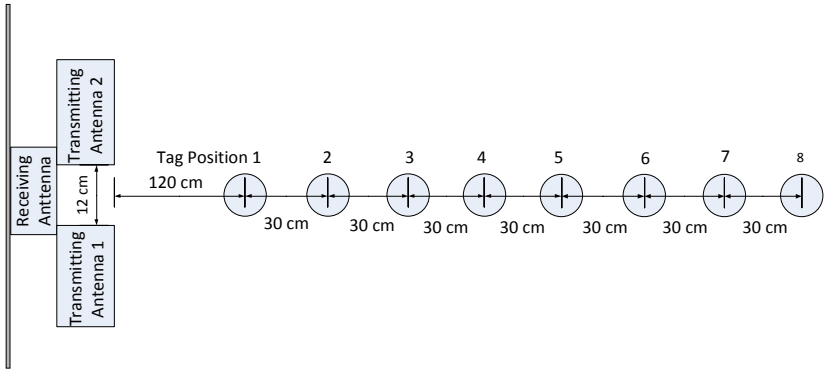

Figure 2.14: Experiment layout.

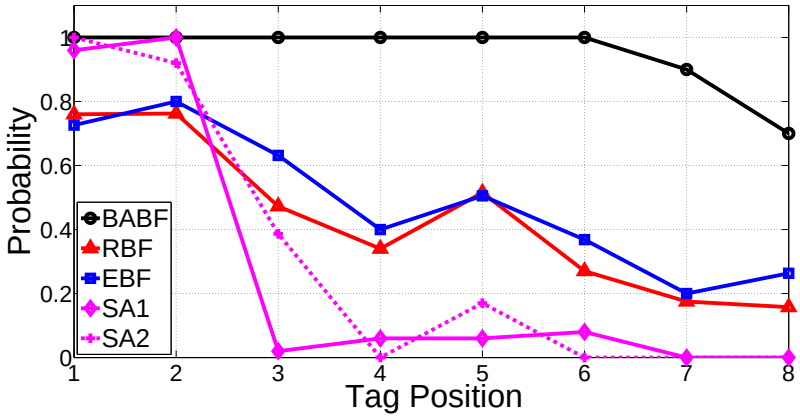

Figure 2.15: Probability of successful RFID tag reading.

of reader *Query* attempts are counted. Thus instead of the average interrogation range in Chapter 2.6, the percentages of successful *Query*-RN16 interaction calculated from the collected data are compared among all the beamforming settings. The tag's backscattered signal strength is also measured in the experiments. It is clear that higher percentage of successful reading indicates better beamforming scheme is at a given position, and so does the stronger signal strength. Therefore, in the experiment we use both the percentage and the signal strength as measures of reader performance.

Fig. 2.15 shows the probabilities of successful RFID tag reading with the different beamforming schemes at selected positions. Obviously, BABF has the largest and most consistent chance to read a tag at all positions. It guarantees successful tag reading at the first 6 points (270 cm), and maintains high probability (0.9 and 0.7) to read the tag at longer distances. Readers with EBF and RBF have similar probability performance; the EBF curve is slightly higher than that of RBF. For these two beamforming settings, neither of these tag positions has zero readings or guarantee perfect readings. Contrast to EBF and RBF, the single-antenna settings (transmitting with either antenna 1 or antenna 2) almost ensure reading when the tag is relatively close to the antenna. However, single antenna readers almost miss all the readings at distances farther than the 3rd point (180 cm). This result illustrates that RFID reader

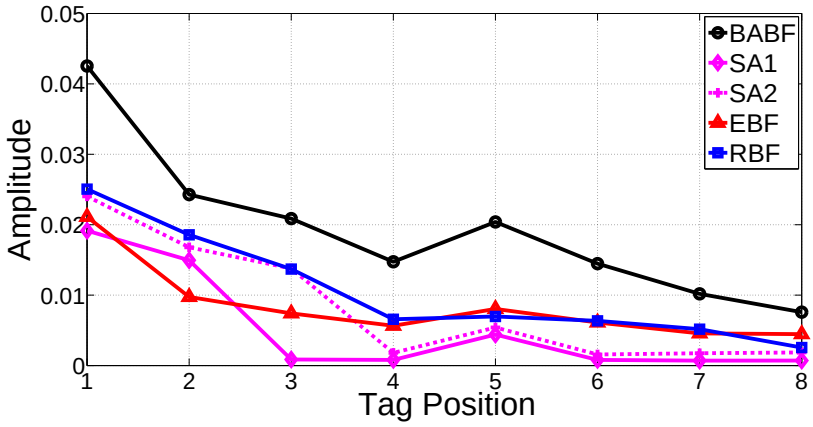

Figure 2.16: Backscattered signal strength received

with single antenna is less sensitive to the channel state, but long distance readings require MIMO settings. For all these antenna settings the probability of successful reading decreases as the tag moves away from the antennas. This trend matches with the simulation results as well. It is interesting that the probabilities for the readers at the 5th point (240 cm) using EBF, RBF and single-antenna 2 are slightly higher than those at the 4th point, which act against the overall trend. This may be caused by environmental factors, e.g., the electromagnetic wave reflection in the laboratory amplifies the signal reception at the 5th point. Nevertheless, the results clearly show that the multiple-antenna RFID reader is more reliable at long distances, and in particular the proposed blind adaptive beamforming algorithm leads the tag reading rate at all distances.

Fig. 2.16 is the plot of backscattered signal amplitude received by the reader. Similar to the probability plot, the reader receives the strongest signal response from the tag when it employs BABF. Readers using EBF and RBF generally can obtain stronger signal at long distances, but have close readings to single antenna reader in short range.

From both the probability and signal strength plots, it is seen that the MIMO RFID reader exhibits a clear advantage in long range interrogation compared with the

standard single-antenna readers. Moreover, the BABF algorithm is validated as an effective and stable technique to find the near-optimal antenna weights, and enhance the reader performance at all distances. Note that the difference of interogation range values in the experiment and the simulation is mainly caused by the difference of transmit power in each case. However, RFID systems with multiple antennas always outperform the single antenna systems in both cases.

2.8 Conclusions

We have proposed a passive multiple-antenna UHF RFID system with the reader equipped with multiple antennas and each tag equipped with a single antenna. The reader interrogation range, data transmission performance and the estimation of tag quantity have been investigated. In particular, the proposed BABF algorithm is performed to optimize the beamforming weights of the reader. As shown in Fig. 2.4, the improvement of the interrogation range is achieved during the transmission of CW before the *Select* command is sent for the FLL system and during the backscattering transmission of the tag for the RLL system.

Our results indicate that under the multiple-antenna configuration, especially with the BABF scheme, the interrogation range extends substantially. The PER performance of the data transmission approaches the optimal beamforming performance with BABF algorithm as well without channel estimation. Finally, we note that the proposed MIMO RFID reader with blind adaptive beamforming complies with the current RFID standard and hence they can be readily implemented in existing systems.

Chapter 3

Wireless Power Transfer by Beamspace MIMO with Lens Antenna Array

3.1 Introduction

In this chapter we design a wireless power transfer (WPT) system using beamspace MIMO, a recently proposed MIMO architecture with lens antenna array. One major challenge is that the efficiency of WPT is low, which leads to high input power consumption and severely limits the coverage range [13]. One key approach to increasing the power transfer efficiency is to employ MIMO and massive MIMO technologies, which has emerged as the key 5G technology to provide higher data rate and spectral efficiency [40]. The appliaction of MIMO to WPT has also been considered. In particular, in [41] the feasibility of a WPT system using multi-antenna array is studied, and it shows that by adding more antennas at the base-station (BS), the range of WPT can be extended. In [42] the authors study the optimal design of channel training for a MIMO WPT system, and propose a method to maximize the harvested energy at the receiver. The superimposed pilot aided channel estimation is considered in [43]

for WPT-enabled massive MIMO system, where the uplink channel estimation and information transmission that powered by WPT can be performed simultaneously. The hybrid analog beamforming is considered in [44] for simultaneous wireless information and power transfer (SWIPT), and [45] shows that the energy beamforming gain, i.e., the end-to-end power transfer efficiency increases linearly with the number of antennas at the transmitter, even with reverse-link based channel training. Wireless power transfer using millimeter wave (mmWave) is studied in [46] for cellular networks, and its performances in energy coverage probability and average harvested power are analyzed in [47]. Wireless power transfer for the phase shifting and selection network is studied in [48] and the effect of rain attenuations is investigated. A compact mmWave wireless power transfer system is prototyped in [49] and it was demonstrated to power smart sensors with relatively high efficiency. The linear energy conversion model is employed in most wireless power transfer works [40, 45, 50]. Some recent works propose non-linear energy transfer models in [51, 52]. Another line of work focuses on the SWIPT [53] where the receivers harvest energy and decode information separately from the signal sent by a common transmitter. Along this line multiple works show that massive MIMO can improve the system performance in different settings [44, 54–57]. However, realizing large-scale MIMO in practice has a key challenge that each antenna element needs to be equipped with a RF chain. Hence, the transmitter requires a large number of RF chains, which leads to high hardware cost and circuit energy consumption.

Recently, the concept of beamspace MIMO has attracted significant attention [58, 59], and the discrete lens array (DLA) is the key component. Essentially, the DLA acts as an analog beamformer, which can transform the spatial channel to the beamspace domain with negligible performance loss. As a result, it enables direct operation in the beamspace which often exhibits strong structural properties, i.e., the beamspace channel is sparse in mmWave band due to the sparse scattering [60]. Since each beam represents one antenna in this system, only a small number of antennas

need to be active to achieve the performance of a conventional mmWave massive MIMO system, and therefore the number of RF chains can be significantly reduced. It has been demonstrated that the DLA-based prototype can achieve a spectral efficiency of 10-20 bits/s/Hz with a 17-31 dB power advantage over the state-of-the-art design at mmWave band [58]. A number of works have addressed various aspect of the DLA-based beamspace MIMO communications. A near-optimal beam selection scheme is proposed to optimize the sum-rate performance for beamspace mmWave massive MIMO systems [61]. The channel estimation problem for beamspace massive MIMO system is investigated in [62]. The work in [63] designs schemes with the lens antenna array at BS to achieve lower signal processing complexity and hardware power cost, while maintaining comparable performance as the conventional MIMO systems. Note that the DLA-based beamspace MIMO is fundamentally the same as the phase shifting and selection hybrid beamforming system in[48]. However, the beamspace MIMO uses completely different hardware components, resulting in significantly lower hardware cost and energy consumption.

In this chapter we study wireless power transfer by the beamspace large-scale MIMO system with lens antenna arrays. We first present the WPT model for the beamspace MIMO which is derived from the spatial MIMO model. By constraining on the number of RF chains in the transmitter, we formulate two WPT optimization problems: the sum power transfer problem and the max-min power transfer problem. The key challenges of the problems are to select the optimal active set of antennas and to compute the corresponding optimal beamformers, which are NP hard. The main contributions of the chapter are summarized as follows.

- We present the system model of wireless power transfer for beamspace MIMO, and formulate two important power transfer problems, the sum power transfer problem and the max-min power transfer problem.

- For the sum power transfer problem we consider two different transmission schemes, the multi-stream and uni-stream transmissions. The multi-stream

scheme forms multiple beamforming vectors which cover all groups of receivers in different locations. In contrast the uni-stream scheme has a single beamforming vector, but the variation in power reception is higher among receivers. We theoretically show that the uni-stream scheme can achieve the same performance as the multi-stream counterpart, and propose two algorithms for the uni-stream power transfer. The first algorithm employs greedy search and eigen-decomposition whereas the second is a truncated power iteration algorithm which is computationally more efficient.

- Similarly for the max-min power transfer problem, both the multi-stream and uni-stream schemes are considered. For the multi-stream scheme, a semidefinite relaxation (SDR)-based greedy algorithm is proposed; and for the uni-stream scheme a Riemannian conjugate gradient algorithm is proposed, which is computationally more efficient and stable compared to the SDR-based greedy algorithm.

3.2 System Model

We consider a mmWave massive MIMO wireless charging system. The power transmitter (PT) is equipped with N antennas, and serves K single-antenna [1] power receivers (PR). We assume that the PT has $M_{RF}(\leq N)$ RF chains due to the practical cost-efficient considerations, and M_{RF} antennas are selected to pair with these RF chains. The system therefore can transmit $M_S(\leq M_{RF})$ streams for power transfer. In the spatial domain, for each stream, a beamforming vector forms a beam which brings in the power gain to those PRs in the beam direction. Multiple streams can simultaneously serve PRs in different locations, but also result in high baseband processing

[1] We consider single-antenna receiver in this work, and the results in this chapter can be generalized to multiple-antenna receivers by alternatively optimizing for the receive beamformers and the transmit beamformer.

complexity. Hence the number of streams M_S is an important system parameter and we will consider the multi-stream (i.e., $M_S > 1$) and uni-stream (i.e., $M_S = 1$) cases separately.

3.2.1 MmWave MIMO Channel Model in Spatial Domain

The first part of this thesis (Chapter 2 and Chapter 3) aims to optimize the performance of the multi-agent sequential test under these two constraints.

First we consider the classic fully digital MIMO architecture with $N = M_{RF}$ as shown in Fig. 3.1(a). Let $\tilde{\boldsymbol{h}}_k \in \mathbb{C}^N$ denote the channel vector of the k-th PR. It is known that the mmWave channel exhibits sparse scattering [60]. We employ the classic Saleh-Valenzula channel model to describe $\tilde{\boldsymbol{h}}_k$ with a line-of-sight (LoS) path and L scattering paths as [58, 60]

$$\tilde{\boldsymbol{h}}_k = \sqrt{\frac{N}{\varrho}}_k \Big(\alpha_{k,0}\boldsymbol{a}(\theta_{k,0}) + \sum_{l=1}^{L} \alpha_{k,l}\boldsymbol{a}(\theta_{k,l})\Big), \tag{3.1}$$

where ϱ_k is the path-loss, $\alpha_{k,0}$ and $\alpha_{k,l}$ are the complex channel gains of the LoS and the l-th scattering path of PR k with the signal physical directions $\theta_{k,0}$ and $\theta_{k,l}$ respectively, and $\boldsymbol{a}(\theta)$ is the steering vector. For uniform linear arrays (ULA) the steering vector can be expressed as $\boldsymbol{a}(\theta) = \frac{1}{\sqrt{N}}[1, e^{j\frac{2\pi}{\lambda}d\sin(\theta)}, \cdots, e^{j(N-1)\frac{2\pi}{\lambda}\sin(\theta)}]^H$, where λ is the wavelength and d is the distance between adjacent antenna elements. Typically $d = \lambda/2$, which yields $\boldsymbol{a}(\theta) = \frac{1}{\sqrt{N}}[1, e^{j\pi\sin(\theta)}, \cdots, e^{j(N-1)\pi\sin(\theta)}]^H$. Denote $\tilde{\boldsymbol{H}} = [\tilde{\boldsymbol{h}}_1, \cdots, \tilde{\boldsymbol{h}}_K] \in \mathbb{C}^{N\times K}$ as the channel matrix of all PRs.

Let $\boldsymbol{v}_m \in \mathbb{C}^N$ be the beamforming vector of the power stream m, and $\hat{\boldsymbol{V}} = [\boldsymbol{v}_1, \cdots, \boldsymbol{v}_{M_S}] \in \mathbb{C}^{N\times M_S}$ be the beamforming matrix. To satisfy the transmit power constraint, we have $\mathrm{Tr}(\tilde{\boldsymbol{V}}^H\tilde{\boldsymbol{V}}) \le P$ where P is the total power supply at the PT. Let $\boldsymbol{s} \in \mathbb{C}^{M_S}$ be the power signal vector with $\mathbb{E}(\boldsymbol{s}\boldsymbol{s}^H) = \boldsymbol{I}_{M_S}$. Hence, the received signal vector for all PRs is

$$\tilde{\boldsymbol{y}} = \tilde{\boldsymbol{H}}^H\hat{\boldsymbol{V}}\boldsymbol{s} \in \mathbb{C}^K. \tag{3.2}$$

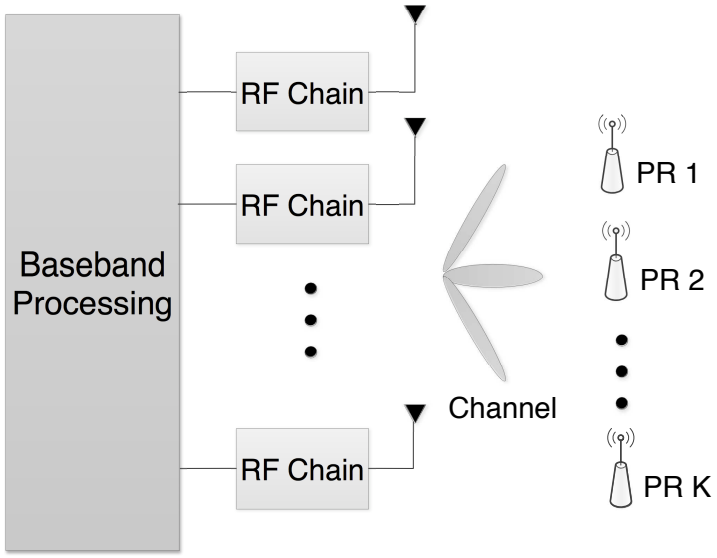

(a) Traditional MIMO system

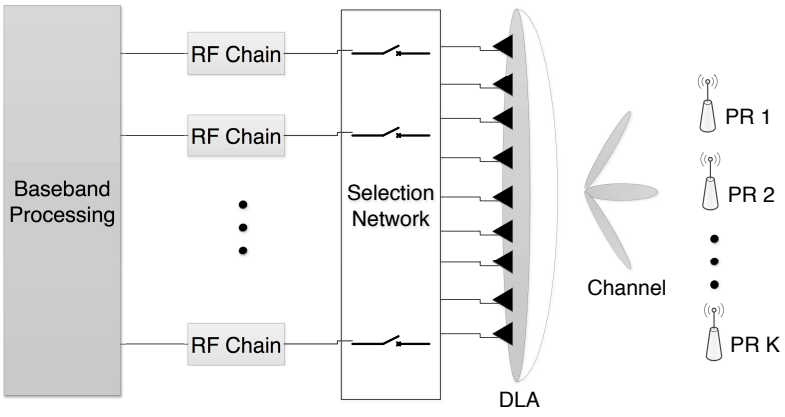

(b) Beamspace MIMO with lens antenna array

Figure 3.1: Illustration of the two types of multi-agent systems.

3.2.2 Beamspace MIMO with Lens Antenna Array

The channel model of beamspace MIMO can be transformed from the conventional MIMO in the spatial domain with carefully designed lens antenna array [58, 62]. As shown in Fig. 3.1(b), N antenna elements are attached to the lens to form a discrete lens array (DLA), and such DLA acts as an $N \times N$ discrete Fourier matrix $\boldsymbol{U}$ which transforms between the spatial domain and beamspace domain. In other words, the DLA turns an omni-directional signal into a beam. Specifically, the DLA matrix is $\boldsymbol{U} = [\tilde{\boldsymbol{a}}(1), \cdots, \tilde{\boldsymbol{a}}(N)]$, where column $\tilde{\boldsymbol{a}}(m) = \frac{1}{\sqrt{N}}[1, e^{jm\pi}, e^{jm2\pi}, \cdots, e^{jm(N-1)\pi}]^H$ represents the orthogonal array steering vector of the m-th antenna elements in the DLA. Hence, for any PR k, the channel vector for the beamspace MIMO becomes $\boldsymbol{h}_k = \boldsymbol{U}^H \tilde{\boldsymbol{h}}_k$. The received signal vector for the beamspace MIMO is

$$\boldsymbol{y} = \boldsymbol{H}^H \hat{\boldsymbol{V}} \boldsymbol{s} = \tilde{\boldsymbol{H}}^H \boldsymbol{U} \hat{\boldsymbol{V}} \boldsymbol{s} \in \mathbb{C}^K, \tag{3.3}$$

where $\boldsymbol{H} = \boldsymbol{U}^H \tilde{\boldsymbol{H}}$ is the beamspace MIMO channel matrix. We assume that the channel matrix $\boldsymbol{H}$ is known to the transmitter [2].

So far we have considered the beamspace MIMO system with full deployment of the N antennas, which requires N individual RF chains. In this chapter, we consider the hybrid beamforming architecture with $M_{RF}(\leq N)$ RF chains using antenna selection. There are two main reasons. The first is for cost efficiency, since reducing the number of RF chains will lower the total cost of the RF circuits given that the RF chain module is expensive. Secondly, the mmWave channel has limited and sparse scattering, especially for the beamspace MIMO since the channel is sparse under the Fourier bases. This means that it is not necessary to use every antenna for power transmission, and it suffices to use the dominant beams. As a result, M_{RF} antennas are selected, which form the effective channel matrix $\boldsymbol{H}(\mathcal{A}) = \boldsymbol{H}[n, :]_{\{n\in\mathcal{A}\}} = \boldsymbol{U}[n, :]^H_{\{n\in\mathcal{A}\}} \tilde{\boldsymbol{H}} \in \mathbb{C}^{M_{RF}\times K}$ where $\mathcal{A}$ is the set of indices of selected antennas, and the corresponding beamforming matrix becomes $\boldsymbol{V} \in \mathbb{C}^{M_{RF}\times M_S}$.

[2] Channel estimation can be efficiently performed for beamspace MIMO[62].

The final signal model is then

$$\boldsymbol{y} = \boldsymbol{H}(\mathcal{A})^H \boldsymbol{V}\boldsymbol{s} \in \mathbb{C}^K. \tag{3.4}$$

The received power vector of all PRs is

$$\boldsymbol{p} = \text{diag}(\boldsymbol{V}^H \boldsymbol{H}(\mathcal{A})\boldsymbol{H}(\mathcal{A})^H \boldsymbol{V}), \tag{3.5}$$

where diag$(\cdot)$ returns a vector consisting of the diagonal elements of the input matrix. Note that in (3.5) we employ the linear RF energy harvesting model[45, 50]. Recent experiments in[64] show that the linear model is justified and can accurately characterize the relationship between the transmitted and received power.

Note that in wireless power transfer systems all PRs can harvest power from a common RF power stream, hence it is not necessary to restrict that $K \leq M_S$. In fact, it is preferable to design a system with M_S as low as possible since this would make the beamformer design and baseband processing tasks much more efficient.

3.3 Maximum Sum Power Transfer

In this section we treat the beamformer design for maximizing the sum power transfer in the beamspace MIMO system.

3.3.1 Problem Formulation

Given the power signal model in (3.4), the sum power delivered to all users is $\text{Tr}(\boldsymbol{V}^H \boldsymbol{H}(\mathcal{A})\boldsymbol{H}(\mathcal{A})^H \boldsymbol{V})$ with selected antenna set $\mathcal{A} \subset \{1, \cdots, N\}$. The objective is to select the best M_{RF} antennas and design the corresponding beamformer matrix $\boldsymbol{V} \in \mathbb{C}^{M_{RF} \times M_S}$ to maximize the total delivered power, i.e.,

$$\begin{aligned} \textbf{P3.1}: \quad \max_{\mathcal{A}, \boldsymbol{V}} \quad & \text{Tr}(\boldsymbol{V}^H \boldsymbol{H}(\mathcal{A})\boldsymbol{H}(\mathcal{A})^H \boldsymbol{V}) \\ \text{s.t.} \quad & |\mathcal{A}| = M_{RF}, \\ & \text{Tr}(\boldsymbol{V}^H \boldsymbol{V}) \leq P. \end{aligned} \tag{3.6}$$

Problem **P3.1** is hard to solve. First, the optimization over the cardinality-constrained discrete set $\mathcal{A}$ is NP-hard. Secondly, the objective is to maximize a quadratic function in $\boldsymbol{V}$ which is non-convex. Next we show that uni-stream transmission is optimal, i.e., $M_S = 1$. We then propose two algorithms for uni-stream sum power maximization.

3.3.2 Optimality of Uni-stream Transmission

Due to the difficulty of **P3.1**, we decompose it into two subproblems: the beamformer optimization subproblem and the antenna selection subproblem. First in the beamformer optimization subproblem, a set of antennas $\mathcal{A}'$ with cardinality $|\mathcal{A}'| \leq M_{RF}$ is given as input. As a result, the dimension of the beamforming matrix $\tilde{\boldsymbol{V}}$ becomes $|\mathcal{A}'| \times M_S$. The beamformer optimization problem can be expressed as

$$\rho(\mathcal{A}') = \max_{\{\tilde{\boldsymbol{V}} \in \mathbb{C}^{|\mathcal{A}'| \times M_S} : \mathrm{Tr}(\tilde{\boldsymbol{V}}^H \tilde{\boldsymbol{V}}) \leq P\}} f_{\mathcal{A}'}(\tilde{\boldsymbol{V}}), \tag{3.7}$$

where $f_{\mathcal{A}'}(\tilde{\boldsymbol{V}}) \triangleq \mathrm{Tr}(\tilde{\boldsymbol{V}}^H \boldsymbol{H}(\mathcal{A}') \boldsymbol{H}(\mathcal{A}')^H \tilde{\boldsymbol{V}})$ is the amount of power delivered using $\tilde{\boldsymbol{V}}$ with antenna set $\mathcal{A}'$. Note that the problem in (3.7) is non-convex. A straight-forward method to solve this problem is to introduce a semi-definite matrix $\boldsymbol{W} = \tilde{\boldsymbol{V}} \tilde{\boldsymbol{V}}^H \in \mathbb{S}_+^{|\mathcal{A}'|}$, where $\mathbb{S}_+^{|\mathcal{A}'|}$ denotes the set of semi-definite matrices with dimension $|\mathcal{A}'| \times |\mathcal{A}'|$. By dropping the rank constraint on $\boldsymbol{W}$ we obtain a semi-definite relaxed problem, which can be solved by any convex solver. An approximate solution to $\tilde{\boldsymbol{V}}$ can then be obtained by eigen-decomposition of $\boldsymbol{W}$. However, the optimal solution to (3.7) can be found analytically, as shown in the following results.

Lemma 1. *For any channel matrix $\boldsymbol{H}(\mathcal{A}')$ with a given antenna set $\mathcal{A}'$, the optimizer of $f_{\mathcal{A}'}(\tilde{\boldsymbol{V}})$ is in the eigenspace corresponding to the largest eigenvalue of $\boldsymbol{H}(\mathcal{A}')\boldsymbol{H}(\mathcal{A}')^H$.*

Proof. See Appendix 3.7.1. □

Theorem 1. *For any channel matrix $\boldsymbol{H}(\mathcal{A}')$ with a given $\mathcal{A}'$, there always exists a rank-1 optimal solution to (3.7). That is, the uni-stream transmission is optimal.*

Proof. See Appendix 3.7.2.

□

Lemma 1 and Theorem 1 show that problem (3.7) can be efficiently solved by performing eigen-decomposition on $\boldsymbol{H}(\mathcal{A}')\boldsymbol{H}(\mathcal{A}')^H$. The optimal objective value in (3.7) is given by $\rho(\mathcal{A}') = \lambda^* P$, where λ^* is the largest eigenvalue of $\boldsymbol{H}(\mathcal{A}')\boldsymbol{H}(\mathcal{A}')^H$. The optimizer is any one of the eigenvectors corresponding to λ^*. Compared to the suboptimal semi-definite relaxation method, this solution is not only optimal but also more efficient as it only performs eigen-decomposition instead of convex optimization.

3.3.3 Sum Power Maximization - Algorithm 1

The antenna selection subproblem is to find the set of antennas that maximizes the total power throughput, i.e.,

$$\max_{|\mathcal{A}|=M_{RF}} \rho(\mathcal{A}). \tag{3.8}$$

This problem is NP-hard. The most straightforward approach is the exhaustive search over all possible $\mathcal{A}$. However, the search space of this problem has size of $\binom{N}{M_{RF}}$, which is computationally prohibitive for systems with large number of antennas, e.g., the search space is over 4.88×10^{18} for $N = 64$ and $M_{RF} = 16$. Hence, we employ a greedy algorithm to solve the antenna selection problem in (3.8). The first sum power maximization algorithm is summarized as the SUM1 algorithm in Alg. 3.1.

The SUM1 algorithm initiates with an empty antenna set. In the first iteration, the algorithm tests the sum power transfer with a single transmit antenna. In step 1, it evaluates the system performance $\rho(n)$ where $n \in \{1, \cdots, N\}$, and selects the one which enables the highest power transfer, and then adds it to the antenna set in step 2. This antenna is the strongest antenna. In the next iteration, the algorithm adds another one to the antenna set such that it can generate the largest power transfer

Algorithm 3.1 (SUM1) - Max sum power transfer algorithm

Input: beamspace channel matrix $\boldsymbol{H}$;

Initialization: $\mathcal{A}_0 = \emptyset$;

For $j = 1, 2, \cdots, M_{RF}$**:**

1: Compute $n_j^* = \underset{n \in \{1,\cdots,N\} \setminus \mathcal{A}_{j-1}}{\operatorname{argmax}} \rho(\mathcal{A}_{j-1} \cup n)$, where function ρ outputs the largest eigenvalue of $(\boldsymbol{H}(\mathcal{A}_{j-1} \cup n)\boldsymbol{H}(\mathcal{A}_{j-1} \cup n)^H)$;

2: Set $\mathcal{A}_j = \mathcal{A}_{j-1} \cup n_j^*$;

End

Output: Antenna set $\mathcal{A}_{M_{RF}}$, beamformer $\boldsymbol{v}^* \in \mathbb{C}^{M_{RF}}$ which is any eigenvector corresponding to the largest eigenvalue of $(\boldsymbol{H}(\mathcal{A}_{M_{RF}})\boldsymbol{H}(\mathcal{A}_{M_{RF}})^H)$.

together with the antenna found in the first iteration. In other words, in each iteration the algorithm looks for the antenna which brings in the largest marginal gain to the existing antenna set. The size of the antenna set grows by 1 after each iteration, and finally it terminates when the set has size M_{RF}.

3.3.4 Sum Power Maximization - Algorithm 2

Note that in the i-th iteration of SUM1 algorithm, $(N - i)$ eigen-decompositions are computed. Here we develop an alternative solution that does not require eigen-decomposition.

In the uni-stream setting, the overall problem **P3.1** in (3.6) can be rewritten as

$$\max_{\boldsymbol{v} \in \mathbb{C}^N} f(\boldsymbol{v}) = \boldsymbol{v}^H \boldsymbol{H} \boldsymbol{H}^H \boldsymbol{v}, \quad \text{s.t. } \|\boldsymbol{v}\|_2^2 = P, \|\boldsymbol{v}\|_0 = M_{RF}, \tag{3.9}$$

where $\|\boldsymbol{v}\|_0$ is the zero norm or cardinality, i.e., the number of non-zeros elements of $\boldsymbol{v}$. Note that the set $\mathcal{A}$ in (3.6) corresponds to the non-zero elements of $\boldsymbol{v}$ in (3.9). This problem is known as the sparse principal component analysis (SPCA) problem in the

Algorithm 3.2 (SUM2) - Max sum power transfer

Input: beamspace channel $\boldsymbol{H}$, RF chain number M_{RF};

Initialization: $\boldsymbol{v} = \boldsymbol{v}^{(0)}$ as the dominant eigenvector of the solution to **P3.2** in (3.12), $t = 1$;

Repeat

1: Compute $\tilde{\boldsymbol{v}}^{(t)} = (\boldsymbol{H}\boldsymbol{H}^H\boldsymbol{v}^{(t-1)})/\|\boldsymbol{H}\boldsymbol{H}^H\boldsymbol{v}^{(t-1)}\|_2$;

2: Truncate $\hat{\boldsymbol{v}}^{(t)} = \text{Trun}(\tilde{\boldsymbol{v}}^{(t)}, M_{RF})$ defined in (3.10);

3: Set $\boldsymbol{v}^{(t)} = \hat{\boldsymbol{v}}^{(t)}/\|\hat{\boldsymbol{v}}^{(t)}\|_2$;

4: $t \leftarrow t + 1$;

Until convergence

Output: final beamformer vector $\boldsymbol{v}^{(t)}$.

optimization literature [65–68]. In [66], a semi-definite programming (SDP)-based method was proposed. The authors further proposed a greedy algorithm in [67] which improves the computational efficiency. Recently, [68] proposed an iterative truncated power method that has recovery performance guarantee. In this chapter, we solve (3.9) by the SUM2 algorithm in Alg. 3.2 based on the truncated power method [68] with a carefully designed initial point.

The SUM2 algorithm is an iterative method. At iteration t, the algorithm first computes the new normalized beamformer $\tilde{\boldsymbol{v}}^{(t)}$ using the beamformers obtained in the previous iteration, according to step 1. In step 2, the new beamformer is truncated to keep only the top M_{RF} elements and set the rest to 0, i.e., $\text{Trun}(\tilde{\boldsymbol{v}}^{(t)}, M_{RF})$ returns an $N \times 1$ vector whose i-th element is given as

$$\text{Trun}(\tilde{\boldsymbol{v}}^{(t)}, M_{RF})[i] = \begin{cases} \tilde{\boldsymbol{v}}^{(t)}[i], & \text{if} \quad |\tilde{\boldsymbol{v}}^{(t)}[i]| \geq \alpha; \\ 0, & \text{otherwise}, \end{cases} \tag{3.10}$$

where α is the absolute value of the M_{RF}-th largest element in $\tilde{\boldsymbol{v}}^{(t)}$. In step 3, the

beamformer of the current iteration is updated as the normalized truncated vector $\hat{\boldsymbol{v}}^{(t)}$ from step 2, and passed to the next iteration. The algorithm terminates when the following stopping criterion is satisfied,

$$\|\boldsymbol{v}^{(t)} - \boldsymbol{v}^{(t-1)}\|_2 \leq \epsilon, \tag{3.11}$$

where ϵ is the error tolerance parameter.

Choosing the initial point $\boldsymbol{v}^{(0)}$ is important for the SUM2 algorithm since it often determines where $\boldsymbol{v}^{(t)}$ converges to. To that end, we solve the following problem to obtain our initial point.

$$\begin{aligned} \mathbf{P3.2}: \quad \max_{\boldsymbol{W}\in\mathbb{S}_+^N} \quad & \mathrm{Tr}(\boldsymbol{H}\boldsymbol{H}^H\boldsymbol{W}) && (3.12)\\ \text{s.t.} \quad & \mathrm{Tr}(\boldsymbol{W}) = P \\ & \mathbf{1}^T|\boldsymbol{W}|\mathbf{1} \leq M_{RF}P, && (3.13) \end{aligned}$$

where $\mathbf{1}$ is the all-1 vector and $|\boldsymbol{W}|$ takes the absolute value of $\boldsymbol{W}$ element-wisely. The optimal value of problem **P3.2** is known as a tight upper bound of the problem in (3.9) [66]. In fact, this is an SDP problem after several steps of relaxation. In particular, the constraint $\|\boldsymbol{v}\|_0 = M_{RF}$ in (3.9) is relaxed to two constraints: $\mathrm{Card}(\boldsymbol{W}) \leq M_{RF}^2$, where $\mathrm{Card}(\boldsymbol{W})$ outputs the number of non-zeros elements in matrix $\boldsymbol{W}$, and $\mathrm{Rank}(\boldsymbol{W}) = 1$. Then, because $\|\boldsymbol{v}\|_0 = M_{RF}$ implies $\|\boldsymbol{v}\|_1 \leq \sqrt{M_{RF}}\|\boldsymbol{v}\|_2$ by Cauchy-Schwartz inequality, and by using the fact that $\|\boldsymbol{W}\|_F = \sqrt{\mathrm{Tr}(\boldsymbol{W}\boldsymbol{W}^H)} = \sqrt{\mathrm{Tr}(\boldsymbol{v}\boldsymbol{v}^H\boldsymbol{v}\boldsymbol{v}^H)} = \sqrt{P\mathrm{Tr}(\boldsymbol{W})} = P$, given that $\boldsymbol{W} = \boldsymbol{v}\boldsymbol{v}^H$, the non-convex constraint $\mathrm{Card}(\boldsymbol{W}) \leq M_{RF}^2$ can be replaced by a weaker but convex constraint in (3.13). Further dropping the rank-1 constraint of $\boldsymbol{W}$ yields the semidefinite programming problem **P3.2**. Since the optimal function value of problem **P3.2** gives a good estimate of the optimal value in (3.9), it is reasonable to assume that the optimizer of (3.9) is in the neighborhood of the rank-1 approximation to the optimal $\boldsymbol{W}$. Hence, the initial point of the SUM2 algorithm is set as the dominant eigenvector of the optimizer of problem **P3.2**. In practice, it is reported that the solution to **P3.2** tends to have a rank very close to 1 [66].

In each iteration the SUM2 algorithm essentially solves the following problem

$$\boldsymbol{v}^{(t)} = \underset{\|\boldsymbol{v}\|_2^2=P, \|\boldsymbol{v}\|_0 \le M_{RF}}{\operatorname{argmax}} \; g(\boldsymbol{v}, \boldsymbol{v}^{(t-1)}), \tag{3.14}$$

where $g(\boldsymbol{v}, \boldsymbol{v}^{(t-1)}) = \boldsymbol{v}^{(t-1)^H} \boldsymbol{H}\boldsymbol{H}^H(\boldsymbol{v}-\boldsymbol{v}^{(t-1)})$. Then using the fact that $g(\boldsymbol{v}^{(t)}, \boldsymbol{v}^{(t-1)}) \ge g(\boldsymbol{v}^{(t-1)}, \boldsymbol{v}^{(t-1)}) = 0$ and $\boldsymbol{H}\boldsymbol{H}^H$ is positive definite,

$$\begin{aligned} f(\boldsymbol{v}^{(t)}) - f(\boldsymbol{v}^{(t-1)}) &= 2g(\boldsymbol{v}^{(t)}, \boldsymbol{v}^{(t-1)}) + (\boldsymbol{v}^{(t)} - \boldsymbol{v}^{(t-1)})^H \times \\ &\qquad \boldsymbol{H}\boldsymbol{H}^H(\boldsymbol{v}^{(t)} - \boldsymbol{v}^{(t-1)}) \\ &\ge 0, \end{aligned}$$

where $f(\boldsymbol{v})$ is the sum power transfered using beamformer $\boldsymbol{v}$ defined in (3.9). Hence, the objective function is non-decreasing over the iterations and the SUM2 algorithm converges to a local maximizer [68].

Compared with the SUM1 algorithm, the SUM2 algorithm has a simpler structure where the search for the antenna set is replaced by the truncation step to enforce the sparsity requirement of $\boldsymbol{v}$ in (3.9), which significantly reduces the computational complexity. In particular, in each iteration of the SUM2 algorithm, the dominant complexity is due to the matrix multiplication in step 1. In contrast, in the i-th iteration of the SUM1 algorithm, it requires to perform $(N-i)$ eigen-decompositions, which has much higher complexity.

It is worth mentioning that the lens antenna array plays an important role in the wireless power transfer system under consideration since it transforms the channel matrix from the spatial domain to the sparse beamspace domain, which allows the transmitter to efficiently concentrate the transmit power on fewer transmit antennas and achieves higher power throughput. In fact, both SUM1 and SUM2 algorithms can be applied to the conventional wireless power transfer system without employing the lens antenna array. However, the system performance is significantly improved for the beamspace MIMO, as will be illustrated via simulations in Chapter 3.5.

3.4 Max-Min Power Transfer

In many other scenarios, we are interested in maximizing the minimum received power among all power receivers, to maintain fairness. In this section we study the transmission schemes for max-min power transfer.

3.4.1 Problem Formulation

We denote $\boldsymbol{h}_k(\mathcal{A}) = \boldsymbol{h}_k[n]_{\{n:n\in\mathcal{A}\}} \in \mathbb{C}^{M_{RF}}$ as the effective beamspace channel vector for PR k. The max-min power transfer problem is formulated as follows

$$\begin{aligned} \mathbf{Q1}: \max_{\mathcal{A},\boldsymbol{V}\in\mathbb{C}^{M_{RF}\times M_S}} \quad & \min_{k\in\{1,\cdots,K\}} && \mathrm{Tr}(\boldsymbol{V}^H\boldsymbol{h}_k(\mathcal{A})\boldsymbol{h}_k(\mathcal{A})^H\boldsymbol{V}) \\ & \text{s.t.} && |\mathcal{A}| = M_{RF}, \\ & && \mathrm{Tr}(\boldsymbol{V}^H\boldsymbol{V}) \le P. \end{aligned} \tag{3.15}$$

Problem **Q1** is non-convex and NP-hard.

Note that for the max-min power transfer problem, when all receivers are homogeneous or use the same energy harvesting components, the solutions under the linear energy conversion model and the non-linear energy conversion model (e.g. in [51]) are the same. To see this, under the non-linear model, the harvested energy of receiver k is $f(\mathrm{Tr}(\boldsymbol{V}^H\boldsymbol{h}_k(\mathcal{A})\boldsymbol{h}_k(\mathcal{A})^H\boldsymbol{V}))$, where f is a monotonically increasing non-linear function. For the max-min power transfer problem, i.e., $\max_{\mathcal{A},\boldsymbol{V}} \min_k f(\mathrm{Tr}(\boldsymbol{V}^H\boldsymbol{h}_k(\mathcal{A})\boldsymbol{h}_k(\mathcal{A})^H\boldsymbol{V}))$, the performance is bounded by the worst receiver. Since f is monotonically increasing, the worst receiver is the one with the lowest value of $\mathrm{Tr}(\boldsymbol{V}^H\boldsymbol{h}_k(\mathcal{A})\boldsymbol{h}_k(\mathcal{A})^H\boldsymbol{V})$. Therefore the problem is equivalent to $\max_{\mathcal{A},\boldsymbol{V}} \min_k \mathrm{Tr}(\boldsymbol{V}^H\boldsymbol{h}_k(\mathcal{A})\boldsymbol{h}_k(\mathcal{A})^H\boldsymbol{V})$, which is the max-min power transfer problem **Q1** under the linear model.

3.4.2 Multi-Stream Max-Min Power Transfer

As in the SUM1 algorithm, problem **Q1** is decomposed into two subproblems: the beamformer design subproblem and the antenna selection subproblem. For a given

set of selected antennas $\mathcal{A}'$, the beamformer design subproblem is

$$\gamma(\mathcal{A}') = \max_{\{\tilde{\boldsymbol{V}} \in \mathbb{C}^{|\mathcal{A}'| \times M_S} : \mathrm{Tr}(\tilde{\boldsymbol{V}}^H \tilde{\boldsymbol{V}}) \leq P\}} g_{\mathcal{A}'}(\tilde{\boldsymbol{V}}), \tag{3.16}$$

where $g_{\mathcal{A}'}(\tilde{\boldsymbol{V}}) \triangleq \min_k \mathrm{Tr}(\tilde{\boldsymbol{V}}^H \boldsymbol{h}_k(\mathcal{A}') \boldsymbol{h}_k(\mathcal{A}')^H \tilde{\boldsymbol{V}})$ is the lowest received power by all PRs. Different from the sum power transfer problem in (3.7), (3.16) has no closed-form solution. Since $g_{\mathcal{A}'}$ is a point-wise minimum of a convex quadratic function, it is not convex nor concave. Hence, we relax the problem by introducing the semi-definite matrix variable $\boldsymbol{W} = \tilde{\boldsymbol{V}} \tilde{\boldsymbol{V}}^H$. By dropping the rank constraint of $\boldsymbol{W}$, problem $\gamma(\mathcal{A}')$ is relaxed to

$$\begin{aligned} \max_{\boldsymbol{W}} \min_k \quad & \mathrm{Tr}(\boldsymbol{h}_k(\mathcal{A}') \boldsymbol{h}_k(\mathcal{A}')^H \boldsymbol{W}) \\ \text{s.t.} \quad & \mathrm{Tr}(\boldsymbol{W}) \leq P, \boldsymbol{W} \succeq 0, \end{aligned} \tag{3.17}$$

where the objective is now the point-wise minimum of a set of linear functions, which is concave. To handle the max-min objective, we introduce an auxiliary variable $\beta > 0$, and rewrite (3.17) as the following equivalent SDP

$$\begin{aligned} \max_{\boldsymbol{W}, \beta} \quad & \beta \\ \text{s.t.} \quad & \mathrm{Tr}(\boldsymbol{h}_k(\mathcal{A}') \boldsymbol{h}_k(\mathcal{A}')^H \boldsymbol{W}) \geq \beta, \ k = 1, \cdots, K, \\ & \mathrm{Tr}(\boldsymbol{W}) \leq P, \boldsymbol{W} \succeq 0, \beta \geq 0. \end{aligned} \tag{3.18}$$

The physical meaning of β is the power achievable by all PRs, and the non-smooth objective is now replaced by K linear constraints, which is a convex optimization problem and can be solved efficiently by any convex solver, e.g., [69]. To recover $\tilde{\boldsymbol{V}}$ from $\boldsymbol{W}$, we use eigen-decomposition, i.e., $\boldsymbol{W} = \boldsymbol{D} \boldsymbol{\Sigma} \boldsymbol{D}^H$ where $\boldsymbol{\Sigma}$ is a matrix with eigenvalues on the diagonal in decreasing order, and $\boldsymbol{D}$ is a unitary matrix with the d-th column being the normalized eigenvector corresponding to the d-th eigenvalue. Hence, the final beamforming matrix for (3.7) is extracted as $\tilde{\boldsymbol{V}}^* = \boldsymbol{D} \boldsymbol{\Sigma}'$ where $\boldsymbol{\Sigma}'$ is the left $\min(M_S, |\mathcal{A}'|)$ columns of $\boldsymbol{\Sigma}^{\frac{1}{2}}$. By Eckart-Young-Mirsky theorem[70], $\tilde{\boldsymbol{V}}^* \tilde{\boldsymbol{V}}^{*H}$ is the best rank-M_S approximation to $\boldsymbol{W}$ in terms of both the spectral and Frobenius

Algorithm 3.3 (MM-multi) - Multi-stream max-min power transfer

Input: beamspace channel matrix $\boldsymbol{H}$;

Initialization: $\mathcal{A}_0 = \emptyset$;

For $j = 1, 2, \cdots, M_{RF}$

1: Compute $n_j^* = \text{argmax}_{n \in \{1,\cdots,N\} \setminus \mathcal{A}_{j-1}} \gamma(\mathcal{A}_{j-1} \cup n)$, where $\gamma(\cdot)$ is calculated by solving the SDR problem in (3.18), followed by low rank extraction;

2: Set $\mathcal{A}_j = \mathcal{A}_{j-1} \cup n_j^*$;

End

Output: Antenna set $\mathcal{A}_{M_{RF}}$, beamformer $\boldsymbol{V}^* \in \mathbb{C}^{M_{RF} \times M_S}$, which is extracted from the solution of the SDR problem in (3.18) with antenna set $\mathcal{A}_{M_{RF}}$.

norms. The multi-stream max-min power transfer algorithm is summarized in the MM-multi algorithm in Alg. 3.3.

3.4.3 Uni-Stream Max-Min Power Transfer

For the uni-stream case, i.e., $M_S = 1$, one approach is to apply the MM-multi algorithm and extract the rank-1 solution from the optimal $\boldsymbol{W}$ of the SDR problem (3.18). However, there are two major drawbacks of the rank extraction approach. First, it is computationally inefficient since it requires to solve an SDP problem just for optimizing a single vector. Secondly, problem (3.18) does not guarantee a low-rank solution, which results that the extracted beamformer has poor performance especially when M_{RF} is large. Hence, in this subsection we propose to employ a Riemannian conjugate gradient (RCG) algorithm [71, 72] in Alg. 3.4 to solve the uni-stream max-min beamforming problem. The formulation of this problem is

$$\begin{aligned} \mathbf{Q2}: \max_{\tilde{\boldsymbol{v}} \in \mathbb{C}^{|\mathcal{A}'|}} \quad & g_{\mathcal{A}'}(\tilde{\boldsymbol{v}}) = \min_k \tilde{\boldsymbol{v}}^H \boldsymbol{h}_k(\mathcal{A}') \boldsymbol{h}_k(\mathcal{A}')^H \tilde{\boldsymbol{v}}, \\ \text{s.t.} \quad & \|\tilde{\boldsymbol{v}}\|_2^2 = P, \end{aligned} \tag{3.19}$$

for the given set $\mathcal{A}'$.

In **Q2**, the variable $\tilde{\boldsymbol{v}}$ is on the surface of an $|\mathcal{A}'|$-dimensional complex sphere with radius $\sqrt{P}$. Without loss of generality, we assume $P = 1$ and define $\mathcal{S} = \{\tilde{\boldsymbol{v}} \in \mathbb{C}^{|\mathcal{A}'|} | \tilde{\boldsymbol{v}}^H \tilde{\boldsymbol{v}} = 1\}$. Then **Q2** is equivalent to the unconstrained optimization on $\mathcal{S}$, i.e., $\max_{\tilde{\boldsymbol{v}} \in \mathcal{S}} g_{\mathcal{A}'}(\tilde{\boldsymbol{v}})$. Since the objective $g_{\mathcal{A}'}(\tilde{\boldsymbol{v}})$ is non-smooth and non-differentiable in $\tilde{\boldsymbol{v}}$, we replace it with a smooth exponential penalty function [73] $\tilde{g}_{\mathcal{A}'}(\tilde{\boldsymbol{v}})$ and the problem becomes

$$\mathbf{Q2'}: \quad \tilde{\gamma}(\mathcal{A}') = \max_{\tilde{\boldsymbol{v}} \in \mathcal{S}} \tilde{g}_{\mathcal{A}'}(\tilde{\boldsymbol{v}}), \tag{3.20}$$

where

$$\tilde{g}_{\mathcal{A}'}(\tilde{\boldsymbol{v}}) \triangleq -\frac{1}{q} \log \big(\sum_{k=1}^{K} \exp\{-q \tilde{\boldsymbol{v}}^H \boldsymbol{h}_k(\mathcal{A}') \boldsymbol{h}_k(\mathcal{A}')^H \tilde{\boldsymbol{v}}\} \big),$$

and $q \geq 0$ is a smoothing parameter which satisfies

$$\tilde{g}_{\mathcal{A}'}(\tilde{\boldsymbol{v}}) \leq g_{\mathcal{A}'}(\tilde{\boldsymbol{v}}) \leq \tilde{g}_{\mathcal{A}'}(\tilde{\boldsymbol{v}}) + 1/q \log(K). \tag{3.21}$$

When q is set appropriately, problem $\mathbf{Q2'}$ well approximates the original problem **Q2**, and it can be solved by the RCG algorithm [71].

Starting from an initial point, in each iteration the RCG algorithm first computes the gradient of the objective function at the current point $\tilde{\boldsymbol{v}}^{(j)}$ in the Euclidean space, which is given by

$$\frac{\partial}{\partial \tilde{\boldsymbol{v}}} \tilde{g}_{\mathcal{A}'}(\tilde{\boldsymbol{v}}^{(j)}) = \frac{2 \sum_{k=1}^{K} \exp\{-q \tilde{\boldsymbol{v}}^{(j)H} \boldsymbol{h}_k(\mathcal{A}') \boldsymbol{h}_k(\mathcal{A}')^H \tilde{\boldsymbol{v}}^{(j)}\} \big(\boldsymbol{h}_k(\mathcal{A}') \boldsymbol{h}_k(\mathcal{A}')^H \tilde{\boldsymbol{v}}^{(j)} \big)}{\exp\{-q \tilde{\boldsymbol{v}}^{(j)H} \boldsymbol{h}_k(\mathcal{A}') \boldsymbol{h}_k(\mathcal{A}')^H \tilde{\boldsymbol{v}}^{(j)}\}}. \tag{3.22}$$

In step 2, the Riemannian gradient [71] is calculated based on the Euclidean gradient. Define the tangent space of a point on the spherical manifold $\tilde{\boldsymbol{v}} \in \mathcal{S}$ as

$$T_{\tilde{\boldsymbol{v}}} \mathcal{S} = \{\boldsymbol{x} \in \mathbb{C}^{|\mathcal{A}'|} | \tilde{\boldsymbol{v}}^H \boldsymbol{x} + \boldsymbol{x}^H \tilde{\boldsymbol{v}} = 0\}, \tag{3.23}$$

and the Riemannian gradient is given by

$$\boldsymbol{w}^{(j)} = \mathrm{Rgrad}_{\tilde{\boldsymbol{v}}} g_{\mathcal{A}'}(\tilde{\boldsymbol{v}}^{(j)}) = (\boldsymbol{I} - \tilde{\boldsymbol{v}}^{(j)} \tilde{\boldsymbol{v}}^{(j)H}) \frac{\partial}{\partial \tilde{\boldsymbol{v}}} \tilde{g}_{\mathcal{A}'}(\tilde{\boldsymbol{v}}^{(j)}). \tag{3.24}$$

Algorithm 3.4 (RCG) - Riemannian conjugate gradient

Input: beamspace channel matrix $\boldsymbol{H}(\mathcal{A}')$ with given $\mathcal{A}'$, initial point $\tilde{\boldsymbol{v}}^{(0)}$;

Initialization: compute $\boldsymbol{w}^{(0)}$ using (3.24), let $\boldsymbol{d}^{(0)} = \boldsymbol{w}^{(0)}$, $\tilde{\boldsymbol{v}}^{(1)} = \tilde{\boldsymbol{v}}^{(0)}$, $j = 1$;

Repeat

1: Compute Euclidean partial derivative $\frac{\partial}{\partial \tilde{\boldsymbol{v}}} \tilde{g}_{\mathcal{A}'}(\tilde{\boldsymbol{v}}^{(j)})$ using (3.22)

2: Compute Riemannian gradient $\boldsymbol{w}^{(j)}$ using (3.24);

3: Compute search direction $\boldsymbol{d}^{(j)}$ using (3.26) and (3.27),

If $\text{Real}(\langle \boldsymbol{w}^{(j)}, \boldsymbol{d}^{(j)} \rangle) < 0$, **Then** $\boldsymbol{d}^{(j)} = \boldsymbol{w}^{(j)}$;

4: Compute Armijo step size $\theta^{(j)}$ via backtracking line-search;

5: Update $\tilde{\boldsymbol{v}}^{(j+1)}$ using (3.28);

6: $j \leftarrow j + 1$;

Until convergence

Output: converged beamformer vector $\tilde{\boldsymbol{v}}^{(j)}$.

Essentially, the Riemannian gradient is the projection of the Euclidean gradient onto the tangent space at $\tilde{\boldsymbol{v}}^{(j)}$.

In the key step 3, the conjugate gradient $\boldsymbol{d}^{(j)}$ is computed, which is also the search direction of the RCG algorithm. The conjugate gradient combines the Riemannian gradient vector $\boldsymbol{w}^{(j)}$ calculated in step 2 at the current iteration and the search direction vector $\boldsymbol{d}^{(j-1)}$ in the previous iteration. Since the two vectors belong to different tangent spaces, $\boldsymbol{d}^{(j-1)}$ needs to be transported to the tangent space of $\boldsymbol{w}^{(j)}$ to ensure the operation is meaningful. Define the vector transport operation from $\boldsymbol{u}$ to the tangent space of $\tilde{\boldsymbol{v}}$ as

$$H_{T_{\tilde{\boldsymbol{v}}}\mathcal{S}}(\boldsymbol{u}) = (\boldsymbol{I} - \tilde{\boldsymbol{v}}\tilde{\boldsymbol{v}}^H)\boldsymbol{u}. \tag{3.25}$$

The conjugate gradient is then calculated by

$$\boldsymbol{d}^{(j)} = \boldsymbol{w}^{(j)} + \beta \boldsymbol{x}, \tag{3.26}$$

where $\boldsymbol{x} = H_{T_{\tilde{\boldsymbol{v}}^{(j)}}\mathcal{S}}(\boldsymbol{d}^{(j-1)})$, and β is a weight coefficient given by

$$\beta = \max\left(0, -\frac{\text{Real}\{(\boldsymbol{w}^{(j)} - \boldsymbol{z})^H \boldsymbol{w}^{(j)}\}}{\text{Real}\{(\boldsymbol{w}^{(j)} - \boldsymbol{z})^H \boldsymbol{x}\}}\right), \tag{3.27}$$

where $\boldsymbol{z} = H_{T_{\tilde{\boldsymbol{v}}^{(j)}}\mathcal{S}}(\boldsymbol{w}^{(j-1)})$. The choice of weight β is known as the modified Hestens-Stiefel rule [74]. Then, the RCG algorithm checks if the search direction computed in step 3 is gradient related [71], i.e., its inner product with $\boldsymbol{w}^{(j)}$ is positive, and is reset to $\boldsymbol{w}^{(j)}$ if it is negative. This step ensures that $\boldsymbol{d}^{(j)}$ is aligned with $\boldsymbol{w}^{(j)}$, which is an ascending direction. The algorithm then updates the beamformer vector as

$$\tilde{\boldsymbol{v}}^{(j+1)} = \frac{\tilde{\boldsymbol{v}}^{(j)} + \theta^{(j)}\boldsymbol{d}^{(j)}}{\|\tilde{\boldsymbol{v}}^{(j)} + \theta^{(j)}\boldsymbol{d}^{(j)}\|}, \tag{3.28}$$

where $\theta^{(j)}$ is an adaptive step size according to the Armijo rule [71]. In particular, $\theta^{(j)}$ is initialized as 1. It keeps decreasing its value, i.e., $\theta^{(j)} \leftarrow \mu\theta^{(j)}$ with $\mu \ll 1$, until the following Armijo rule is satisfied:

$$\tilde{g}_{\mathcal{A}'}(\tilde{\boldsymbol{v}}^{(j+1)}) - \tilde{g}_{\mathcal{A}'}(\tilde{\boldsymbol{v}}^{(j)}) \geq 10^{-4}\theta^{(j)}\text{Real}\{\boldsymbol{w}^{(j)H}\boldsymbol{d}^{(j)}\}. \tag{3.29}$$

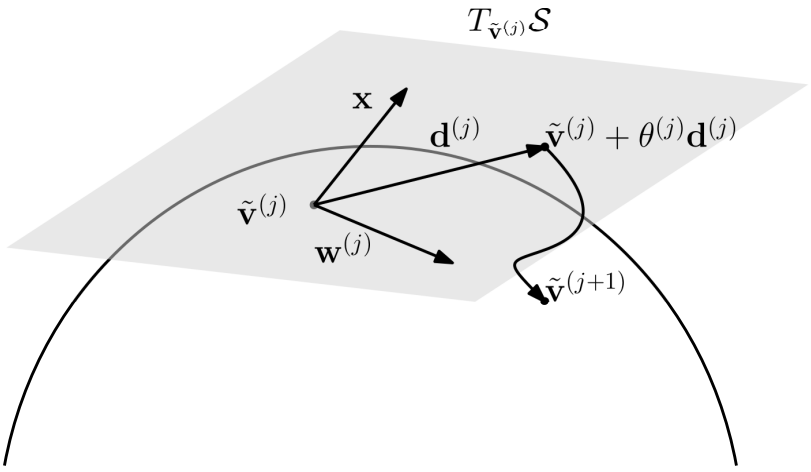

Figure 3.2: Geometric interpretation of the RCG algorithm.

This procedure of tuning the step size is often referred to as the backtracking line-search, which not only guarantees that the algorithm is non-decreasing, but also prevents slow convergence due to the step size being too small. The RCG algorithm stops when the norm of the Riemannian gradient falls below a threshold, i.e., $\|\boldsymbol{w}^{(j)}\|^2 < \epsilon$. The algorithm is geometrically illustrated in Fig. 3.2.

The RCG algorithm guarantees that every limit point of the sequence $\{\tilde{\boldsymbol{v}}^{(j)}\}$ generated is a stationary point according to the convergence results on the backtracking line-search [71, Th. 4.3.1]. The final output beamformer is thus a stationary point of the objective function $\tilde{g}_{\mathcal{A}'}(\tilde{\boldsymbol{v}})$ in (3.20).

As in the SUM1 algorithm, by employing the greedy-based outer loop to select the antenna set, we present the MM-uni algorithm for uni-stream max-min power transfer. The initial beamforming vector is set to 1. In each iteration, it searches for the best antenna to add to the existing set similar to the MM-multi algorithm. The difference is that now the RCG algorithm is employed. In this step, the same initial point is used for all candidates antennas to start with. The antenna which brings in the highest power gain is added in step 2, and the optimal beamforming vector is updated as the output of the RCG algorithm with the current antenna set. The optimal beamforming vector is also set as the initial point of the next

Algorithm 3.5 (MM-uni) - Uni-stream max-min power transfer

Input: beamspace channel matrix $\boldsymbol{H}$;

Initialization: $\mathcal{A}_0 = \emptyset$, $\boldsymbol{v}_1^{(0)} = 1$;

For $j = 1, 2, \cdots, M_{RF}$**:**

1: Compute $n_j^* = \text{argmax}_{n \in \{1,\cdots,N\} \setminus \mathcal{A}_{j-1}} \tilde{\gamma}(\mathcal{A}_{j-1} \cup n)$, where function $\tilde{\gamma}(\cdot)$ is calculated by the RCG algorithm with initial point $\boldsymbol{v}_j^{(0)}$;

2: Set $\mathcal{A}_j \leftarrow \mathcal{A}_{j-1} \cup n_j^*$;

3: Set $\boldsymbol{v}_j$ as the output of the RCG algorithm with input $\boldsymbol{H}(\mathcal{A}_j)$;

4: Set $\boldsymbol{v}_{j+1}^{(0)} \leftarrow [\boldsymbol{v}_j; 0]$;

End

Output: Antenna set $\mathcal{A}_{M_{RF}}$, beamformer $\tilde{\boldsymbol{v}}^* \in \mathbb{C}^{M_{RF}}$ which maximizes $\tilde{g}_{\mathcal{A}_{M_{RF}}}$ in (3.20).

iteration. Since the vector size is increased by 1 in the next iteration, a 0 is padded to the end of the current beamforming vector. The reason to use the beamforming vector in the previous iteration as the initial point is that the antennas in the current set are supposed to contribute most of the power transfer, which means that the current beamforming vector still plays a dominant role when more antennas are added, and hence the updated beamformer with one more antenna is believed to be in the neighborhood of the previous iteration.

The MM-uni algorithm in Alg. 3.5 has a much lower computational complexity than the MM-multi algorithm for single stream power transfer due to the efficient RCG algorithm. The difference can be clearly seen by comparing the variable sizes of the two algorithms. In each iteration, e.g., at the final iteration $j = M_{RF}$, for the MM-uni algorithm, the optimization variable is the beamformer vector $\tilde{\boldsymbol{v}}$, whose size is $M_{RF} \times 1$. On the other hand in the SDR based MM-multi algorithm, each beamformer vector is transformed into a semidefinite matrix $\boldsymbol{W}$ which has size $M_{RF} \times$

M_{RF}. One can clearly observe that the variable size of the MM-multi algorithm is the square of that of the MM-uni algorithm, and so does the size of the gradient. As a result, even using the first-order method, the SDR approach has significantly higher computational complexity than the RCG algorithm. Second-order methods will be even worse due to the large-size Hessian matrices. Therefore, the MM-uni algorithm has much lower complexity than the MM-multi algorithm. Furthermore, the MM-uni algorithm guarantees that the objective value is non-decreasing as the size of the antenna set grows, and this does not hold for the SDR approach. This is because when the set size increases, the rank of the SDR solution tends to increase as well. As a result, it can often be observed that the rank-1 extraction solution of the SDR approach exhibits worse performance even when the antenna size increases. Hence, the MM-uni algorithm has advantages over the MM-multi algorithm in both computational complexity and performance for uni-stream power transfer.

3.5 Simulation Results

In this section, we illustrate the power transfer performance via simulations. We consider the following general simulation settings unless specified otherwise. The simulations were run on a desktop with 20 GB RAM and 3.5 GHz CPU, and all results were averaged over 100 channel realizations.

System Setting: We employ the lens antenna array beamspace MIMO system presented in Section 3.2 with $N = 32$ antennas and $M_{RF} = 8$ RF chains. All transmitting and receiving antennas have 10 dBi gains. There are $K = 8$ PRs. The distance between each PR k and the PT, d_k, is uniformly distributed in the range of 10-15 meters.

Channel Setting: For the mmWave channel model in (3.2), there is a LoS path and $L = 2$ scattering paths with $\alpha_{k,0} \sim \mathcal{CN}(0, 2)$ and $\alpha_{k,l} \sim \mathcal{CN}(0, 0.4)$, $l = 1, 2$. The signal directions $\{\theta_{k,l}\}$ are i.i.d. uniformly distributed in $[0, 2\pi]$. The system

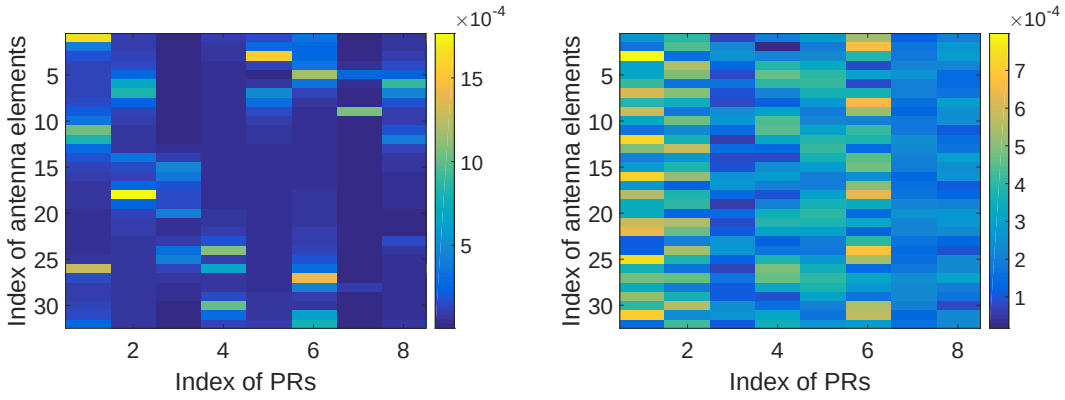

(a) Beamspace MIMO (b) Conventional MIMO

Figure 3.3: Channel gain of each antenna-PR pair for both MIMO systems.

is assumed to operate at $f_{\text{carrier}} = 24$ GHz carrier frequency, and the path-loss is calculated as $\varrho_k = (4\pi f_{\text{carrier}} d_k/c)^2$ where c is the speed of light.

First of all we illustrate the channel sparsity of the beamspace MIMO system. Fig. 3.3 shows the matrices of channel gains between the transmitter antenna array and receivers for the beamspace MIMO and conventional MIMO systems in one realization. It can be clearly observed that for the beamspace MIMO most antenna-PR pairs have very small gains and only a few ones have large values. In contrast for the conventional MIMO system, the variations of channel gains are much smaller, thus the channel is less sparse. This result can also be illustrated by comparing their empirical CDF plots in Fig. 3.4.

3.5.1 Sum Power Transfer

We first consider the sum power transfer problem, and we compare the proposed SUM1 and SUM2 algorithms, and the following baselines.

- MC-ED: the maximum channel gain criterion [58] is considered, where the antennas are selected based on the channel gains. Specifically, the norm of the channel gain vector of each antenna element to all K receivers is calculated,

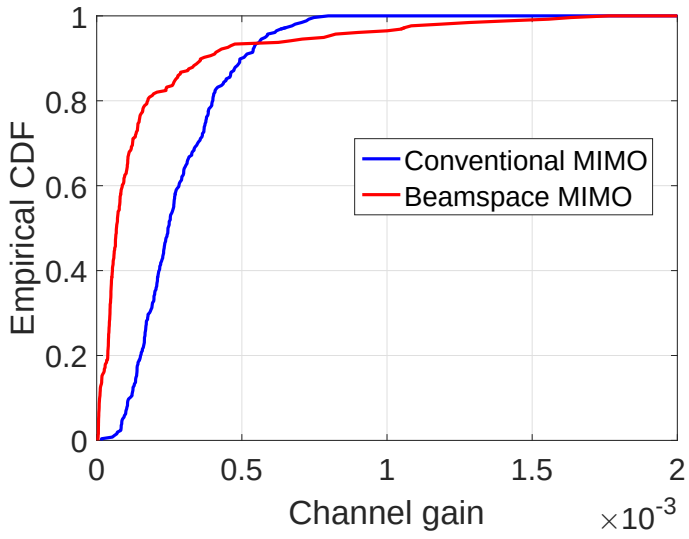

Figure 3.4: Empirical CDF of the channel gain for beamspace MIMO and conventional MIMO.

and the antennas with the top M_{RF} gains are selected. Given this set of antennas, the beamformers are optimized using eigen-decomposition as discussed in Section 3.3.2.

- MIMO1 & MIMO2: in these two baselines the transmitter is not equipped with the lens array, and the conventional uniform linear array is employed. The SUM1 and SUM2 algorithms are employed respectively for antenna selection and beamformer design.

Two performance upper bounds are also illustrated as benchmarks.

- FD: in this fully digital baseline the transmitter has N RF chains, and all antennas are used. This gives the overall performance upper bound of the system. The optimal beamformer is obtained by eigen-decomposition.

- U-UB: this is the performance upper bound of the uni-stream transmission which is given by solving the semidefinite program **P3.2** in (3.12)-(3.13).

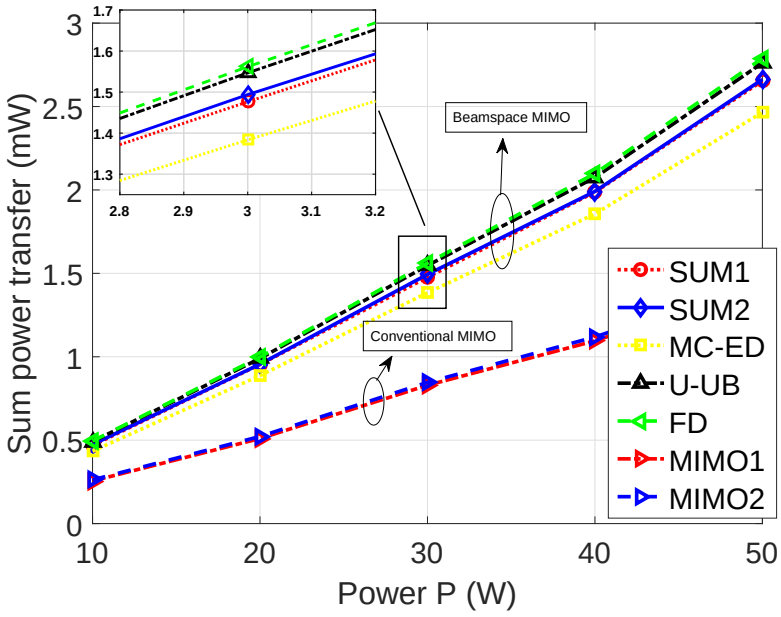

Figure 3.5: Sum power transferred versus varying input power P.

In the first simulation we let $M_{RF} = 8$ and vary the input power P. The result is shown in Fig. 3.5. It can be observed that the energy transfer increases linearly with the input power for all baseline methods. Among all baselines, the FD system achieves the highest power transfer, which is in fact the upper bound of the whole system since it enables the maximum degrees of freedom in the beamformer design. The U-UB is slightly lower than FD due to the constraint on the number of RF chains. The SUM1 algorithm shows very impressive power transfer performance: when the input power is P =30 W, it achieves 94.4% of the FD bound. The SUM2 algorithm achieves even better performance, i.e., it achieves 96.5% of the U-UB bound and 95.6% of the FD bound.

As discussed earlier, the SUM2 algorithm has a much lower complexity than the SUM1 algorithm. In this case it also demonstrates superior power transfer performance mainly due to two reasons. The first reason is that the initial point of the SUM2 algorithm corresponds to the upper bound of the problem, and the local optimum near the upper bound solution yields near-optimal performance. The second

reason is that the SUM2 algorithm yields monotonically increasing objective function value, and hence finds the local optimum efficiently. Specifically, we demonstrate the convergence of the SUM2 algorithm for one channel realization in Fig. 3.6. It can be observed that it converges very fast, i.e., within 12 iteration. Since the computation complexity in each iteration is very low, the overall running time of the SUM2 algorithm is much shorter than that of the SUM1 algorithm which needs to perform a series of eigen-decompositions. In this example the SUM2 algorithm takes less than 5% of the running time of the SUM1 algorithm. Specifically, the running time of the SUM1 algorithm is 65.9 ms while that of the SUM2 algorithm is only 3.25 ms.

Back to Fig. 3.5, we can easily see that both proposed algorithms outperform the MC-ED baseline. The performance gain of the SUM1 algorithm over the MC-ED baseline is essentially the improvement of the greedy-based antenna selection over the maximum channel gain criterion. On the other hand, all the beamspace MIMO baselines, which equip the transmitter with the lens antenna array, significantly outperform and almost double the power throughput of the MIMO1 and MIMO2 baselines that employ the conventional multi-antenna transmitter. The performance improvement comes from the fact that the channel is more sparse in the beamspace domain, i.e., for each PR there are only a few antenna elements that have strong channel gains. Hence, when the number of RF chains is small the beamspace MIMO system can be much more efficient as the transmitter just needs to focus on those antennas with strong gains. Therefore, the beamspace MIMO with lens antenna array considered in this chapter can significantly increase the efficiency of wireless power transfer.

In Fig. 3.7 the blockage effect [75] is studied. In this simulation, we set $P = 30$ W and $M_{RF} = 12$, and vary the blockage probability. When the blockage probability is 0, there is no block and the channel model is the same as that in Fig. 3.5. When the blockage probability is 1, the LoS path of each receiver is blocked and only the scattering paths exist. It can be seen that the performances of all schemes decrease as the blockage probability increases, since the LoS path that has the dominant channel

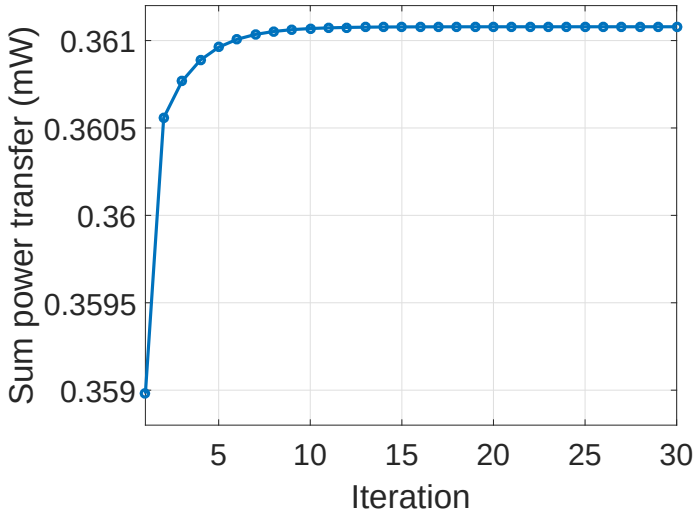

Figure 3.6: Convergence of the SUM2 algorithm.

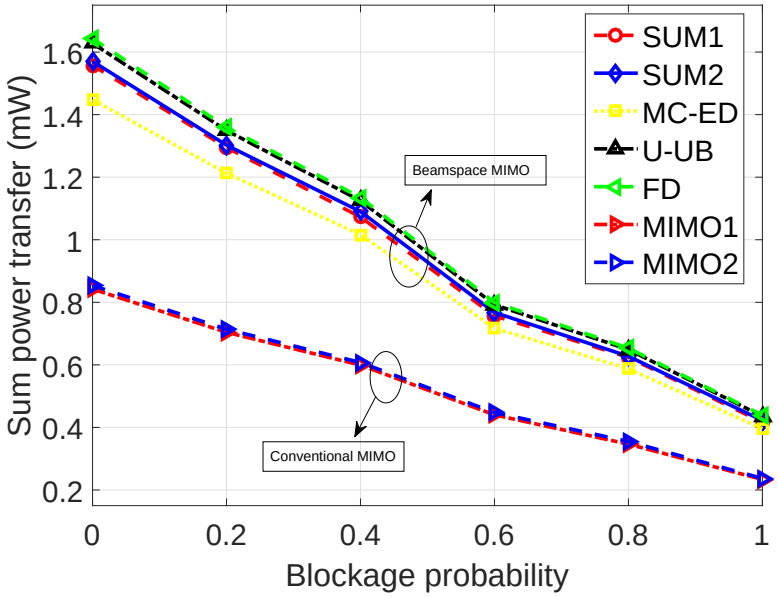

Figure 3.7: Sum power transferred versus blockage probability.

gain is more likely to be blocked, which results in system performance degradation. Similarly as in Fig. 3.5 the beamspace MIMO outperforms the conventional MIMO.

In the next simulation the power input is fixed as $P = 30$ W and we investigate the

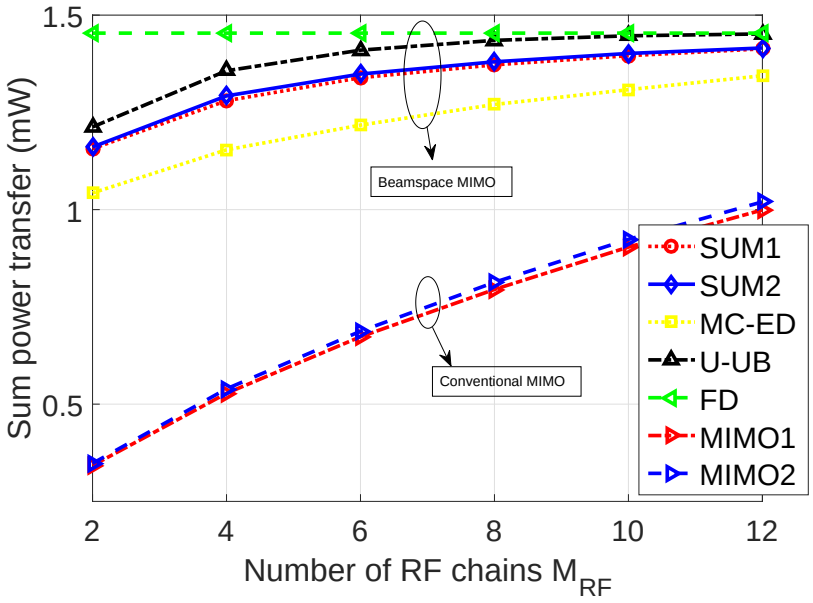

Figure 3.8: Sum power transferred versus number of RF chains M_{RF}.

system performance with varying number of RF chains. In Fig. 3.8, it can be seen that the total amount of transferred power increases as the number of RF chains increases for all baselines, because increasing the number of RF chains allows higher degrees of freedom in beamformer design, which leads to higher power transfer. However, the extra performance gain diminishes as more RF chains are added. The reason is that the beamspace mmWave channel model is sparse, such that only a few beams dominate the capacity of power transfer. That is, a small number of antenna elements which are associated with strong channel gains contribute to the majority portion of the power delivery, and the other antennas play a less important role compared with those dominant ones. Same as in Fig. 3.5, the SUM2 algorithm exhibits the best performance for all values of M_{RF}, and the SUM1 algorithm outperforms the baseline approach using the MC antenna selection criterion. Finally, it is clear that the beamspace MIMO baselines outperform the conventional MIMO systems.

In Fig. 3.9 we set $M_{RF} = 16$ and $P = 30$ W and increase the total number of antenna elements N. The result is shown using SUM2 algorithm. It is clear that the

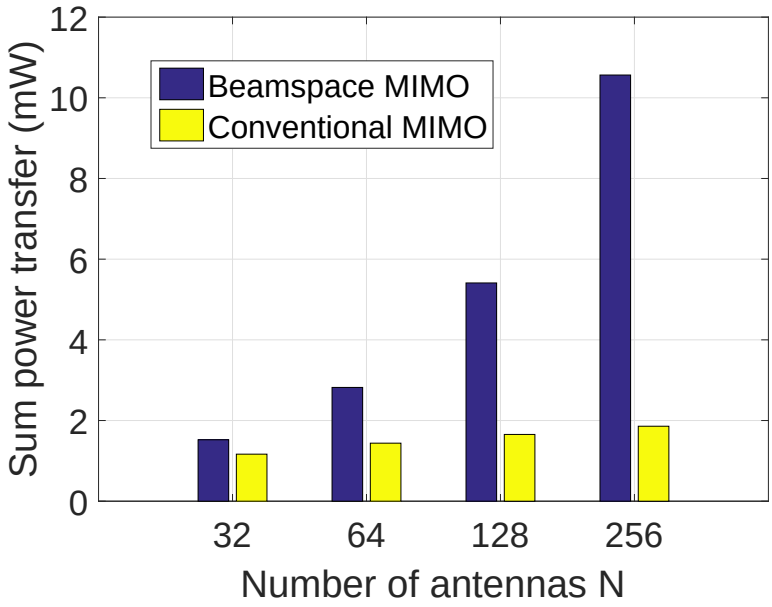

Figure 3.9: Sum power transferred versus number of antennas N (SUM2 algorithm).

beamspace MIMO outperforms the conventional MIMO. Specifically, the sum power increases linearly with respect to N for the beamspace MIMO, while the performance gain diminishes for the conventional MIMO. This result illustrates that large-scale beamspace MIMO is a particularly well suited for WPT application, since increasing the number of antennas can improve the performance while the costly RF chain circuits remain unchanged.

The effect of the non-linearity in power conversion [51, 76] is investigated in Fig. 3.10. These works suggest that for practical energy harvesting circuits, the harvested power has a non-linear relationship to the incident power at the antennas. In this simulation, we set $M_{RF} = 8$ and $P = 30$ W, and we employ the non-linear power conversion model in [51] to compare its performance to the linear model considered in this chapter. It can be observed that for all baselines, the sum power throughput under the non-linear model is a fraction of the counterparts under the linear model due to practical limits. However, the proposed SUM1 and SUM2 algorithms, which generate higher transferred power in linear model, also enable higher power through-

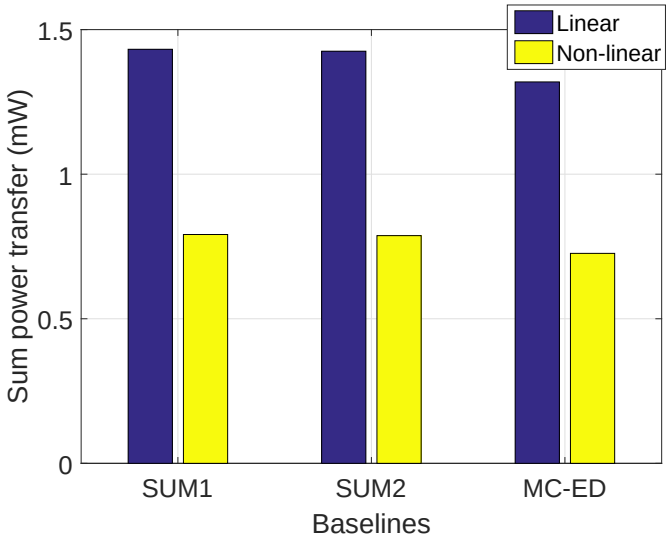

Figure 3.10: Comparison to non-linear energy conversion models.

put in the non-linear model. This is because the harvested power is monotonically increasing with respect to the incident power, and that is what SUM1 and SUM2 algorithms are optimized for. Hence, the proposed methods can be extended to the power transfer problems in non-linear energy conversion models.

From the above simulation results, it is important to note that the beamspace MIMO system with lens antenna array is very cost efficient in terms of power transfer. For example in Fig. 3.5 the system with only 1/4 active antenna elements can achieve over 90% of the system output with fully deployed antennas, which is far beyond the reach of the conventional MIMO system with ULA. Hence, the beamspace MIMO system shows its great potential in wireless power transfer applications.

3.5.2 Max-Min Power Transfer

In this subsection we evaluate the system performance in terms of max-min power transfer. Both multi-stream ($M_S = 3$) and uni-stream transmissions are considered. We demonstrate the performances of the proposed MM-multi and MM-uni algorithms and compare them with the following baselines.

- MC-SDR: the maximum channel gain criterion [58] is used. Given the chosen set of antennas, the multi-stream beamformers are optimized by solving the SDR problem in (3.17).

- MIMO-multi: in this baseline the transmitter is not equipped with the lens, and the conventional uniform linear array transmitter is employed. Multi-stream power transfer with $M_S = 3$ is considered in this baseline and MM-multi algorithm is employed for antenna selection and beamformer design.

- MIMO-uni: similar to the MIMO baseline the conventional ULA transmitter is employed. Uni-stream power transfer is considered and the MM-uni algorithm is employed.

Similar to the sum power transfer case, two performance upper bounds are illustrated as benchmarks.

- FD: the transmitter has N RF chains, and all antennas are used. The optimal beamformer is obtained by solving the SDR problem in (3.17).

- U-UB: this is the performance upper bound of the uni-stream transmission which is given by solving the following semidefinite program

$$\begin{aligned} \max_{\boldsymbol{W}\in\mathbb{C}^{N\times N},\beta} \quad & \beta \\ \text{s.t.} \quad & \mathrm{Tr}(\boldsymbol{h}_k\boldsymbol{h}_k^H\boldsymbol{W}) \geq \beta,\ k = 1, \cdots, K, \\ & \mathrm{Tr}(\boldsymbol{W}) \leq P, \boldsymbol{W} \succeq 0, \beta \geq 0, \\ & \mathbf{1}^T|\boldsymbol{W}|\mathbf{1} \leq M_{RF}P. \end{aligned} \tag{3.30}$$

We first show the result of the max-min power transfer versus the number of RF chains M_{RF} in Fig. 3.11. The system parameters are the same as those in Fig. 3.8. By the same reason as in the sum power problem, the performance of the max-min power transfer improves as M_{RF} increases, and the performance gain diminishes as M_{RF} becomes closer to N for all baselines except for MM-multi ($M_S = 1$). However,

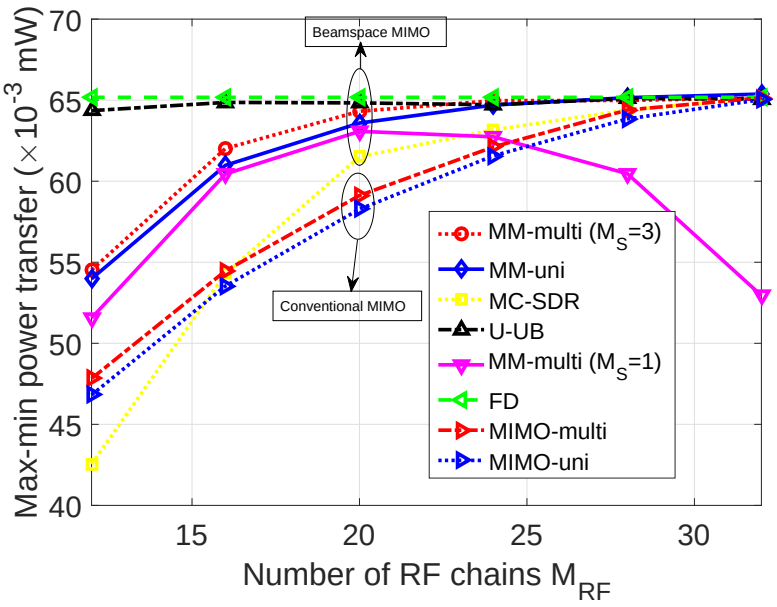

Figure 3.11: Max-min power transferred versus number of RF chains M_{RF}.

there are several significant differences from the sum power transfer problem. First of all, we observe that the performance of the MM-multi algorithm degrades for uni-stream transmission ($M_S = 1$) when M_{RF} increases from 20 to 32. Interestingly on the other hand, for multi-stream transmission ($M_S = 3$), its performance improves and converges to the FD upper bound. Indeed, the only difference between these two cases is that the beamformer design subproblem enforces to extract the rank-1 solution for $M_S = 1$ and rank-M_S solution for $M_S = 3$. This result illustrates that when M_{RF} is close to N, the optimal solution of the beamformer design problem in (3.18) tends to have rank great than 1, the uni-stream transmission actually degrades the performance compared to the result corresponding to smaller M_S. On the other hand, the performance of the proposed MM-uni algorithm is more stable. It has better performance when the number of RF chain is small, and it guarantees the power throughput grows monotonically as M_{RF} increases. Moreover, the computational complexity is much lower for the MM-uni algorithm. For example, for uni-stream transmission with $M_{RF} = 12$, the average running time of the MM-uni

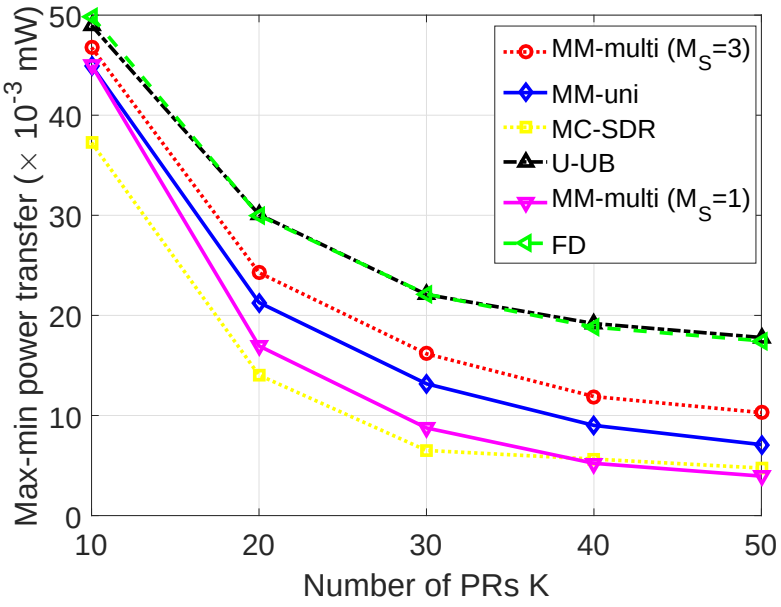

Figure 3.12: Max-min power transferred versus number of PRs K.

algorithm is only 14.7 s and that of the MM-multi algorithm is 123.5 s. Fig. 3.11 also illustrates another feature of the max-min power transfer that multi-stream outperforms uni-stream. This is because a single stream can hardly serve all PRs with different channel gains, and additional streams provide higher spatial multiplexing gain. Another observation from Fig. 3.11 is that the upper bound of the uni-stream max-min power transfer is not as tight as that of the sum power transfer when M_{RF} is small. This is also due to the fact that the solution to (3.30) tends to have rank greater than 1, which leads to large gap between the optimal solution of the relaxed problem and a rank feasible solution. Finally, the beamspace MIMO outperforms the conventional MIMO again for the max-min power transfer, especially when M_{RF} is small for the multi-stream case, e.g., when $M_{RF} = 12$ the beamspace MIMO system achieves 13% higher power output than the conventional MIMO baselines.

In the next simulation, we set $P = 30$ W and $M_{RF} = 16$, and vary the number of PRs K. All other parameters are the same as in Fig. 3.11. The result is shown in Fig. 3.12. As expected, the max-min power transferred decreases as K increases

for all baselines, since when K increases it is more difficult to maintain the same power throughput for all PRs with the same level of power supply. An interesting observation is that the gap between the uni-stream case (MM-multi ($M_S = 1$) or MM-uni) and multi-stream case (MM-multi ($M_S = 3$)) increases as K increases. This is because the optimal solution tends to have higher rank as K increases, which is due to the increasing size of the channel matrix. Therefore in general, the system should adopt the uni-stream scheme when K is small and the multi-stream scheme when K is large.

3.6 Conclusions

In this chapter, we have studied wireless power transfer (WPT) by beamspace MIMO systems with lens antenna arrays. By taking advantage of the channel sparsity of the beamspace MIMO, fewer RF chains are required to achieve comparable power throughput as the conventional MIMO system, which effectively reduces the hardware cost and circuit power consumption. We have formulated two WPT design problems for the beamspace MIMO with constraints on the number of RF chains, the sum power maximization problem and max-min power problem, and both of them are NP-hard. For maximum sum power transfer, we showed that the uni-stream transmission is optimal and the proposed SUM2 algorithm based on the truncated power method is efficient for joint antenna selection and beamformer design. For the max-min power transfer, we proposed algorithms for both multi-stream and uni-stream transmissions. Extensive simulation results demonstrate that for both problems, the proposed algorithms outperform a number of heuristic approaches. More importantly, the beamspace MIMO significantly outperforms the conventional MIMO, in terms of WPT efficiency especially when the number of RF chains is limited.

3.7 Appendices

3.7.1 Proof of Lemma 1

For convenience we denote $\boldsymbol{H} = \boldsymbol{H}(\mathcal{A}')$. It is obvious that $f_{\mathcal{A}}(\tilde{\boldsymbol{V}})$ achieves the optimum on the boundary, i.e., $\mathrm{Tr}(\tilde{\boldsymbol{V}}^H\tilde{\boldsymbol{V}}) = P$. Hence, the Lagrange function of the problem in (3.7) with equality constraint is

$$\mathcal{L}(\tilde{\boldsymbol{V}}, \lambda) = \mathrm{Tr}(\tilde{\boldsymbol{V}}^H\boldsymbol{H}\boldsymbol{H}^H\tilde{\boldsymbol{V}}) + \lambda(P - \mathrm{Tr}(\tilde{\boldsymbol{V}}^H\tilde{\boldsymbol{V}})), \tag{3.31}$$

where λ is the Lagrange multiplier. According to the KKT conditions, $\tilde{\boldsymbol{V}}$ is optimal only if

$$\begin{aligned}\frac{\partial}{\partial\tilde{\boldsymbol{V}}}\mathcal{L}(\tilde{\boldsymbol{V}}, \lambda) &= \boldsymbol{H}\boldsymbol{H}^H\tilde{\boldsymbol{V}} + (\boldsymbol{H}\boldsymbol{H}^H)^H\tilde{\boldsymbol{V}} - 2\lambda\tilde{\boldsymbol{V}} \\ &= 2\boldsymbol{H}\boldsymbol{H}^H\tilde{\boldsymbol{V}} - 2\lambda\tilde{\boldsymbol{V}} \\ &= 0.\end{aligned}$$

Hence, $\boldsymbol{H}\boldsymbol{H}^H\tilde{\boldsymbol{V}} = \lambda\tilde{\boldsymbol{V}}$, which means that λ is an eigenvalue of $\boldsymbol{H}\boldsymbol{H}^H$ and columns of $\tilde{\boldsymbol{V}}$ are eigenvectors corresponding to λ. Therefore we have $f_{\mathcal{A}}(\tilde{\boldsymbol{V}}) = \lambda^*\mathrm{Tr}(\tilde{\boldsymbol{V}}^H\tilde{\boldsymbol{V}}) = \lambda^*P$ where λ^* is the largest eigenvalue of $\boldsymbol{H}\boldsymbol{H}^H$, and the optimal $\tilde{\boldsymbol{V}}$ is in the eigenspace of $\boldsymbol{H}\boldsymbol{H}^H$ corresponding to λ^*.

3.7.2 Proof of Theorem 1

By Lemma 1, the optimal $\tilde{\boldsymbol{V}}$ is in the eigenspace of $\boldsymbol{H}\boldsymbol{H}^H$ which corresponds to its largest eigenvalue λ^*. Suppose that the multiplicity of λ^* is M, and $\boldsymbol{v}_1, \cdots, \boldsymbol{v}_M$ are the orthonormal eigenvectors corresponding to λ^*. Then we can simply choose, e.g., $\tilde{\boldsymbol{V}} = [\sqrt{P}\boldsymbol{v}_1, \boldsymbol{0}, \cdots, \boldsymbol{0}]$ so that

$$f_{\mathcal{A}}(\tilde{\boldsymbol{V}}) = P\boldsymbol{v}_1^H\boldsymbol{H}\boldsymbol{H}^H\boldsymbol{v}_1 = \lambda^*P.$$

Therefore, single-stream transmission using any of the dominant eigenvectors as the beamformer is optimal.

Part II

Network Optimization for Wireless Power Transfer and Backscatter Communication Systems

Chapter 4

Energy Allocation and Utilization for Wireless Powered Networks

4.1 Introduction

In this chapter, we study energy allocation and utilization for wireless powered sensor networks. The rapid development of the IoT technologies enables easy access and control of a variety forms of information and data, and leads novel applications such as smart home, smart factory, etc. However, due to the small sizes and different operating environments of the IoT sensors, it is hard to directly power the sensors from the grid and batteries are usually employed to power the sensors. Hence, sensor charging and efficient energy utilization become key challenges and are currently under active research. A significant amount of works consider the energy harvesting communication models, where the wireless sensor devices can harvest energy from an external source in their natural environment, for example in the form of sun light [77], vibration [78], etc. Specifically, when the full knowledge of energy arrival is assumed to be known in advance, the throughput maximization problem is studied in [79]. When such information is not observable in advance, online scheduling methods are considered. Water filling algorithm is used in [80] to find the optimal policy that

maximizes the data throughput for a single sensor. In [14] the learning theoretic approaches are considered to find the optimal transmission policy for point-to-point communication. Based on channel state and energy queue length, the work in [81] considers the successful packets delivery maximization problem. Some works consider the power allocation between data acquisition and transmission [82] [83]. Also, energy cooperation is studied in multi-sensor network [84]. The transmission scheme optimization problem is considered in [85] such that the data transmission with finite-length can be completed in the shortest time. Recently, an interesting work further takes into account the non-ideal characterization of the batteries with internal resistance [86]. The user association and power allocation problems are studied in [87] where the base stations harvest energy to improve the transmission efficiency. However this work does not consider energy harvesting as the power source. However, such energy harvesting model has several limitations. Firstly, the stochastic nature of the energy arrival makes the model less controllable or stable. Secondly, the resource of the natural energy may not be immediately available in the ambient surroundings of the sensors, and this is particularly true for some scenarios of the IoT applications. Consider the smart home application as a motivating example. All sensors are connected to form an IoT network, i.e., thermo sensors for air conditioning and heating systems, signal detect sensors for smart lock system, motion and sound sensors for security and surveillance systems, etc. Since this is an indoor environment, the network sensors cannot be charged by the unavailable external sources like sunlight or vibration. Hence, other forms of energy transmission are urgently demanded to serve such scenarios.

On the other hand, the development of RF power transfer in the past few decades provides another paradigm. In particular, recent advancement shows that the wireless power transfer efficiency and distance can be improved using multi-antenna setup [41][88][89], millimeter wave [90], etc. Long distance wireless power transfer has been enabled, and network architecture has been proposed based on the technique.

Recently, RF energy harvesting and transfer for spectrum sharing IoT network is studied in [91]. The RF power transfer has several nice characteristics. Firstly, the wireless power transfer essentially enables more flexibility in IoT sensor placement planning. Secondly, the RF power transfer is controllable. The rate of power transfer can be effectively controlled by changing the strength of the radiating power. Hence, the RF power transfer is more reliable and easily managed than the energy harvesting model.

In this chapter, we consider an RF powered IoT network system, where there is a central node and multiple RF powered sensors. The central node is an RF power transmitter (charger), and it transmits (RF) power to the sensors. Each sensor is equipped with a battery. The sensors harvest the RF power from the central node, and store the energy in their batteries. On the other hand, the sensors utilize the energy stored in their batteries to transmit data to the central node. The objective is to maximize the total data throughput of all sensors. The remotely powered communication model is studied in [92] from an information-theoretic point of view. Note that our considered model is fundamentally different from another line of work, the SWIPT [93] [53]. For SWIPT, the transmitter transmits both information and power, while in this model the power transmitter is the information receiver and vice versa. In this problem, too many factors are coupled which makes the overall objective complicated to analyze. We break the problem into two subproblems: the sensor battery energy utilization problem and the charging power allocation problem of the central node, and the technical challenges are to find efficient methods to solve both subproblems. The main contributions of this chapter are summarized as follows.

- To the best of our knowledge, this is the first work on resource allocation for wirelessly powered IoT system.
- We formulate the sensor energy utilization problem as a finite-horizon MDP. We show several important properties of the value function based on which we propose an optimal energy utilization algorithm with reduced search space of

possible actions.

- We show that the total value function of the sensors under a given power allocation satisfies the M-EXC property. We then propose an optimal power allocation algorithm based on the discrete steepest ascent method that has a significantly lower complexity than exhaustive search.

4.2 System Descriptions

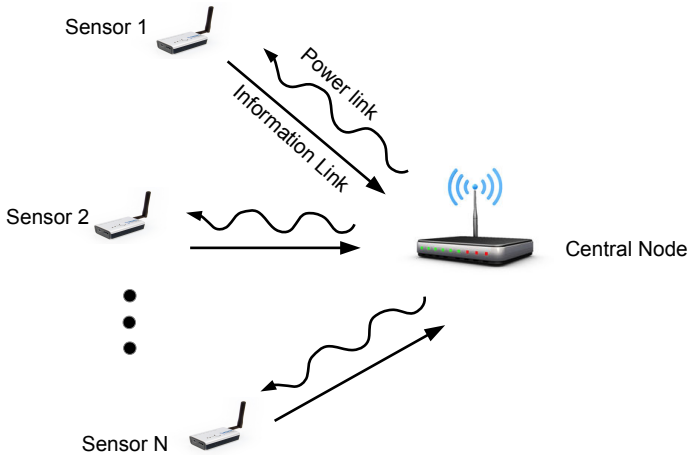

Figure 4.1: System model for Chapter 4.

We consider a wireless connected system shown in Fig. 4.1 with one central node and N sensor nodes. The central node is a power station that transfers RF power to the sensor nodes. Each sensor node has a battery of capacity $b_{\max}$, which can be recharged by the RF power from the central node. Each sensor transmits information signal to the central node when its battery is not depleted. Hence, the central node acts as both the power charger and information receiver, while each sensor node is a power receiver and information transmitter.

We assume that time is divided into time frames, and each frame has T time slots. The wireless channel between the central node and any sensor i is modeled as

a finite-state Markov channel (FSMC) [94] for both information and power transfer. Rather than modeling the channel gain as a continuous random variable, the FSMC model partitions the channel gain into a finite number of intervals with thresholds $\rho_i\gamma_0 < \rho_i\gamma_1 < \cdots < \rho_i\gamma_K$, where ρ_i is the path loss factor between sensor i and the central node. The channel gain, with certain distribution, is in state k if it falls in the interval $[\rho_i\gamma_{k-1}, \rho_i\gamma_k)$. Hence, the channel state h_i^t of sensor i in time slot t, is a discrete random variable that takes values in the set $\mathcal{H} = \{1, 2, \cdots, K\}$. Using pilot signal, it is not hard to find out which interval the channel gain falls in, thus we assume that at the beginning of time slot t each sensor i knows its current channel state h_i^t. Note that this work can be extended to the case when the channel state is not perfectly known. Moreover, the statistical information of the channel state, i.e., the channel transition probability $P(h_i^{t+1}|h_i^t)$ from time slot t to $t+1$ is known. Each sensor only has its own channel state information (CSI) but not the CSI of other sensors.

The sensors transmit information in different frequency bands to avoid signal interference. The energy stored in each sensor battery is measured by discrete battery levels $\{0, \delta, 2\delta, \cdots, b_{\max}\delta\}$, where δ is the amount of energy increment per level and $b_{\max}\delta$ is the capacity of the sensor battery. Thus, we denote the battery state in slot t as $b_i^t \in \mathcal{B}$, $\mathcal{B} = \{0, 1, \cdots, b_{\max}\}$, when its battery level is $b_i^t\delta$. Each sensor can utilize $e_i^t\delta$ energy from the battery for data transmission, where $e_i^t \in \{0, 1, \cdots, b_i^t\}$. Both b_i^t and e_i^t are known only to sensor i at time t. The average transmit power of sensor i in slot t is $e_i^t\delta/\tau$, where the duration of each time slot is τ. Suppose each sensor has infinite data backlog. Hence, the average transmission rate in channel state h_i^t is

$$r(e_i^t, h_i^t) = \mathbb{E}_\gamma[B_i \log_2\big(1 + \frac{\rho_i\gamma e_i^t\delta}{B_i N_0 \tau}\big)|h_i^t] \quad (4.1)$$

$$= \int_{\gamma_{k-1}}^{\gamma_k} B_i \log_2\big(1 + \frac{\rho_i\gamma e_i^t\delta}{B_i N_0 \tau}\big) f_k(\gamma)d\gamma, \quad \text{if } h_i^t = k, k = 1, \cdots, K \quad (4.2)$$

where γ is the channel gain coefficient, B_i is the bandwidth of sensor i, N_0 is the noise power spectral density, and $f_k(\gamma)$ is the conditional probability density function of γ

given $h_i^t = k$.

On the other hand, we assume that each sensor is charged by a RF power signal with a unique frequency, and hence the central node needs to allocate its power to different sensors. Let the total power of the central node be $p_{\max}\Delta$, and the power allocated to sensor i be $p_i\Delta$, where $p_i \in \{0, 1, 2, \cdots p_{\max}\}$ and $\sum_{i=1}^{N} p_i \leq p_{\max}$. The amount of energy delivered to sensor i is modeled as $(\tau p_i \Delta \rho_i^2 d_i^t)\delta$, where d_i^t is a random power transfer efficiency coefficient. We assume that in each channel state k there are L possible transfer efficiency coefficients, $D_{k,1} < \cdots < D_{k,L}$, with probability $q_{k,1}, \cdots, q_{k,L}$ respectively. To enforce valid battery energy transition, $\{D_{k,l}\}$ are quantized such that $\tau\Delta\rho_i^2 D_{k,l}$ is an integer for any i, k, l. The power transfer efficiency coefficient determines the range of the energy transfer gain for each channel state, and the amount of energy received at each sensor depends on its channel state. We require that for $k' > k$, $D_{k,L} \leq D_{k',1}$ because the power transfer efficiency monotonically increases as the channel gain increases [88]. Denote $\mathcal{D}_k = \{D_{k,1}, \cdots, D_{k,L}\}$. To simplify the expression, let $w_i = \tau\Delta\rho_i^2$. Thus, the transition of the battery states can be expressed as

$$b_i^{t+1} = \min\{b_i^t - e_i^t + p_i w_i d_i^t, b_{\max}\}. \tag{4.3}$$

The evolution of the system state over time is illustrated in Fig. 4.2.

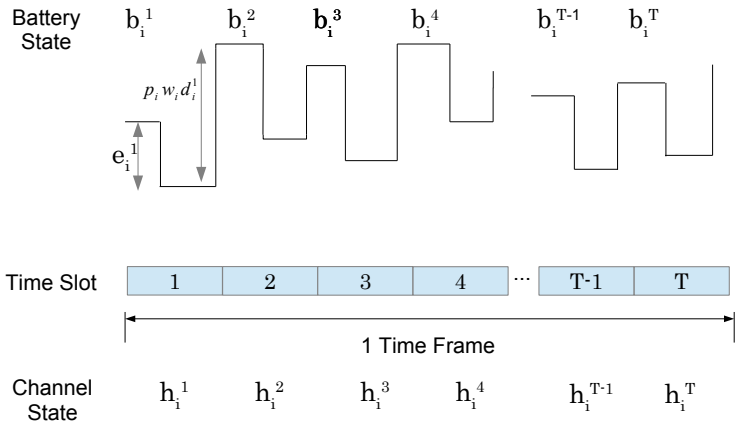

Figure 4.2: System state evolution over time.

It is clear that large e_i^t results in higher data rate, but it also leaves less battery energy for future transmission. Aggressive usage of battery causes the system to heavily rely on the energy transfered from the central node in each time slot; while conservative usage leads to low data rate and energy dissipation when the battery is saturated and part of the incoming energy is wasted. On the other hand, the power allocation at the central node controls the battery charging rate. An efficient allocation strategy is important to achieve higher system data throughput and to minimize the energy waste.

4.3 Problem Formulation

In this chapter, we consider the problem of the joint design of the power allocation at the central node and transmission energy utilization policy at the sensors in one time frame, with the objective of maximizing the expected total data throughput. At the beginning of the time frame, the central node chooses the power allocation $\{p_i, i = 1, \cdots, N\}$ for the entire time frame, and computes an energy utilization policy for sensor i which determines the amount of energy e_i^t for data transmission in slot t given the system state (h_i^t, b_i^t). Therefore, the whole problem is decomposed into two subproblems: 1) computing the energy utilization policy for sensors given the power allocation $\{p_i, i = 1, \cdots, N\}$, and 2) computing the power allocation by the central node.

4.3.1 Energy Utilization Planning Subproblem

We notice that the components of the energy utilization policy of each sensor, i.e., the state, state transition, action and reward which will be elaborated in this subsection, are independent from those of the other sensors. Hence, the energy utilization planning subproblem for the entire system can be further broken down to N independent ones where each corresponds to one sensor. Thus, in this subsection we consider the

energy utilization planning subproblem for any sensor, and we drop the subscript index i for simplicity. For each sensor, the energy utilization planning subproblem aims to optimize its own battery usage policy for signal transmission given the charging rate p. The subproblem is formulated as a finite-horizon Markov decision process (MDP) problem. The MDP consists of the following elements: system state, action set, reward function and state transitions, which are described as follows.

1) System State: The state of the sensor at time slot t consists of the battery state $b^t \in \mathcal{B}$ and the channel state $h^t \in \mathcal{H}$, i.e., $\boldsymbol{s}^t = (b^t, h^t)$. The sensor also observes the allocated charging power p, which is fixed in the current time frame.

2) Action Set: In time slot t the sensor utilizes $e^t\delta$ amount of energy for data transmission, where the action

$$e^t \in \mathcal{A}(b^t) = \{0, 1, \cdots, b^t\}. \tag{4.4}$$

3) State Transition: The transition of the sensor state $\boldsymbol{s}$ involves the transitions of the channel state and the battery state. The channel state transition probability is $P(h^{t+1}|h^t)$. On the other hand, the battery state transition is given in (4.3). Since d^t in (4.3) is random, the transition probability of the battery state is

$$P(b^{t+1}|b^t, h^t, e^t) = \sum_{d^t \in \mathcal{D}_{h^t}} P(b^{t+1}|b^t, d^t, e^t) P(d^t|h^t) \tag{4.5}$$

where

$$P(d^t = D_{k,l}|h^t = k) = q_{k,l} \tag{4.6}$$

as explained in the energy arrival model, and

$$P(b^{t+1}|b^t, d^t, e^t) = \begin{cases} 1, & \text{if (4.3) holds,} \\ 0, & \text{otherwise.} \end{cases} \tag{4.7}$$

Note that the battery transition is also affected by the channel transition. For example, the energy harvested in time slot $(t+1)$ depends on both the random energy arrival and the channel transition, i.e., $P(d^{t+1}|h^t) = P(d^{t+1}|h^{t+1})P(h^{t+1}|h^t)$. This is important for the optimization of the energy utilization policy.

4) Reward Function: At time slot t, the immediate reward of the sensor is the data rate in the current time slot $r(e^t, h^t)$ in (4.2) given the channel state h^t and action e^t.

An energy utilization policy is a sequence of decisions $\boldsymbol{\pi} = \{\pi^1, \pi^2, \cdots, \pi^T\}$, where π^t is a mapping from a state to an action at time slot t. The value of a policy $\boldsymbol{\pi}$ for the given p and initial state $\boldsymbol{s}^1$ is defined as

$$V_{\boldsymbol{\pi}}(\boldsymbol{s}^1, p) = \mathbb{E}\big[\sum_{t=1}^{T} r(h^t, e^t)|\boldsymbol{s}^1\big], \tag{4.8}$$

which is the expected total data throughput in one time frame. The energy utilization problem is then to maximize the policy value, i.e.,

$$\textbf{P4.1:} \quad \max_{\boldsymbol{\pi}} \quad V_{\boldsymbol{\pi}}(\boldsymbol{s}^1, p). \tag{4.9}$$

A classic approach to solving the finite-horizon MDP problem is the value iteration (backward induction) algorithm [95]. Define the value function at the t-th time slot as

$$V^t(\boldsymbol{s}^t, p) = \max_{\pi^t, \pi^{t+1}, \cdots, \pi^T} \mathbb{E}\big[\sum_{n=t}^{T} r(h^n, e^n)|\boldsymbol{s}^t\big], \tag{4.10}$$

the value function for the previous time slot can then be written as

$$V^{t-1}(\boldsymbol{s}^{t-1}, p) = \max_{e^{t-1} \in \mathcal{A}(b^{t-1})} [r(h^{t-1}, e^{t-1}) + \mathbb{E}[V^t(\boldsymbol{s}^t, p)|\boldsymbol{s}^{t-1}]], \tag{4.11}$$

and if $(e^{t-1})^*$ minimizes $V^{t-1}(\boldsymbol{s}^{t-1}, p)$, the action $(e^{t-1})^*$ is optimal for $\boldsymbol{s}^{t-1}$ [96, Proposition 1.3.1]. As a special case, the value function of the last time slot is

$$V^T(\boldsymbol{s}^T, p) = \max_{e^T \in \mathcal{A}(b^T)} \big[r(h^T, e^T)\big]. \tag{4.12}$$

Hence, the MDP problem of finding the optimal energy utilization policy can be solved by the value iteration algorithm as shown in Alg. 4.1. The algorithm starts from the last time slot of a time frame. For any battery state $b^T \in \mathcal{B}$ and channel state $h^T \in \mathcal{H}$, the value function and optimal policy π^T are calculated by solving the problem in (4.12). Once we find the optimal policy in the last step, we can calculate

Algorithm 4.1 - Value iteration algorithm for solving P4.1 in (4.9)

1: Input: initial channel state h^1, battery state b^1, allocated charging power p;
for $t = T$ to 1
for $b^t \in \mathcal{B}$, $t \neq 1$
for $h^t \in \mathcal{H}$, $t \neq 1$
2: Calculate the value function $V^t(\boldsymbol{s}^t, p)$ using (4.11) or (4.12);
3: Find the optimal energy utilization policy which maximizes $V^t(\boldsymbol{s}^t, p)$ in (4.11) or (4.12);
end
end
end

the value function and optimal policy π^{T-1} by solving (4.11). Repeat this process for time slots $t = T-2, T-3, \cdots, 1$, and eventually the value $V^1(\boldsymbol{s}^1, p)$ is the solution to **P4.1**, together with the optimal policy, $\boldsymbol{\pi}^*$. The computational complexity of value iteration is $\mathcal{O}(|\mathcal{B}|^2|\mathcal{H}|^2|\mathcal{A}|) = \mathcal{O}(K^2 b_{\max}^3)$.

4.3.2 Power Allocation Subproblem

On the other hand, the central node aims to find the power allocation policy for each sensor at the beginning of the time slot, such that the total expected data throughput is maximized. Let the allocated power p_i be in the set $\mathcal{P} = \{0, \cdots, p_{\max}\}$. The total data throughput of all sensors using power allocation policy $\boldsymbol{p} = [p_1, \cdots, p_N]$ is thus

$$F(\boldsymbol{p}) = \sum_{i=1}^{N} V_i^1(\boldsymbol{s}_i^1, p_i) \tag{4.13}$$

given the initial sensor states $\{\boldsymbol{s}_1^1, \cdots, \boldsymbol{s}_N^1\}$. The formulation for the power allocation subproblem is then

$$\textbf{P4.2:} \quad \max_{\boldsymbol{p}} \quad F(\boldsymbol{p}) \tag{4.14}$$
$$\text{s.t.} \quad \sum_{i=1}^{N} p_i \leq p_{\max},$$
$$p_i \in \mathcal{P}, i = 1, \cdots, N.$$

Problem **P4.2** can be solved by exhaustive search. However, it requires to perform the value iteration algorithm for all possible power allocations $\boldsymbol{p}$, which is prohibitively complex.

In this chapter, we propose efficient algorithms for solving **P4.1** and **P4.2**. In particular, we propose an accelerated value iteration algorithm to solve the energy utilization problem that can efficiently reduce the size of the action set in every time slot without loss of optimality. For the power allocation subproblem, we propose a discrete steepest descent algorithm which guarantees to find the optimal power allocation policy with a much lower computational complexity than exhaustive search.

4.4 Optimal Energy Utilization Policy

In this section, we reduce the search space in value iteration by showing that in each state some actions in the action set are non-optimal and therefore need not be considered.

The value function at time t in (4.11) can be expanded as

$$\begin{aligned}
&V^t(b^t, h^t, p) \\
&= \max_{e^t \in \mathcal{A}(b^t)} \big[r(h^t, e^t) + \sum_{b^{t+1} \in \mathcal{B}, h^{t+1} \in \mathcal{H}} P(h^{t+1}|h^t) P(b^{t+1}|b^t, h^t, e^t) \\
&\quad \times V^{t+1}(b^{t+1}, h^{t+1}, p) \big] \\
&= \max_{e^t \in \mathcal{A}(b^t)} \big[r(h^t, e^t) + \sum_{h^{t+1} \in \mathcal{H}} P(h^{t+1}|h^t) \times \\
&\quad \sum_{d^t \in \mathcal{D}_{h^t}} P(d^t|h^t) V^{t+1}(\min\{b^t - e^t + pwd^t, b_{\max}\}, h^{t+1}, p) \big]. \qquad (4.15)
\end{aligned}$$

We now show that the value function (4.15) has the following properties.

Lemma 2. *Given the channel state h^t, $V^t(b^t, h^t, p)$ is non-decreasing in (a) the battery state b^t and (b) the charging rate p.*

Proof. See proof in Appendix 4.8.1 □

Lemma 2 shows that the value function is non-decreasing in both the battery state and charging rate. The next result shows that the value function is concave in the battery state and charging rate.

Lemma 3. *Given the channel state h^t in time slot t, $V^t(b^t, h^t, p)$ is concave in (a) the battery state b^t and (b) the power allocation p.*

Proof. See proof in Appendix 4.8.2. □

The non-decreasing and concave properties lead to an important feature of the value function, which can be used to reduce the search space in the action set.

Theorem 2. *The optimal energy utilization action is non-decreasing in b^t for given h^t and p.*

Proof. See proof in Appendix 4.8.3. □

Algorithm 4.2 - Optimal energy utilization (OEU) algorithm

Input: Initial channel state h^1, current battery state b^1,
charging power p;
for $t = T$ to 1
for $h^t \in \mathcal{H}$, $t \neq 1$
Set $e_{LB} = 0$
for $b^t \in \mathcal{B}$ in increasing order, $t \neq 1$
Calculate the value function $V^t(\boldsymbol{s}^t, p)$ using (4.16) or (4.17);
Output the energy utilization action $\pi^t(b^t) = (e^t)^*$ which maximizes $V^t(\boldsymbol{s}^t, p)$ in (4.16) or $e^T = b^T$ for $t = T$;
Set $e_{LB} = (e^t)^*$;
end
end
end

Theorem 2 reveals the fact that the optimal energy utilization action for a given battery state is lower bounded by the optimal actions of all lower battery states. Suppose we have found the optimal action $(e^t)^*$ for b^t. For any battery state $\widetilde{b^t} \geq b^t$ we can search the optimal action in the range of $\{(e^t)^*, \cdots, \widetilde{b^t}\}$ rather than $\mathcal{A}(\widetilde{b^t}) = \{0, \cdots, \widetilde{b^t}\}$ in value iteration algorithm. This fact can significantly reduce the search space and speed up the algorithm. Hence, we propose an optimal energy utilization (OEU) algorithm based on Theorem 2 in Alg. 4.2.

In the OEU algorithm, at each time slot, the action is evaluated and optimized in the increasing order of the battery state b^t. When the battery is empty, the feasible action set and optimal action are both 0. Suppose the optimal action for the state $b^t - 1$ has been found as e_{LB}. In the battery state b^t, the optimal action is in the set

$\{e_{LB}, \cdots, b^t\}$. The value function effectively becomes

$$\begin{aligned} & V^t(b^t, h^t, p) \\ = & \max_{e^t \in \{e_{LB}, \cdots, b^t\}} \big[r(h^t, e^t) + \sum_{h^{t+1} \in \mathcal{H}} P(h^{t+1}|h^t) \times \\ & \sum_{d^t \in \mathcal{D}_{h^t}} P(d^t|h^t) V^{t+1}(\min\{b^t - e^t + pwd^t, b_{\max}\}, h^{t+1}, p) \big], \end{aligned} \tag{4.16}$$

and for $t = T$,

$$V^T(b^T, h^T, p) = \mathbb{E}_\gamma[B \log_2 \big(1 + \frac{\rho \gamma b^T \delta}{B N_0 \tau}\big) | h^T] \tag{4.17}$$

which has optimal action $e^T = b^T$. Step 2 initializes the lower bound of the energy utilization for each h^t. Step 3 and Step 4 optimize the value function and action for the current b^t, and Step 5 passes the current optimal action and sets as the lower bound of the energy utilization for the next value of b^t.

Same as the traditional value iteration algorithm, the OEU algorithm guarantees to find the optimal policy for given charging rate p, but it is much more efficient. The computational complexity of the OEU algorithm is upper bounded by the value iteration algorithm. That is, the OEU algorithm can achieve the same computational complexity only in the worst case scenario. On average, however, the running time of the OEU algorithm is significantly lower than that of the value iteration algorithm since the size of the search space is reduced. We illustrate the improvement of the OEU algorithm using a simple example. Suppose $b_{\max} = 9$, we want to find the policy for a given h^t at time slot t. The search space and the optimal actions are shown in Fig. 4.3. It is seen that the size of the search space is significantly reduced from 55 to 28 in this example, and 27 actions are eliminated.

4.5 Optimal Power Allocation Algorithm

In this section, we show that the optimal total throughput $F(\boldsymbol{p})$ in (4.13) is a discrete concave function which will be defined in this section, then we propose a dis-

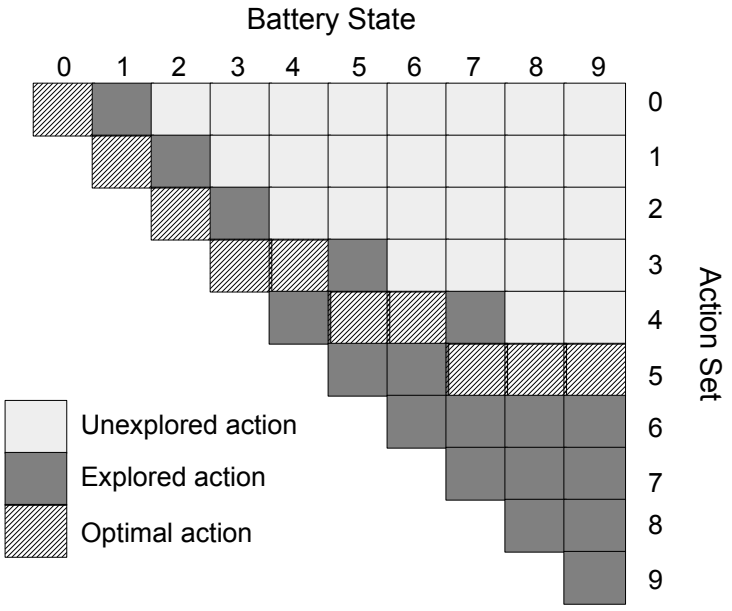

Figure 4.3: Search space of Alg. 4.2.

crete steepest-ascent algorithm to optimally solve the power allocation subproblem in (4.14).

We first introduce the concept of discrete concave functions. For a vector $\boldsymbol{x}$, define the positive support of $\boldsymbol{x}$ as $\text{supp}^+(\boldsymbol{x}) = \{u|\boldsymbol{x}[u] > 0\}$, and similarly the negative support is $\text{supp}^-(\boldsymbol{x}) = \{u|\boldsymbol{x}[u] < 0\}$. Define the basis vector as $\boldsymbol{z}_i = [0, \cdots, 0, 1, 0, \cdots, 0]$ where the non-zero element is at the i-th entry. Assuming the vector $\boldsymbol{p} \in \mathbb{Z}^N$, a function $F(\boldsymbol{p})$ is called M-concave if it satisfies the following M-concavity exchange (M-EXC) property [97].

Definition 1. *(M-EXC) For any $\boldsymbol{p}, \boldsymbol{p}' \in domF$ and $u \in supp^+(\boldsymbol{p} - \boldsymbol{p}')$, there exists $v \in supp^-(\boldsymbol{p} - \boldsymbol{p}')$ such that*

$$F(\boldsymbol{p}) + F(\boldsymbol{p}') \leq F(\boldsymbol{p} - \boldsymbol{z}_u + \boldsymbol{z}_v) + F(\boldsymbol{p}' + \boldsymbol{z}_u - \boldsymbol{z}_v). \tag{4.18}$$

We use a two-dimensional example to illustrate the M-EXC property in Fig. 4.4. Intuitively, for a discrete concave function $F(\boldsymbol{p})$, the sum of the function values evaluated at two points, $\boldsymbol{p}_1$ and $\boldsymbol{p}_2$, does not decrease if the two points move towards

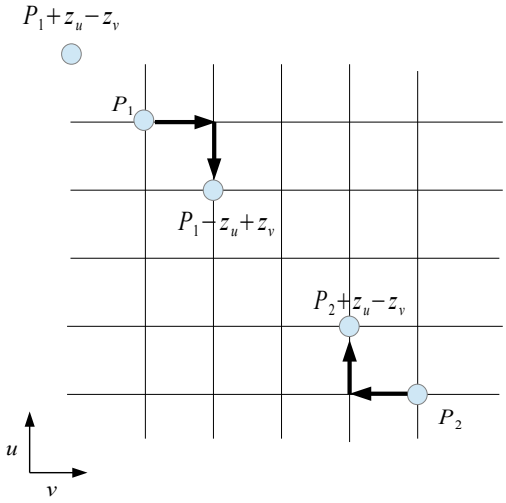

Figure 4.4: Exchange property of M-concavity.

each other. The concept is similar to the standard concave function defined in the continuous domain, but is stronger due to the discreteness of the function domain. An important property of the M-concave function is that local optimality is necessary and sufficient for global optimality [98], i.e., for the M-concave function $F(\boldsymbol{p})$, $\boldsymbol{p}^*$ is a maximizer if and only if $F(\boldsymbol{p}^*) \geq F(\boldsymbol{p}^* - \boldsymbol{z}_u + \boldsymbol{z}_v)$ for all u, v. Therefore, the discrete steepest ascent algorithm can be employed to find the maximum [97]. The algorithm starts from any point $\boldsymbol{p}$ in the function domain. It then evaluates all points in the neighborhood of the current point, i.e., $F(\boldsymbol{p} + \boldsymbol{z}_u - \boldsymbol{z}_v)$ for all u, v, and moves toward the point with the largest value. For example, at point $\boldsymbol{p}_1$ in Fig. 4.4, it moves to $\boldsymbol{p}_1 - \boldsymbol{z}_u + \boldsymbol{z}_v$ if it has higher function value than $\boldsymbol{p}_1 + \boldsymbol{z}_u - \boldsymbol{z}_v$. The algorithm continues until it terminates at a point where all neighboring points have smaller or equal function values. The final point is guaranteed to be the maximizer of $F(\boldsymbol{p})$.

In what follows, we first show that $F(\boldsymbol{p})$ in (4.13) is M-concave. Then we present the discrete steepest descent algorithm to solve the power allocation problem **P4.2** in (4.14).

Theorem 3. *The function $F(\boldsymbol{p})$ in (4.13) is M-concave.*

Proof. See proof in Appendix 4.8.4. □

Algorithm 4.3 - Optimal power allocation (OPA) algorithm for central node

1: Pick a random charging policy $\boldsymbol{p} = \{p_1, \cdots, p_N\} \in \text{dom}F$,
initialize empty $\boldsymbol{V}$;
2: **For** $i, j = 1, \cdots, N, i \neq j$
If $\boldsymbol{V}[i,(p_i-1)]$,$\boldsymbol{V}[j,(p_j+1)]$,$\boldsymbol{V}[i,p_i]$, or $\boldsymbol{V}[j,p_j]$ empty
3: Evaluate the missing policies;
4: Record the policy values in the table;
End
End
If $\left(V_{i^*}^1(\boldsymbol{s}_{i^*}^1, p_{i^*}-1) + V_j^1(\boldsymbol{s}_{j^*}^1, p_{j^*}+1) - V_{i^*}^1(\boldsymbol{s}_{i^*}^1, p_i) - V_{j^*}^1(\boldsymbol{s}_{j^*}^1, p_{j^*}) \leq 0\right)$
Stop;
Else
5: Update $\boldsymbol{p}$ where $p_{i^*} = p_{i^*} - 1, p_{j^*} = p_{j^*} + 1$;
6: Return to Step 2;
End

Now we propose the optimal power allocation (OPA) algorithm. We start from a random power allocation $\boldsymbol{p}$. In each iteration, we find the optimal search direction $\tilde{\boldsymbol{p}}$ in the neighborhood of $\boldsymbol{p}$, i.e.,

$$\tilde{\boldsymbol{p}} = \underset{\boldsymbol{p}' \in \text{ neighborhood of } \boldsymbol{p}}{\text{argmax}} F(\boldsymbol{p}') - F(\boldsymbol{p}), \tag{4.19}$$

or equivalently

$$(i^*, j^*) = \underset{i,j \in \{1,\cdots,N\}}{\text{argmax}} V_i^1(\boldsymbol{s}_i^1, p_i - 1) + V_j^1(\boldsymbol{s}_j^1, p_j + 1) - V_i^1(\boldsymbol{s}_i^1, p_i) - V_j^1(\boldsymbol{s}_j^1, p_j), \tag{4.20}$$

where $V_i^1(\boldsymbol{s}_i^1, p_i - 1)$ and $V_j^1(\boldsymbol{s}_j^1, p_j + 1)$ can be evaluated using the OEU algorithm in Alg. 4.2. If $F(\tilde{\boldsymbol{p}}) > F(\boldsymbol{p})$, then we set $\boldsymbol{p} \leftarrow \tilde{\boldsymbol{p}}$ and repeat the process. Otherwise, the current $\boldsymbol{p}$ is the optimum.

In order to avoid repetitive calculation of $V_i^1(\boldsymbol{s}_i^1, p_i)$, we use a table $\boldsymbol{V}$ to record the values of all evaluated policies.The table has N rows and $(p_{\max}+1)$ columns. Each row of $\boldsymbol{V}$ corresponds to a sensor, and each column corresponds to an input power. For example, $\boldsymbol{V}[1,2]$ corresponds to the optimal policy value of sensor 1 when the charging rate is $p_1 = 2$, i.e., $\boldsymbol{V}[1,2] = V_1^1(\boldsymbol{s}_1^1, 2)$. Once a power allocation is evaluated, the value is filled in the table. In this way we can keep track of the evaluated power allocation policies for each sensor and avoid repeated calculations. The OPA algorithm is summarized in Alg. 4.3. The number of iterations to converge is bounded by $\|\boldsymbol{p}^0 - \boldsymbol{p}^*\|_1/2 \leq p_{\max}$ by [97, Lemma 2], where $\boldsymbol{p}^0$ is the initial power allocation and $\boldsymbol{p}^*$ is the optimal solution. Note that the table is partially filled when the optimum is found. On the other hand, the exhaustive search requires to evaluate all possible power allocations for all sensors, which is equivalent to exhaustively evaluate the entire table of $\boldsymbol{V}$. Then, it needs to find the optimal power allocation from the totally $\binom{p_{\max}+N}{N}$ possible $\boldsymbol{p}$ that satisfies $\sum_i^N p_i = p_{\max}$ by the occupancy theorem [99]. Thus, it is clear that the OPA algorithm is computationally much more efficient than the exhaustive search.

In practice, the system implementation consists of a planning phase and a functioning phase for each time frame. The planning phase is at the beginning of the time frame. In this phase the central node carries out Alg. 4.3 and Alg. 4.2 to find the optimal power allocation and energy utilization scheme. Then the system goes into the functioning phase. The central node charges the sensor nodes according to the optimal power allocation plan for the entire time frame. In each time slot, each sensor acquires its channel state and battery state, and transmits data to the central node according to its energy utilization policy. The functioning phase terminates at the end of the current time frame. The process repeats for all time frames.

4.6 Simulation Results

In this section we evaluate of the performance of the proposed algorithms through simulations. We consider a system with $N = 5$ sensors. The channel between each sensor and the central node follows Rayleigh distribution, with the probability density function $f(\gamma) = \frac{1}{\bar{\gamma}} e^{-\frac{\gamma}{\bar{\gamma}}}$, where $\bar{\gamma} = 1$ is the mean. The channel is then modeled as an FSMC with 3 states, where $\gamma_1 = 0.25, \gamma_2 = 1.5, \gamma_3 = 3$, and the path loss of each sensor is $\rho_1 = 0.017, \rho_2 = 0.017, \rho_3 = 0.014, \rho_4 = 0.01, \rho_5 = 0.01$. According to the FSMC channel model [94], the transition probability of the channel states is set as

$$P = \begin{bmatrix} 0.38 & 0.62 & 0 \\ 0.245 & 0.595 & 0.16 \\ 0 & 0.54 & 0.46 \end{bmatrix},$$

where $P[a, b]$ represents that the transition probability from state a to state b. The set of power transfer efficiency coefficients is $\mathcal{D}_1 = \{1, 2\}$ with probability $q_{1,1} = 0.8$ and $q_{1,2} = 0.2$ when the channel is in state 1, $\mathcal{D}_2 = \{2, 3\}$ with $q_{2,1} = 0.5$ and $q_{2,2} = 0.5$ when channel is in state 2, and $\mathcal{D}_3 = \{3, 4\}$ with $q_{3,1} = 0.2$ and $q_{3,2} = 0.8$ when channel is in state 3. Let $w_1 = 3, w_2 = 3, w_3 = 2, w_4 = 1, w_5 = 1$. The battery increment is $\delta = 1$J, and the size of the battery is $b_{\max} = 40$. The central node has total power $p_{\max} = 10$. The bandwidth of each sensor is 100kHz. The channel has noise spectrum density $N_0 = 10^{-5}$. Each time slot has duration 1s and the policies are planned for $T = 20$ time slots.

We first evaluate the performance of the proposed algorithms in terms of the total transmission rate $F(\boldsymbol{p})$. All sensors are initially in channel state 2 and battery state 0. In this example, the exhaustive search method needs to evaluate the full $\boldsymbol{V}$ matrix of size of $(10 + 1) \times 5 = 55$. That is, the exhaustive search method has to run Alg. 4.1 or Alg. 4.2 55 times.

On the other hand, Fig. 4.5 shows the convergence of the OPA algorithm. It can be seen that it converges very fast and reaches optimum in 5 iterations. After the OPA algorithm converges, the $\boldsymbol{V}$ matrix is only partially filled as shown in Table I.

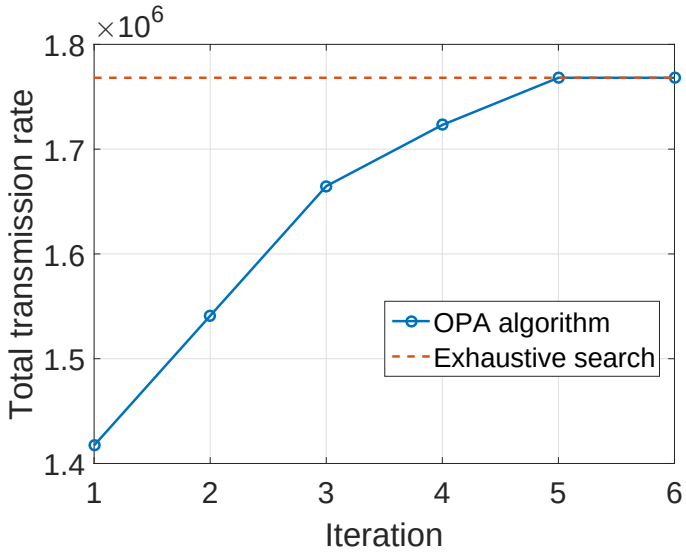

Figure 4.5: Convergence of Alg. 4.3.

Only 21 power allocations are evaluated, which is less than 40% of the exhaustive search space. To compare with the value iteration algorithm, the running time of all schemes are shown in Table II. The OEU algorithm in Alg. 4.2 speeds up the value iteration algorithm in Alg. 4.1, and it takes 43% of the time that Alg. 4.1 takes. On the other hand, the OPA algorithm in Alg. 4.3 significantly reduce the computational load, with a running time that is about 40%. Together the two algorithms can speed up the computation by a factor of 4 compared with the method based on exhaustive search and standard value iteration.

Now we evaluate the system performance in different settings. First we fix the capacity of the power source to be $p_{\max} = 10$ and vary the size of sensor batteries $b_{\max}$. All other parameters are kept the same as in Fig. 4.5. We compare the system performance with different policy baselines. For the energy utilization policy of each sensor, we compare our result with the aggressive utilization baseline (AG) where each sensor always utilize 75% of the energy in the battery in each time slot, and we also compare with the conservative utilization baseline (CON) where each sensor always utilizes 25% of the energy in the battery. On the other hand, for the power allocation

p_i / i	0	1	2	3	4	5	6	7	8	9	10
1		27.9	48.5	65.0	73.5						
2		27.9	48.5	65.0	73.5						
3		15.5	27.3	37.8	46.9	54.9					
4	0	4.6	8.6	12.2							
5	0	4.6	8.6	12.2							

Table 4.1: Value of power allocations ($\times 10^4$).

Scheme	Running time (s)
Proposed Scheme (Alg.4.2+Alg.4.3)	2.5
Alg. 4.1 + Alg. 3	5.7
Alg. 4.2 + Exhaustive search	4.2
Alg. 4.1 + Exhaustive search	10.5

Table 4.2: Running time of different methods

of the central node, we compare with the uniform power allocation baseline (UA), where the central node allocates the total power evenly over all sensors. To specifically show the performance gain of each policy, we compare the proposed scheme with the following combination of baselines: UA with the optimal energy utilization policy using Alg. 4.2 (UA-OEU), UA with AG, and UA with CON. The result is averaged over 2000 time slots, which is 100 policy planning frames.

The result is illustrated in Fig. 4.6. For all baselines, the amount of data transmitted increases as the battery size increases. The reason is when the battery size increases, the battery will be less likely to be charged to saturation, and less energy will be wasted. Hence more energy can be used for transmission, which increases the data throughput. From the figure it is clear that the proposed scheme outperforms all other baselines. By comparing the UA-OEU baseline with the UA-AG and UA-

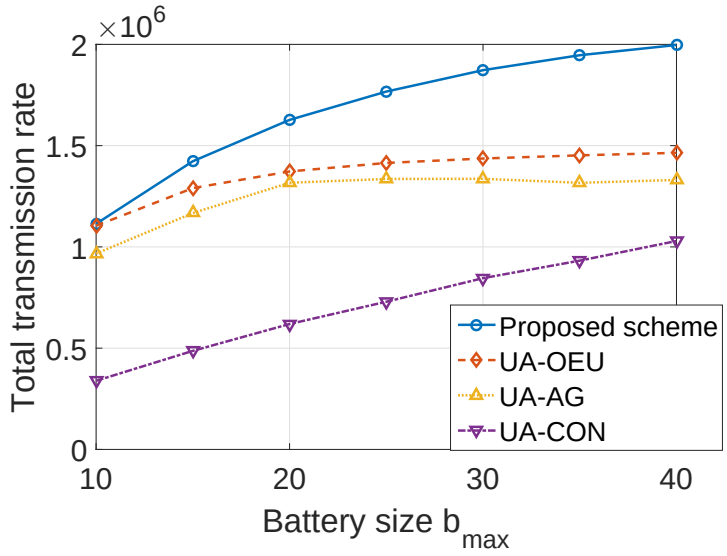

Figure 4.6: Data throughput versus the size of sensor battery.

CON baselines, it is clear that the optimal energy utilization policy for the sensors achieves higher data throughput than both the aggressive baseline and the conservative one. In this example, the aggressive baseline shows better performance than the conservative one. By comparing the proposed scheme with UA-OEU, we see that the optimal power allocation outperforms the uniform allocation policy, and interestingly the gap increases as the battery size increases. To discover the reason that magnifies the difference and understand the underlying characteristics of the system, we look into the detail of the optimal policies.

Fig. 4.7 illustrates the optimal power allocation versus the battery size. When the sensor battery size is $b_{\max} = 10$, the difference of the power allocation for each sensor is not large, and the OPA is similar to the uniform baseline. In this case the total data throughput is very close. As the sensor battery size increases, more power is allocated to sensor 1, 2 and 3, and less power is allocated to sensors 4 and 5. When $b_{\max}$ is greater than 20, the OPA stops allocating power to sensors 4 and 5, and all power is shared among the other 3 sensors. The unbalanced power allocation enables more data throughput in the large battery size settings. The reason is that

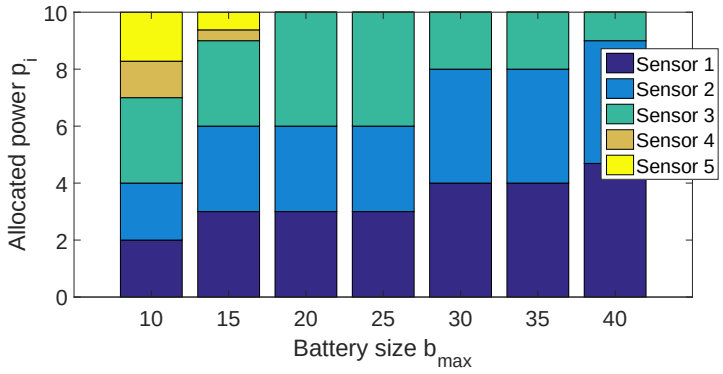

Figure 4.7: Optimal power allocation versus the battery size.

sensors 1-3 have higher channel gain than sensors 4 and 5. In this case, allocating more power to those sensors with high gains enables high energy transfer efficiency, which in turn can let them utilize more energy for data transmission. In Fig. 4.8,

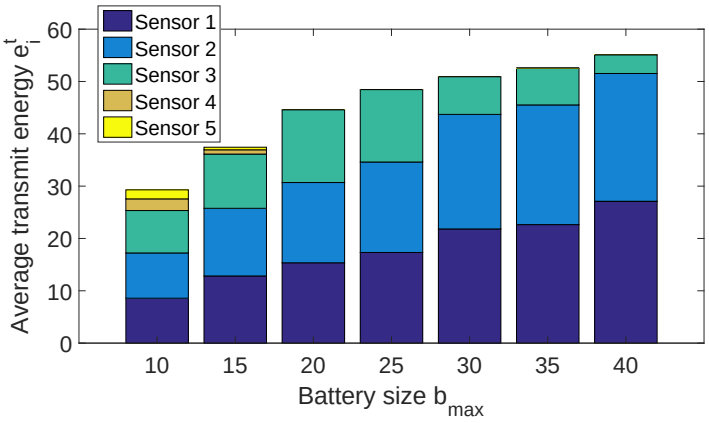

Figure 4.8: Average transmit energy of each sensor versus the battery size.

we observe that the average energy utilization per slot increases rapidly for sensors 1 and 2 as the battery size increases. Moreover, their high channel gains further improve the data throughput. Hence, high channel gain leads to better performance in both energy and information transfer, and therefore the OPA focuses power on the sensors with strong channels, so as to achieve high data throughput when the battery size is large. On the other hand, when the battery size is small the OPA distributes

power more evenly among all sensors. The reason is that the batteries can easily been charged in full due to the limited battery size, and those sensors with strong channel gain will experience high battery discharge when they are assigned with high charging power. That is, although sensors with strong channels may transmit more data with unit energy, allocating more power to them will result in increasing energy waste and limit their data transmission performance. This can be clearly illustrated by the battery discharges in Fig. 4.9. When the battery size is small, sensors 1 and 2

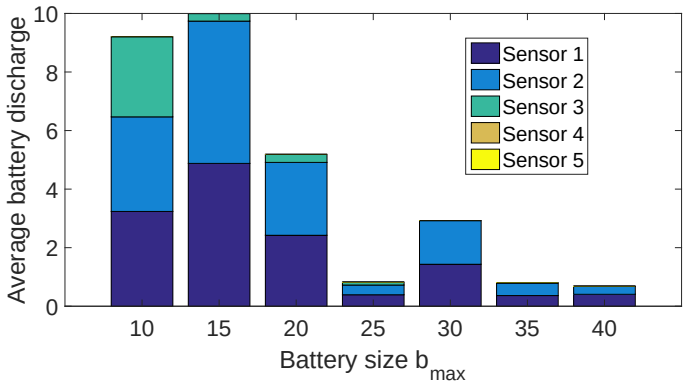

Figure 4.9: Average battery energy discharge per slot versus the battery size.

experience high battery discharges even when they are allocated with a small portion of the power resource. The discharge rate decreases as the battery size increases.

Similar result is observed if we fix the battery size at $b_{\max} = 25$ and vary the total power at the central node. As shown in Fig. 4.10, when the total power is low, it needs to be spent efficiently on sensors 1 and 2. In this case, the power allocation policy is unbalanced and these two sensors have priority to use the total power. Hence, the difference between the proposed scheme and the uniform baseline is large. As the total power increases, the OPA becomes more balanced among all sensors, and the gap becomes smaller. On the other hand, the gap between the UA-OEU and UA-CON baselines becomes greater, which illustrates that the energy utilization policy becomes more aggressive when the total power increases. This is because as the

sensors receive more energy from the central node, and aggressive utilization policy not only increases the data throughput, but also reduces the energy discharge.

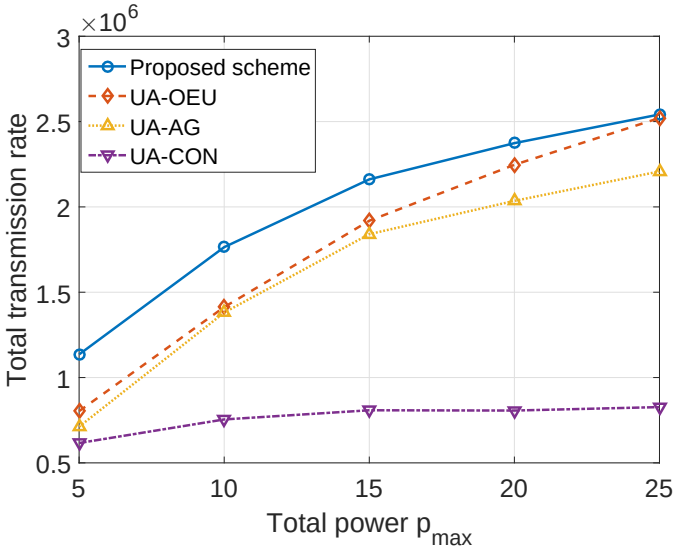

Figure 4.10: Data throughput versus total charging power.

We also investigated the performance of the time frame length T. In Fig. 4.11, we show the total number of bits transmitted in 1000 time slots with T is 20, 50, and 100 respectively. In this example, $P_{\max} = 25$ and other parameters are set as in Fig. 4.10. We can see that as T increases, the total number of bits transmitted in the same period of time increases. This is because during the transition of time frames, the optimal energy utilization action is to use all available energy at the end of the previous slot, and will leads to low battery initial states in the next time frame. This results in performance reduction. By increasing T, the number of time frame transitions will reduce in the same period of time, and thus improve the system throughput. However, the throughput gain is very small because the improvement over the transitions is very limited comparing with the overall performance. On the other hand, increasing the number of time slots in a time frame also increases the running time for Alg. 4.2 and Alg. 4.3 to search for the optimal policy, which may result in a timeout in practical implementations. Hence, T can be set based on the

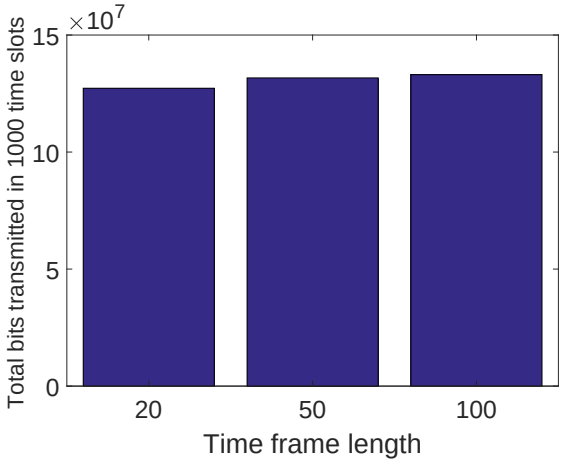

Figure 4.11: Total number of bits transmitted in 1000 time slots.

size of system and computation capability.

To summarize, increasing the battery size or the power source increases the data throughput. In the large battery size or low power supply settings the optimal power allocation has nonuniform distribution of total powers as the sensors with strong channel gains have higher priority to use power source. On the other hand, when the total power is high or battery size is low, the optimal policy tends to have balanced power allocation among all sensors. The energy utilization policy becomes aggressive as the total charging power increases.

4.7 Conclusions

In this chapter, we have considered a wireless powered IoT networks where the sensors are charged by the RF signal transmitted from a central node. We have formulated the problem of designing the sensor energy utilization policy and the problem of allocating the total charging power among the sensors, with the objective of maximizing the total data throughput. The first problem is an MDP and by showing that optimal action is non-decreasing in the battery state, we have proposed an algorithm to compute the optimal energy utilization policy with reduced search space. On the other hand, for

the power allocation problem we have shown that the total data throughput function is M-concave with respect to the power allocation, based on which a discrete steepest ascent algorithm is proposed to find the optimal power allocation.

Simulations show that the proposed algorithms are computationally efficient and they outperform simple heuristics. In particular, the proposed optimal power allocation algorithm outperforms the uniform power allocation baseline, and the optimal energy utilization algorithm outperforms the corresponding aggressive and conservative baselines.

4.8 Appendices

4.8.1 Proof of Lemma 2

The proof is by induction. First consider the case $t = T$ in (4.12), we have

$$V^T(b^T, h^T, p) = \max_{e^T \in \mathcal{A}(b^T)} \mathbb{E}_\gamma[B \log_2 \big(1 + \frac{\rho\gamma e^T \delta}{B N_0 \tau}\big) | h^T]. \tag{4.21}$$

Since the log function is monotonically increasing as e^T increases, it can be easily seen that the maximizer of V^T is $(e^T)^* = b^T$. Hence, Lemma 2 holds for b^t when $t = T$. Now we assume $V^{t+1}(b^{t+1}, h^{t+1}, p)$ is non-decreasing in b^{t+1} in time slot $t+1$. For a given h^t and p, suppose that the optimal action for b^t is $(e^t)^*$, and we have another battery state $(b^t)' > b^t$. Then $(e^t)^*$ is also in the action set $\mathcal{A}((b^t)')$. Let

$\beta^t(b,e) = \min\{b + pwd^t - e, b_{\max}\}$, we have

$$
\begin{aligned}
& V^t((b^t)', h^t, p) \\
=& \max_{e^t \in \mathcal{A}((b^t)')} \left[r(h^t, e^t) + \sum_{h^{t+1} \in \mathcal{H}, d^t \in \mathcal{D}_{h^t}} P(h^{t+1}|h^t) P(d^t|h^t) V^{t+1}(\beta^t((b^t)', e^t), h^{t+1}, p) \right] \\
\geq& r(h^t, (e^t)^*) + \sum_{h^{t+1} \in \mathcal{H}, d^t \in \mathcal{D}_{h^t}} P(h^{t+1}|h^t) P(d^t|h^t) V^{t+1}(\beta^t((b^t)', (e^t)^*), h^{t+1}, p) \qquad (4.22) \\
\geq& r(h^t, (e^t)^*) + \sum_{h^{t+1} \in \mathcal{H}, d^t \in \mathcal{D}_{h^t}} P(h^{t+1}|h^t) P(d^t|h^t) V^{t+1}(\beta^t(b^t, (e^t)^*), h^{t+1}, p) \qquad (4.23) \\
=& V^t(b^t, h^t, p). \qquad (4.24)
\end{aligned}
$$

Because $\beta^t((b^t)', (e^t)^*) \geq \beta^t(b^t, (e^t)^*)$, and V^{t+1} is assumed to be non-decreasing in b^{t+1} by the induction assumption, (4.22) is no less than (4.23). Therefore V^t is also non-decreasing in b^t at time t, which completes the proof for part (a).

For part (b) at time T, V^T is independent of p in (4.21), so it is non-decreasing in p. Now assume that $V^{t+1}(b^{t+1}, h^{t+1}, p)$ is non-decreasing in p. For given b^t and h^t, let the optimal action under the charging rate p be $(e^t)^*$, and $\tilde{\beta}^t(p,e) = \min\{b^t + pwd^t - e, b_{\max}\}$. Thus for any $p' > p$, we have

$$
\begin{aligned}
& V^t(b^t, h^t, p') \\
\geq& r(h^{t-1}, (e^t)^*) + \sum_{h^{t+1} \in \mathcal{H}, d^t \in \mathcal{D}_{h^t}} P(h^{t+1}|h^t) P(d^t|h^t) V^{t+1}(\tilde{\beta}^t(p', (e^t)^*), h^{t+1}, p') \qquad (4.25) \\
\geq& r(h^{t-1}, (e^t)^*) + \sum_{h^{t+1} \in \mathcal{H}, d^t \in \mathcal{D}_{h^t}} P(h^{t+1}|h^t) P(d^t|h^t) V^{t+1}(\tilde{\beta}^t(p, (e^t)^*), h^{t+1}, p) \qquad (4.26) \\
=& V^t(b^t, h^{t-1}, p),
\end{aligned}
$$

where (4.26) follows from (4.25) since V^{t+1} is proved to be non-decreasing in b^{t+1} in part (a), and by the induction assumption it is non-decreasing. Hence V^t is non-decreasing in p, which completes the proof for part (b).

4.8.2 Proof of Lemma 3

We show that V^t is concave in both b^t and p by induction. From (4.21), it can be easily seen that when $t = T$,

$$V^T(b^T, h^T, p) \;=\; \mathbb{E}_\gamma[B\log_2\big(1+\frac{\rho\gamma b^T\delta}{BN_0\tau}\big)|h^T], \tag{4.27}$$

which is concave in b^T. Since it is independent of p, V^T is concave in (b^T, p). Now assume that in time slot $(t+1)$, V^{t+1} is concave in (b^{t+1}, p) for given h^{t+1}, we need to show that V^t is concave in (b^t, p). That is, for any (b^t, p) and $((b^t)', p')$, and $\lambda \in [0,1]$ such that $(b_\lambda, c_\lambda) = \lambda(b^t, p) + (1-\lambda)((b^t)', p') \in \mathcal{B}\times\mathcal{P}$, we need to show that $V^t(b_\lambda, h^t, p_\lambda) \geq \lambda V^t(b^t, h^t, p) + (1-\lambda)V^t((b^t)', h^t, p')$, where V^t is given in (4.15). Let the maximizer of $V^t(b^t, h^t, p)$ and $V^t((b^t)', h^t, p')$ be e_1 and e_2 respectively. From (4.2) r is a concave function of e^t. Thus for the first term of V^t in (4.15), we have

$$\lambda r(e_1, h^t) + (1-\lambda)r(e_2, h^t) \leq r(e_\lambda, h^t), \tag{4.28}$$

where $e_\lambda = \lambda e_1 + (1-\lambda)e_2$. Note that since $e_1 \leq b^t$ and $e_2 \leq (b^t)'$, $e_\lambda \leq b_\lambda$ then $e_\lambda \in \mathcal{A}(b_\lambda)$. Next, let $\beta^t(b,p) = \min\{b + pwd^t, b_{\max}\}$, and we check the concavity of the function $V^{t+1}(\beta^t(b^t - e^t, p), h^{t+1}, p)$. Firstly, V^{t+1} is concave in (b^{t+1}, p) by the induction assumption of the induction. Secondly, V^{t+1} is non-decreasing in each variable b^{t+1} and p by Lemma 2. Also, $\beta^t(b^t - e^t, p)$ is the minimum of an affine function of $(b^t - e^t, p)$ and a constant, hence $\beta^t(b^t - e^t, p)$ is a concave function of $(b^t - e^t, p)$. Therefore, by the vector composition rule [100, pp. 86], $V^{t+1}(\beta^t(b^t - e^t, p), h^t, p)$ is concave in $(b^t - e^t, p)$, i.e.,

$$\begin{aligned}\lambda V^{t+1}(\beta^t(b^t - e_1, p), h^{t+1}, p) + (1-\lambda)V^{t+1}(\beta^t((b^t)' - e_2, p'), h^{t+1}, p') \\ \leq V^{t+1}(\beta^t(b_\lambda - e_\lambda, p_\lambda), h^{t+1}, p_\lambda).\end{aligned} \tag{4.29}$$

By (4.28) and (4.29), we have

$$\begin{aligned}
&V^t(b_\lambda, h^t, p_\lambda) \\
=&\max_{e^t \in \mathcal{A}(b_\lambda)} \left[r(h^t, e^t) + \sum_{h^{t+1} \in \mathcal{H}, d^t \in \mathcal{D}_{h^t}} P(h^{t+1}|h^t) P(d^t|h^t) V^{t+1}(\beta^t(b_\lambda - e^t, p_\lambda), h^{t+1}, p_\lambda) \right] \\
\geq& r(h^t, e_\lambda) + \sum_{h^{t+1} \in \mathcal{H}, d^t \in \mathcal{D}_{h^t}} P(h^{t+1}|h^t) P(d^t|h^t) V^{t+1}(\beta^t(b_\lambda - e_\lambda, p_\lambda), h^{t+1}, p_\lambda) \\
\geq& \lambda r(h^t, e_1) + (1-\lambda) r(h^t, e_2) + \sum_{h^{t+1} \in \mathcal{H}, d^t \in \mathcal{D}_{h^t}} P(h^{t+1}|h^t) P(d^t|h^t) \\
&\times \left[\lambda V^{t+1}(\beta^t(b^t - e_1, p), h^{t+1}, p) + (1-\lambda) V^{t+1}(\beta^t((b^t)' - e_2, p'), h^{t+1}, p') \right] \\
=& \lambda V^t(b^t, h^t, p) + (1-\lambda) V^t((b^t)', h^t, p'). \qquad (4.30)
\end{aligned}$$

Hence, the concavity of the value function holds for time slot t, and this completes the proof that V^t is concave in (b^t, p). To show that $V^t(b^t, h^t, p)$ is concave in each variable of b^t and p, simply fixing one variable of (b^t, p) and the concavity still holds because concavity can be restricted to any line that intersects the domain. This completes the proof for Lemma 3.

4.8.3 Proof of Theorem 2

For given h^t and p, denote $(e^t)^*$ as the optimal action. When $t = T$ it can be easily seen that for any $\widetilde{b^T} > b^T$, the optimal action $(\widetilde{e^T})^* > (e^T)^*$. For $t < T$, the value of an action e^t is

$$\begin{aligned}
W_{e^t}(b^t, h^t, p) =& r(h^t, e^t) + \sum_{h^{t+1} \in \mathcal{H}, d^t \in \mathcal{D}_{h^t}} P(h^{t+1}|h^t) P(d^t|h^t) \\
&\times V^{t+1}(\beta^t(b^t, e^t), h^{t+1}, p), \qquad (4.31)
\end{aligned}$$

where $\beta^t(b,e) = \min\{b + pwd^t - e, b_{\max}\}$. For b^t, the difference of the values of the action $(e^t)^*$ and any non-optimal action $e^t < (e^t)^*$ is

$$W_{(e^t)^*}(b^t,h^t,p) - W_{e^t}(b^t,h^t,p) = \sum_{h^{t+1}\in\mathcal{H},d^t\in\mathcal{D}_{h^t}} P(h^{t+1}|h^t)P(d^t|h^t)$$
$$\times [V^{t+1}(\beta^t(b^t,(e^t)^*),h^{t+1},p) - V^{t+1}(\beta^t(b^t,e^t),h^{t+1},p)]. \tag{4.32}$$

Similarly, consider a larger battery state $\widetilde{b^t} > b^t$. The optimal action $(e^t)^*$ of b^t is also in the action set of $\widetilde{b^t}$, hence

$$W_{(e^t)^*}(\widetilde{b^t},h^t,p) - W_{e^t}(\widetilde{b^t},h^t,p) = \sum_{h^{t+1}\in\mathcal{H},d^t\in\mathcal{D}_{h^t}} P(h^{t+1}|h^t)P(d^t|h^t)$$
$$\times [V^{t+1}(\beta^t(\widetilde{b^t},(e^t)^*),h^{t+1},p) - V^{t+1}(\beta^t(\widetilde{b^t},e^t),h^{t+1},p)]. \tag{4.33}$$

By Lemma 2(a), Lemma 3(a) and applying the vector composition rule of concavity, $V^{t+1}(\beta^t(b,e),h^t,c)$ is concave in (b,e). Hence, let $\lambda = ((e^t)^* - e)/(\widetilde{b^t} - b - e^t + (e^t)^*)$,

$$V^{t+1}(\beta^t(\widetilde{b^t},(e^t)^*),h^{t+1},p) \geq \lambda V^{t+1}(\beta^t(\widetilde{b^t},e^t),h^{t+1},p)$$
$$+ (1-\lambda)V^{t+1}(\beta^t(b^t,(e^t)^*),h^{t+1},p), \tag{4.34}$$
$$V^{t+1}(\beta^t(b^t,e^t),h^{t+1},p) \geq (1-\lambda)V^{t+1}(\beta^t(\widetilde{b^t},e^t),h^{t+1},p)$$
$$+ \lambda V^{t+1}(\beta^t(b^t,(e^t)^*),h^{t+1},p). \tag{4.35}$$

Adding both sides of (4.34)-(4.35), we have

$$V^{t+1}(\beta^t(\widetilde{b^t},(e^t)^*),h^{t+1},p) + V^{t+1}(\beta^t(b^t,e^t),h^{t+1},p)$$
$$\geq V^{t+1}(\beta^t(\widetilde{b^t},e^t),h^{t+1},p) + V^{t+1}(\beta^t(b^t,(e^t)^*),h^{t+1},p), \tag{4.36}$$

and thus

$$V^{t+1}(\beta^t(\widetilde{b^t},(e^t)^*),h^{t+1},p) - V^{t+1}(\beta^t(\widetilde{b^t},e^t),h^{t+1},p)$$
$$\geq V^{t+1}(\beta^t(b^t,(e^t)^*),h^{t+1},p) - V^{t+1}(\beta^t(b^t,e^t),h^{t+1},p). \tag{4.37}$$

Substituting (4.37) in (4.32) and (4.33), we have

$$W_{e^t}(\widetilde{b^t},h^t,p) - W_{(e^t)^*}(\widetilde{b^t},h^t,p) \leq W_{e^t}(b^t,h^t,p) - W_{(e^t)^*}(b^t,h^t,p) \leq 0. \tag{4.38}$$

Therefore, the optimal action of $\widetilde{b^t}$ is lower bounded by $(e^t)^*$, which means that the optimal action is non-decreasing in b^t. This completes the proof.

4.8.4 Proof of Theorem 3

The domain of $F(\boldsymbol{p})$ in problem **P4.2** is $\sum_{i=1}^{N} p_i \leq p_{\max}$, with $p_i \in \mathcal{P}$. It is easy to see that to achieve optimality we should have $\sum_{i=1}^{N} p_i = p_{\max}$, because by Lemma 2(b) $V_i^1(\boldsymbol{s}_i^1, p_i)$ is non-decreasing in p_i. Therefore, the effective domain guarantees that for any $\boldsymbol{p}$ and $\boldsymbol{p}'$, the sets $\text{supp}^+(\boldsymbol{p}-\boldsymbol{p}')$ and $\text{supp}^-(\boldsymbol{p}-\boldsymbol{p}')$ are non-empty, which is a necessary condition for the M-EXC property.

To show that $F(\boldsymbol{p})$ is M-concave, let $i \in \text{supp}^+(\boldsymbol{p}-\boldsymbol{p}')$ and $j \in \text{supp}^-(\boldsymbol{p}-\boldsymbol{p}')$. For given $\boldsymbol{s}_i^1$,

$$\begin{aligned}
&F(\boldsymbol{p}-\boldsymbol{z}_i+\boldsymbol{z}_j)+F(\boldsymbol{p}'+\boldsymbol{z}_i-\boldsymbol{z}_j)-F(\boldsymbol{p})+F(\boldsymbol{p}') \\
=&V_i(\boldsymbol{s}_i^1, p_i-1)+V_j(\boldsymbol{s}_j^1, p_j+1)+V_i(\boldsymbol{s}_i^1, p_i'+1)+ \\
&V_j(\boldsymbol{s}_j^1, p_j'-1)-V_i(\boldsymbol{s}_i^1, p_i)-V_j(\boldsymbol{s}_j^1, p_j)-V_i(\boldsymbol{s}_i^1, p_i')-V_j(\boldsymbol{s}_j^1, p_j'). \qquad (4.39)
\end{aligned}$$

Since $i \in \text{supp}^+(\boldsymbol{p}-\boldsymbol{p}')$, we have $p_i > p_i'$, and hence $p_i' < p_i'+1 \leq p_i$ and $p_i' \leq p_i - 1 < p_i$. Let $\lambda = 1/(p_i - p_i')$, thus $\lambda p_i + (1-\lambda)p_i' = p_i'+1$ and $\lambda p_i' + (1-\lambda)p_i = p_i - 1$. Since $V_i(\boldsymbol{s}_i^1, p_i)$ is concave in p_i by Lemma 3(b), we have

$$V_i(\boldsymbol{s}_i^1, p_i'+1) \geq \lambda V_i(\boldsymbol{s}_i^1, p_i') + (1-\lambda)V_i(\boldsymbol{s}_i^1, p_i), \qquad (4.40)$$

$$V_i(\boldsymbol{s}_i^1, p_i-1) \geq (1-\lambda)V_i(\boldsymbol{s}_i^1, p_i') + \lambda V_i(\boldsymbol{s}_i^1, p_i). \qquad (4.41)$$

Adding both sides of (4.40)-(4.41), we have

$$V_i(\boldsymbol{s}_i^1, p_i-1)+V_i(\boldsymbol{s}_i^1, p_i'+1)-V_i(\boldsymbol{s}_i^1, p_i)-V_i(\boldsymbol{s}_i^1, p_i') \geq 0. \qquad (4.42)$$

Similarly,

$$V_j(\boldsymbol{s}_j^1, p_j+1)+V_j(\boldsymbol{s}_j^1, p_j'-1)-V_j(\boldsymbol{s}_j^1, p_j)-V_j(\boldsymbol{s}_j^1, p_j') \geq 0. \qquad (4.43)$$

Substituting (4.42) and (4.43) in (5.58), we have

$$F(\boldsymbol{p}-\boldsymbol{z}_i+\boldsymbol{z}_j)+F(\boldsymbol{p}'+\boldsymbol{z}_i-\boldsymbol{z}_j)-F(\boldsymbol{p})+F(\boldsymbol{p}') \geq 0. \qquad (4.44)$$

This completes the proof that $F(\boldsymbol{p})$ is M-concave.

Chapter 5

Time Scheduling in Wireless Powered Backscatter Communication Networks

5.1 Introduction

In this chapter we study the time scheduling problem in a wireless-powered backscatter communication network. As discussed in previous chapters, WPT and backscatter technologies have unique feasibilities. Backscatter communication enables low latency real-time communications with simple and low cost devices. However it requires an external reader to constantly provide carrier wave. Also it has fixed transmission rate and do not support simultaneous transmission. On the other hand, the harvest-then-transmit (HTT) communication with WPT and RF-energy harvesting transmitters do not have such limitations and more flexible in transmission rate. As a tradeoff, it has to harvest enough energy before active transmission, which results in a delay. As a result, integrating the backscatter technology and HTT system becomes a prominent solution to address the issues for both methods and achieve flexible and low-latency wireless network transmission, and it has been an active research area most recently.

In [101], the network throughput optimization problem is considered for the wireless-powered backscatter communication networks, where each sensor has a unique receiver destination. Similarly, the network throughput optimization problem is considered for RF-powered cognitive radio networks (CRN) and ambient backscatter communications in [16]. The tradeoff between backscatter communication and HTT in the RF-powered backscatter CRN is analyzed in [15], and the time ratio between the two transmission modes are optimized to maximize the overall transmission rate of the secondary network. The same problem is studied in the reinforcement learning setting in [20]. The user cooperation schemes are studied to improve the energy transmission efficiency in [102]. The time allocation is studied to maximize the throughput based on user location in [19]. The relay strategy is considered in [18] to improve applicability and performance, and the throughput maximization problem is studied in [17] where the backscatter transmitters act as power relays. Game theoretic approaches are studied in [103] where the best price and backscatter time optimized to optimize the profit and utility.

In this chapter, we study the time scheduling problem in RF-powered backscatter communication networks. We consider a system network with one single-antenna reader and multiple RF powered backscatter transmitters. The transmitters can operates in either backscattering mode or harvest-then-transmit (HTT) mode, and the reader acts as a power transmitter and information receiver and supports both operating modes. The objective is to decide the mode of all transmitters and minimize the total transmission time of the network. We consider the ideal transmitters where it is assumed that no power is required for non transmission-related operations in the HTT mode. We also consider practical transmitters under realistic power consumption model where power consumption such as coding, baseband processing are considered [104, 105]. Under both transmitter models we show several key properties, and show that the optimal transmission time of each transmitter can be calculated, and their optimal operating modes can be found by using a bisection based algorithm

which has significantly lower complexity than that the exhaustive search method. We then extend the result to the massive MIMO regime, and propose an algorithm to solve the corresponding problems in linear time complexity.

5.2 System Description and Problem Formulations

5.2.1 System Model

We consider a backscatter communication system with one single-antenna reader and K RF-powered single-antenna transmitters, as illustrated in Fig. 5.1. The reader transmits carrier wave which is used for both backscatter modulation and RF energy harvesting purposes. Each transmitter is equipped with a backscatter circuitry, an energy harvesting module and a battery. They can operate in either backscattering (BS) mode or harvest-then-transmit (HTT) mode. The reader also receives and decodes information from both backscatter and HTT signals.

5.2.1.1 Network Model

All transmitters have messages with size l and they are divided into two groups: a BS group $\mathcal{B}$ and a HTT group $\mathcal{H}$. One time frame denotes the entire transmission period of the network, and it is divided into two phases, the BS phase and the HTT phase. In the BS phase, the reader transmits power signal, and each BS group transmitter transmits its message via backscattering in one of the time slots individually. The reader receives and decodes the backscatter signal from the BS transmitters. The HTT group transmitters, which are selected for HTT transmission, harvest the RF energy and store to the batteries during the entire BS phase. Then in the HTT phase, these transmitters actively transmit their messages to the reader with the harvested energy in the time-division fashion. The reader does not transmit and receives signal from the HTT transmitters during this time. The network model is illustrated in Fig. 5.2.

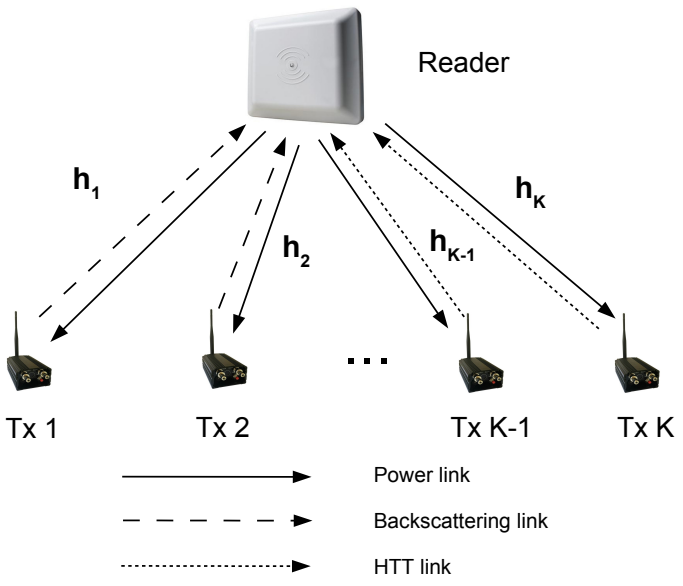

Figure 5.1: System model for Chapter 5.

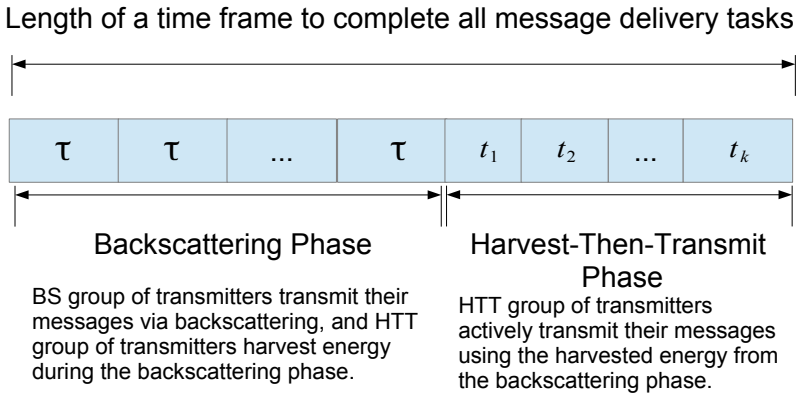

Figure 5.2: Time scheduling of the network.

5.2.1.2 Channel Model

The environment is static and the channels are assumed to remain constant within a time frame. Denote $h_k = \sqrt{\delta_k}\tilde{h}_k \in \mathbb{C}$ as the channel gain from the reader to the k-th transmitter, where δ_k is the path loss coefficient and $\tilde{h}_k$ is the fading coefficient modeled as a complex Gaussian random variable with zero mean and unit variance. Note that the channels for power downlink and information uplink of each transmitter are identical, and the fading coefficients for different transmitters $\{\tilde{h}_k\}$ are i.i.d.

5.2.1.3 Backscattering Phase

In the BS phase, the reader transmits power signal stream for both backscattering and energy harvesting. The received RF signal of the k-th transmitter is given by

$$\tilde{y}_k = \sqrt{P_C}h_k\tilde{s} + \tilde{n}_k, \tag{5.1}$$

where P_C is the transmit power of the reader, $\tilde{s} \in \mathbb{C}$ with $\mathbb{E}[\tilde{s}^2] = 1$ represents the signal symbol and $\tilde{n}_k \sim \mathcal{CN}(0, \sigma_k^2)$ denotes the complex additive while Gaussian noise (AWGN) at the k-th transmitter. Since the AWGN power is negligible compared with delivered power from the reader, the received power at the k-th transmitter is given by

$$p_k = \mathbb{E}[|\tilde{y}_k|^2] = P_C|h_k|^2. \tag{5.2}$$

To enable a transmitter operating in the BS mode, its received power must exceed the backscattering sensitivity P_B, i.e., $p_k \geq P_B$. The BS group transmitters backscatter their messages at a fixed rate r_B, and it takes $\tau = l/r_B$ amount of time to complete the task. Hence, in Fig. 5.2 each time slot has length τ, and the total time length for the BS phase is $|\mathcal{B}|\tau$, where $|\mathcal{B}|$ is the number of transmitters in the BS group. We assume that the BS group transmitters do not consume energy.

5.2.1.4 Power Consumption Models for HTT Transmitters

We assume a linear energy conversion model [41, 56, 106] at the HTT transmitters. The amount of harvested energy of an HTT transmitter k during the BS phase is given by $\epsilon_k = \eta p_k |\mathcal{B}| \tau$ where η is the energy conversion efficiency. Let t_k be its transmission time, hence the total power consumption is

$$q_k = \epsilon_k / t_k = \eta P_C |h_k|^2 |\mathcal{B}| \tau / t_k. \tag{5.3}$$

We consider two power consumption models in this chapter.

a) Ideal Power Consumption Model: Ideal transmitters can use all the harvested energy for active transmission, and there is no power consumption for other tasks such as channel coding, modulation mapping, baseband processing, RF link, etc. Let ρ_k be the transmit power, and we have $\rho_k = q_k$ in the ideal model.

b) Realistic Power Consumption Model: Based on [104, 105, 107, 108], the realistic energy consumption model for the HTT transmitters can be expressed as

$$q_k = \rho_k + a r_k + v_k, \tag{5.4}$$

where a denotes the average power consumption coefficient (PCC) of coding and modulation per bit, r_k denotes the transmission rate, and v_k denotes other fixed power consumptions. The second term ar_k accounts for the rate dependent power consumptions such as channel coding and modulation mapping, and the last term v_k accounts for other forms of fixed power consumption such as RF link, baseband processing, etc. Hence, the transmission power in the realistic energy consumption model is given by $\rho_k = q_k - a r_k - v_k$.

5.2.1.5 HTT Phase

In the HTT phase, the $\mathcal{H}$ group transmitters take turns transmitting their messages to the reader by using their harvested energy stored in the batteries, and we assume that other transmitters cannot harvest energy from the HTT transmissions due to

the low transmitting power from the HTT transmitters. The received information signal of the k-th HTT transmitter at the reader can be expressed as

$$y_k = \sqrt{\rho_k} h_k s_k + n_r, \qquad k \in \mathcal{H}, \tag{5.5}$$

where s_k is the information signal symbol and $n_r \sim \mathcal{N}(0, WN_0)$ denotes the AWGN at the reader. Its transmission rate is given by

$$r_k = W \log(1 + \frac{\rho_k |h_k|^2}{WN_0}), \qquad k \in \mathcal{H}, \tag{5.6}$$

where W is the channel bandwidth and N_0 denotes the noise power spectral density. Since the message transmission should be completed within t_k, we need the constraint $t_k r_k \geq l$.

5.2.2 Problem Formulations

The objective of this chapter is to optimize the transmitter group selection and the transmission time of each HTT transmitters, such as to minimize the total amount of time that the system takes to complete all transmission tasks.

5.2.2.1 Formulation under Ideal Power Consumption Model

In the ideal setting, the problem formulation is given by

$$\mathbf{P5.1}: \quad \min_{\mathcal{B}\subset\{1,\cdots,K\},\{t_k:\forall k\in\mathcal{H}\}} \quad |\mathcal{B}|\tau + \sum_{k\in\mathcal{H}} t_k \tag{5.7}$$

$$\text{s.t.} \quad t_k r_k \geq l, \quad k \in \mathcal{H}, \tag{5.8}$$

$$\mathcal{H} = \{1, \cdots, K\} \backslash \mathcal{B},$$

where r_k is given in (5.6).

5.2.2.2 Formulation under Realistic Power Consumption Model

Given t_k, the total power for rate dependent operations and signal power amplifying is $q_k - v_k$. Hence we require $q_k > v_k$, which from (5.4) and (5.6), is equivalent to $\rho_k > 0$

and $r_k > 0$. Therefore the condition $t_k r_k \geq l$ implies $q_k > v_k$. Let $\alpha_k \in [0,1]$ be the portion of power that is allocated for rate dependent consumptions, and $(1-\alpha_k)$ be the portion for signal power amplifying. That is,

$$\rho_k = (1-\alpha_k)(q_k - v_k), \quad ar_k = \alpha_k(q_k - v_k). \tag{5.9}$$

The problem formulation under the realistic power consumption model is

$$\begin{aligned} \mathbf{P5.2}: \quad \min_{\mathcal{B}\subset\{1,\cdots,K\},\{t_k:k\in\mathcal{H}\},\boldsymbol{\alpha}} \quad & |\mathcal{B}|\tau + \sum_{k\in\mathcal{H}} t_k & (5.10)\\ \text{s.t.} \quad & t_k r_k \geq l, \quad (5.9), \quad k \in \mathcal{H}, & (5.11)\\ & \mathcal{H} = \{1,\cdots,K\}\backslash\mathcal{B}, \end{aligned}$$

where q_k is given by (5.3) and r_k is given by (5.6).

5.3 Optimal Solution for Ideal Case

We first study the scheduling problem **P5.1** for ideal transmitters. Using (5.6), define

$$f_k(t_k) = t_k \cdot r_k = W t_k \log(1 + \frac{A_k|\mathcal{B}|}{t_k}), \tag{5.12}$$

where $A_k = \eta P_C \tau |h_k|^4/(WN_0)$. Then we have the following proposition. The proof is provided in Appendix 5.8.1.

Proposition 1. *$f_k(t_k)$ is monotonically increasing and converges to $A_k W|\mathcal{B}|$, for $t_k > 0$.*

It then follows from Prop. 1 that if $A_k W|\mathcal{B}| > l$, t_k is minimized when $f_k(t_k) = t_k \cdot r_k = l$. Hence, t_k is the unique root of $f_k(t_k) = l < A_k W|\mathcal{B}|$. The original problem **P5.1** in (5.7) is equivalent to the following combinatorial problem

$$\begin{aligned} \mathbf{P5.1'}: \quad \min_{\mathcal{B}\subset\{1,\cdots,K\}} \quad & |\mathcal{B}|\tau + \sum_{k\in\mathcal{H}} t_k \\ \text{s.t.} \quad & f_k(t_k) = l, \quad k \in \mathcal{H}, \\ & A_k W|\mathcal{B}| > l, \quad k \in \mathcal{H}, & (5.13)\\ & \mathcal{H} = \{1,\cdots,K\}\backslash\mathcal{B}. \end{aligned}$$

Assumption 1. *We assume that the received power at all transmitters is above the backscattering sensitivity such that they can operate in BS mode, i.e.,* $P_C|h_k|^2 \geq P_B$, $k = 1, \cdots, K$.

We assume that Assumption 1 holds. The reason is if there is one transmitter that does not satisfy this assumption, then it can only be assigned to the $\mathcal{H}$ group, and therefore in problem **P5.1**' the optimization is essentially over transmitters that satisfy Assumption 1. Based on this, we have the following lemma.

Lemma 4. *For the optimal solution to problem* ***P5.1****',* $t_k < \tau$ *holds for* $k \in \mathcal{H}$.

Proof. This is because if $t_k \geq \tau$ for any $k \in \mathcal{H}$, then by Assumption 1 we can switch k to group $\mathcal{B}$ to lower the objective function value. □

Lemma 4 shows that the transmission time for all HTT transmitters is upper bounded by τ. In other words, the transmission should be completed within τ, i.e., $f_k(\tau) \geq l$. This actually enforces a tighter constraint than (5.13) since $A_k W|\mathcal{B}|$ is the upper bound of $f_k(t_k)$. After some manipulations, this condition becomes $|\mathcal{B}| \geq \frac{(e^{\frac{r_B}{W}}-1)\tau}{A_k}$. Thus **P5.1**' becomes

$$\begin{aligned}
\textbf{P5.1}'': \quad \min_{\mathcal{B}\subset\{1,\cdots,K\}} \quad & |\mathcal{B}|\tau + \sum_{k\in\mathcal{H}} t_k && (5.14)\\
\text{s.t.} \quad & f_k(t_k) = l, \quad k \in \mathcal{H}, && (5.15)\\
& |\mathcal{B}| \geq \frac{(e^{\frac{r_B}{W}}-1)\tau}{A_k}, \quad k \in \mathcal{H}, && (5.16)\\
& \mathcal{H} = \{1, \cdots, K\}\backslash\mathcal{B}.
\end{aligned}$$

A straightforward approach to problem **P5.1**" is the exhaustive search over all possible subset $\mathcal{B} \subset \{1, \cdots, K\}$ which has a complexity of $\mathcal{O}(2^K)$ and is computationally prohibitive as K becomes large. For a more efficient solution, we explore the relationship between the two groups of transmitters.

Lemma 5. *Under the optimal solution to problem* ***P5.1****",* $|h_i|^2 \geq |h_j|^2$ *should hold for* $i \in \mathcal{H}, j \in \mathcal{B}$.

Proof. Suppose that there is a transmitter $i \in \mathcal{H}$ and $j \in \mathcal{B}$ such that $|h_i|^2 \leq |h_j|^2$. Then by switching i to group $\mathcal{B}$ and j to $\mathcal{H}$, the system can achieve a time difference of $t_j - t_i$. It can be seen that r_k increases monotonically with $|h_k|^2$, and so does $f_k(t_k)$, hence $f_j(t_j) = l > f_i(t_j)$. By Prop. 1, $f_k(t_k)$ increases monotonically with t_k, thus $t_j - t_i < 0$ since $f_i(t_j) < l = f_i(t_i)$. Therefore, swapping the groups of i and j always guarantees the objective value to be non-increasing and improves the system performance. This completes the proof. □

Lemma 5 essentially shows that the transmitter with higher channel gain has higher priority to be assigned to group $\mathcal{H}$. This leads to the following solution with linear complexity. We first sort the transmitters by their channel gains $|h_k|^2$ in ascending order. Then for each $1 \leq k \leq K$, we assign all first k transmitters to group $\mathcal{B}$ and the rest to group $\mathcal{H}$, and evaluate the objective function in (5.14). Moreover, for each k we just need to check the feasibility constraint in (5.16) for the $(k+1)$-th transmitter, instead of for all transmitters in $\mathcal{H} = \{k+1, \cdots, K\}$. This is because A_k is sorted as well according to $|h_k|^2$, and $|\mathcal{B}| \geq \frac{(e^{\frac{r_B}{W}}-1)\tau}{A_{k+1}} \geq \frac{(e^{\frac{r_B}{W}}-1)\tau}{A_{k'}}$ for $k' > k+1$. Finally find the optimal k with the minimum objective value which leads to the optimal group assignment. This approach has a complexity of $\mathcal{O}(K)$.

Interestingly, we can further improve the efficiency by exploring the relationship between $\mathcal{B}$ and t_k. Note that, $\mathcal{B}$ has to be non-empty, otherwise the HTT transmitters will have no energy for active transmission. Based on (5.12), define $\varrho_k(t, x) = Wt \log(1 + \frac{A_k x}{t})$. Then the constraint $f_k(t_k) = l$ becomes $\varrho_k(t_k, |\mathcal{B}|) = l$. We have the following key properties. The proof is given in Appendix 5.8.2.

Lemma 6. *Given that $\varrho_k(t, x) = l$, then we can write $t = \phi_k(x)$ where the function $\phi_k(\cdot)$ has the following properties: (a) ϕ_k is convex and decreasing in x, and (b) $\phi_k(|\mathcal{B}|) < \phi_{k'}(|\mathcal{B}|)$ for $|h_k|^2 > |h_{k'}|^2$.*

Lemma 6 leads to the following theorem which is instrumental to developing an efficient algorithm that finds the optimal group assignment. The proof is provided in Appendix 5.8.3.

Theorem 4. *Suppose transmitters are sorted according to their channel strength in ascending order, i.e.,* $|h_1|^2 < \cdots < |h_K|^2$. *Let*

$$F(k) = k\tau + \sum_{i=k+1}^{K} \phi_i(k) \tag{5.17}$$

be the objective function in (5.14) with $\mathcal{B} = \{1, \cdots, k\}$. *Then,* $F(k+1) - F(k) > F(k) - F(k-1)$ *for* $k \in \{2, \cdots, K-1\}$.

Note that in (5.17) $\phi_i(k) = t_i$ is the root of $f_i(t_i) = l$ with $|\mathcal{B}| = k$ and it can be evaluated numerically, e.g., using the gradient descent method or the bisection method since $f_i(\cdot)$ is monotonic. Intuitively Theorem 4 indicates that the difference of the objective function in (5.14) is monotonic in terms of the boundary k. Hence we can find the optimal k using the bisection method. In particular if there exists a k^* such that $F(k^*+1) - F(k^*) > 0$ and $F(k^*) - F(k^*-1) < 0$, then k^* is the unique minimizer of **P5.1**". Otherwise $F(k)$ is monotonically increasing or decreasing, which has minimizer $k^* = 1$ or $k^* = K$. Taking advantage of this result, we propose an algorithm based on the bisection method to solve the original problem **P5.1**. The algorithm is presented in Alg. 5.1.

In the initialization step, the transmitters are sorted by their channel strengths, and the left and right boundaries of the bisection procedure are initialized. In each iteration Alg. 5.1 evaluates the objective function in (5.17) at $c, c+1$, and $c-1$ where c is in the center between the left and right boundaries. But at the beginning of each iteration, the algorithm first checks if the feasibility constraint (5.16) is satisfied for $k = c$ and $|\mathcal{B}| = c-1$. If it fails, the left boundary is set to $c+1$ for the next iteration. Such k and $|\mathcal{B}|$ values correspond to the feasibility constraint for $F(c-1)$, and the reason for checking the feasibility of $F(c-1)$ only is that if $F(c-1)$ is feasible $F(c)$ and $F(c+1)$ are also feasible. In steps 4-6, the left and right boundaries are updated according to Theorem 4. If both $F(c+1) - F(c)$ and $F(c) - F(c-1)$ are less than 0, the function is decreasing at c, and the optimal k is to the right of c. Hence the left boundary is updated as $c+1$. Similarly, if both terms are greater than 0, the function

Algorithm 5.1 - Optimal Algorithm for Solving P5.1 (and P5.2)

Input: transmitter channel gains ;

Initialization: Sort the transmitters by channel gains $|h_1|^2 \leq \cdots \leq |h_K|^2$;

$l = 2, r = K-1, c = \lceil \frac{l+r}{2} \rceil$

While $l \neq r$ **Do**

1: **If** $c < \frac{(e^{\frac{r_B}{W}}-1)\tau}{A_{c+1}}$ (or if (5.25) is not satisfied for $k = c$ and $|\mathcal{B}| = c-1$ for **P5.2**):

set $l = c+1, c = \lceil \frac{l+r}{2} \rceil$;

Else Do:

2: Evaluate $F(c)$ given in (5.17) (or $G(c)$ given in (5.27) for **P5.2**, changes apply to the remaining steps), $\mathcal{B} = \{1, \cdots, c\}$, $\mathcal{H} = \{c+1, \cdots, K\}$, and $\phi_i(c)$ is the root of $f_i(t_i) = l$ with $|\mathcal{B}| = c$ (or $\psi_i(c)$ as the root of $g_i(t_i) = l$ for **P5.2**);

3: Similarly, evaluate $F(c+1), F(c-1)$;

4: **If**: $F(c+1) - F(c) < 0$ and $F(c) - F(c-1) < 0$, set $l = c+1, c = \lceil \frac{l+r}{2} \rceil$;

5: **Else If**: $F(c+1) - F(c) > 0$ and $F(c) - F(c-1) > 0$, set $r = c-1, c = \lceil \frac{l+r}{2} \rceil$;

6: **Else If**: $F(c+1) - F(c) > 0$ and $F(c) - F(c-1) < 0$, **Break**;

End

Output: $\mathcal{B} = \{1, \cdots, c\}, \mathcal{H} = \{c+1, \cdots, K\}, t_k$ as the root of $f_k(t_k) = l$ (or $g_k(t_k) = l$ with α_k in (5.18) for **P5.2**).

is monotonically increasing at c, and the optimal k is on the left of c, hence the right boundary is updated as $c-1$. The algorithm terminates when $F(c+1)-F(c)>0$ and $F(c)-F(c-1)<0$ which indicates that c is optimal. On the other hand, it stops when the left and right boundaries coincide. Note that Alg. 5.1 solves problem **P5.1** optimally and has a computational complexity of $\mathcal{O}(\log_2 K)$.

5.4 Optimal Solution for Realistic Case

Next we study problem **P5.2** under the realistic power consumption model. Define $C_k=\frac{N_0}{a|h_k|^2}$ and $D_k=\frac{v_k|h_k|^2}{WN_0}$. First we have the following theorem for the optimal α_k with given t_k. The proof is given in Appendix 5.8.4.

Theorem 5. *The optimal α_k in problem **P5.2** is given by*

$$\alpha_k^*=1+\frac{t_k}{A_k|\mathcal{B}|-D_kt_k}-\frac{t_k}{C_k(A_k|\mathcal{B}|-D_kt_k)}W_0[C_k\exp\{C_k(1+\frac{A_k|\mathcal{B}|}{t_k}-D_k)\}], \quad (5.18)$$

and the corresponding optimal rate is given by

$$r_k^*=W\big(C_k(1+\frac{A_k|\mathcal{B}|}{t_k}-D_k)-W_0[C_k\exp\{C_k(1+\frac{A_k|\mathcal{B}|}{t_k}-D_k)\}]\big) \quad (5.19)$$

where $W_0(x):[-e^{-1},\infty)\to[-1,\infty)$ is the principal branch of the Lambert function which satisfies the definition $W_0(x)e^{W_0(x)}=x$.

By Theorem 5, the optimal α_k can be found analytically, and the constraint $t_kr_k\geq l$ in (5.11) can be rewritten as

$$g_k(t_k)\triangleq t_kW\big(C_k(1+\frac{A_k|\mathcal{B}|}{t_k}-D_k)-U_k(t_k)\big)\geq l,\quad k\in\mathcal{H}, \quad (5.20)$$

where

$$U_k(t_k)=W_0[C_k\exp\{C_k(1+\frac{A_k|\mathcal{B}|}{t_k}-D_k)\}]. \quad (5.21)$$

Note that $W_0(x)>0$ for $x>0$, hence $U_k(t_k)>0$. Similar to the ideal case, in the next step we show that t_k is minimized when equality is achieved in (5.20). We have the following result and the proof is given in Appendix 5.8.5.

Proposition 2. *$g_k(t_k)$ in (5.20) is concave in t_k for $t_k > 0$, and it has a unique maximizer $t_k^* > 0$ which satisfies*

$$g_k'(t_k^*) = C_k - U_k(t_k^*) + \frac{U_k(t_k^*)}{1 + U_k(t_k^*)} \frac{A_k C_k |\mathcal{B}|}{t_k^*} - C_k D_k = 0. \tag{5.22}$$

By Proposition 2, $g_k(t_k)$ monotonically increases in the interval $t_k \in (0, t_k^*)$. Hence if the problem is feasible, i.e., $g_k(t_k^*) > l$, t_k is minimized when $g_k(t_k) = l$ is achieved. On the other hand, we assume that Assumption 1 also holds for **P5.2**, hence Lemma 4 is still valid as well, which requires $t_k < \tau$. As a result, we can rewrite problem **P5.2** as

$$\begin{aligned}
\mathbf{P5.2'}: \quad \min_{\mathcal{B} \subset \{1,\cdots,K\}} \quad & |\mathcal{B}|\tau + \sum_{k \in \mathcal{H}} t_k && (5.23)\\
\text{s.t.} \quad & g_k(t_k) = l, \quad k \in \mathcal{H}, && (5.24)\\
& g_k(t_k^*) > l, t_k < t_k^*, t_k < \tau, \quad k \in \mathcal{H}, && (5.25)\\
& \mathcal{H} = \{1, \cdots, K\} \backslash \mathcal{B},
\end{aligned}$$

where q_k is given by (5.3), $g_k(t_k)$ and t_k^* are given in (5.20) and (5.22) respectively. Constraint in (5.25) ensures that the problem is feasible. Similar to problem **P5.1**' in the ideal setting, **P5.2**' is also a combinatorial problem with the size of search space $\mathcal{O}(2^K)$, and its constraint has a much more complex functional form. Fortunately, the following analysis shows that most of the results for the ideal case in Section 5.3 still hold under the realistic power consumption model, and we can adopt the bisection based Alg. 5.1 to find the optimal transmitter group assignment.

Similarly as in Section 5.3, first we show that the channel gain also determines the transmitter's transmission rate for the power consumption model. The proof is given in Appendix 5.8.6.

Lemma 7. *Under the condition $q_k > v_k$, r_k^* in (5.19) is monotonically increasing with channel gain $|h_k|^2$. Moreover, under the optimal solution of problem **P5.2'**, $|h_i|^2 \geq |h_j|^2$ should hold for $i \in \mathcal{H}, j \in \mathcal{B}$.*

Based on Lemma 7, transmitters with higher channel gains should have higher priority to be assigned to the HTT group. Hence, the linear search method is already applicable to **P5.2**' by following the similar sorting and grouping procedure as discussed in Section 5.3. Also under such grouping, the feasibility constraint in (5.25) is automatically fulfilled for all $\mathcal{H} = \{k+1, \cdots, K\}$ transmitters if the $(k+1)$-th transmitter is satisfied. This can be easily shown since $g_{k'}(t_k^*) > g_k(t_k^*) = l$ for $k' > k$. On the other hand, we can extend Lemma 6 and Theorem 4 to problem **P5.2**'. Based on (5.20), define

$$\mu_k(t, x) = tW\big(C_k(1 + \frac{A_k x}{t} - D_k) - V_k(t, x)\big), \tag{5.26}$$

where $V_k(t, x) = W_0[C_k \exp\{C_k(1 + \frac{A_k x}{t} - D_k)\}]$. Then the constraint $g_k(t_k) = l$ becomes $\kappa_k(t_k, |\mathcal{B}|) = l$. Then we have the following lemma and the proof is given in Appendix 5.8.7.

Lemma 8. *Given that $\mu_k(t, x) = l$, then t can be expressed as a continuous function of $t = \psi_k(x)$ where (a) ψ_k is convex and decreasing in x, and (b) $\psi_k(|\mathcal{B}|) < \psi_{k'}(|\mathcal{B}|)$ for $|h_k|^2 > |h_{k'}|^2$.*

Theorem 6. *Suppose transmitters are sorted according to their channel strength in ascending order, i.e., $|h_i|^2 \leq |h_j|^2$ for $i < j$. Let*

$$G(k) = k\tau + \sum_{i=k+1}^{K} \psi_i(k) \tag{5.27}$$

be the value of the objective function in (5.23) with the groups assigned as $\mathcal{B} = \{1, \cdots, k\}$ and $\mathcal{H} = \{k+1, \cdots, K\}$. Then, $G(k+1) - G(k) > G(k) - G(k-1)$ for $k \in \{2, \cdots, K-1\}$.

Proof. Applying Lemma 8 and following the proof of Theorem 4 in Appendix 5.8.3, Theorem 6 can be proved. □

Therefore, we can adopt the bisection-based Alg. 5.1 to solve the problem **P5.2**'. Simply replace all $F(\cdot)$ in Alg. 5.1 with $G(\cdot)$ in (5.27) and change the condition of

Step 1 to "If (5.25) is not satisfied for $k = c$ and $|\mathcal{B}| = c-1$". Here we also just need to check the feasibility in (5.25) for $G(c-1)$ since $\mu_{k'}(t_c, k'-1) > \mu_c(t_c, c-1)$ for $k' > c$, and $G(c)$ and $G(c+1)$ are feasible if $G(c-1)$ is feasible. The modified algorithm finds the optimal transmitter assignment and transmitter power consumption in $\mathcal{O}(\log_2 K)$ time complexity.

5.5 Extensions to Massive MIMO

5.5.1 Massive MIMO System Model and Problem Formulation for Ideal Case

In this section we study the transmission scheduling problem under the massive MIMO setting. We first consider the ideal case. Assume that the reader is equipped with $M(\gg K)$ antennas. The channel vector has the form $\boldsymbol{h}_k = \sqrt{\delta_k}\tilde{\boldsymbol{h}}_k \in \mathbb{C}^M$, and $\tilde{\boldsymbol{h}}_k = [h_{k,1}, \cdots, h_{k,M}]$ is the channel vector between the k-th transmitter and the reader containing i.i.d. complex Gaussian fading coefficients with zero mean and unit variance.

We employ the low-complexity matched-filtering (MF) beamformer for both downlink power transfer and uplink information receiving, since it is shown to be an asymptotically optimal beamformer for both tasks in massive MIMO systems [56, 57, 109]. The MF beamformer of the k-th transmitter is given by $\boldsymbol{w}_k = \tilde{\boldsymbol{h}}_k/\|\tilde{\boldsymbol{h}}_k\|$. The reader has transmit power P/M where P is constant, and it allocates β_k portion of power for each beamformer, where $\sum_{k=1}^K \beta_k = 1$. In the massive MIMO regime, it is known that the channels are asymptotically orthogonal, i.e., $\tilde{\boldsymbol{h}}_k^H\tilde{\boldsymbol{h}}_k/M \to 1$ and $\tilde{\boldsymbol{h}}_i^H\tilde{\boldsymbol{h}}_j/M \to 0$ $(i \neq j)$ for large M [56, 109]. Hence, the massive MIMO counterpart of the received power (5.2) is given by

$$p_k = \frac{P}{M}\beta_k(\boldsymbol{h}_k^H \sum_{i=1}^K \boldsymbol{w}_i)^2 = \frac{P}{M}\beta_k\|\boldsymbol{h}_k\|^2 = P\beta_k\delta_k, \tag{5.28}$$

and the total power consumption is

$$q_k = \eta p_k |\mathcal{B}|\tau/t_k = \eta P \beta_k \delta_k |\mathcal{B}|\tau/t_k. \tag{5.29}$$

In the BS phase, the reader should allocate sufficient power to the BS transmitters, i.e., $p_k \geq P_B$. On the other hand, taking advantage of the channel orthogonality of massive MIMO, in the HTT phase the $\mathcal{H}$ transmitters can simultaneously transmit information to the reader without interfering with each other. Redefine $A = \eta\tau PM/(WN_0)$ and given $\rho_k = q_k$ for ideal transmitters, the transmission rate function of the massive MIMO system is given by

$$r_k = W\log(1 + \frac{\rho_k \|\boldsymbol{h}_k\|^2}{WN_0}) = W\log(1 + \frac{A\delta_k^2\beta_k|\mathcal{B}|}{t_k}). \tag{5.30}$$

Due to simultaneous transmissions, the total transmission time of the HTT phase becomes $\max_{k\in\mathcal{H}} t_k$. Define

$$\tilde{f}_k(t_k, \beta_k) = t_k r_k = W t_k \log(1 + \frac{A\delta_k^2\beta_k|\mathcal{B}|}{t_k}), \tag{5.31}$$

and using the same analysis techniques as in Proposition 1, we have the following proposition.

Proposition 3. *$\tilde{f}_k(t_k, \beta_k)$ is monotonically increasing in t_k and β_k, and it converges to $AW\delta_k^2\beta_k|\mathcal{B}|$, for $t_k > 0$.*

Hence, the problem formulation for massive MIMO reader under the ideal case is:

$$\mathbf{P5.3}: \min_{\mathcal{B}\subset\{1,\cdots,K\},\{\beta_1,\cdots,\beta_K\}} \quad |\mathcal{B}|\tau + \max_{k\in\mathcal{H}} t_k \tag{5.32}$$

$$\text{s.t.} \quad \tilde{f}_k(t_k, \beta_k) = l, \quad k \in \mathcal{H}, \tag{5.33}$$

$$AW\delta_k^2\beta_k|\mathcal{B}| > l, \quad k \in \mathcal{H},$$

$$P\beta_k\delta_k \geq P_B, \qquad k \in \mathcal{B},$$

$$\sum_{i=1}^{K} \beta_i = 1, \quad \mathcal{H} = \{1, \cdots, K\}\backslash\mathcal{B}.$$

Due to the min-max formulation and the additional variables β_k, problem **P5.3** is very different from **P5.1** of the single antenna case, and the bisection based method does

not work since some properties no longer hold anymore, e.g., Theorem 4. Nevertheless, in the next subsection, we show that **P5.3** can be solved optimally with linear time complexity.

5.5.2 Optimal Solution for Ideal Case

First of all, it can be observed that the optimal power allocation for transmitter $k \in \mathcal{B}$ should be exactly $\beta_k^* = P_B/(P\delta_k)$. This is because higher β_k will reduce the power allocation and harvested energy for $\mathcal{H}$ transmitters, which leads to longer transmission time; while lower β_k will result in insufficient power for backscattering transmission. Thus, all transmitters in the $\mathcal{H}$ group will share the remaining $\beta_H = 1 - \sum_{i\in\mathcal{B}} \beta_i = 1 - \sum_{i\in\mathcal{B}} P_B/(P\delta_i)$ portion of power. In the following theorem, we show that the optimal power allocation can be found analytically for $\mathcal{H}$. The proof is given in Appendix 5.8.8.

Theorem 7. *The optimal solution to **P5.3** satisfies,*

$$t_k = t, \quad \beta_k^* = \beta_H / \big(\sum_{i\in\mathcal{H}} \frac{\delta_k^2}{\delta_i^2} \big), \quad k \in \mathcal{H}, \tag{5.34}$$

for some constant t.

Substituting (5.34) into problem **P5.3**, the constraint (5.33) becomes independent of k and **P5.3** is simplified to:

$$\begin{aligned}
\mathbf{P5.3'}: \quad \min_{\mathcal{B}\subset\{1,\cdots,K\}} \quad & |\mathcal{B}|\tau + t & (5.35)\\
\text{s.t.} \quad & Wt\log(1 + \frac{A(1-\sum_{i\in\mathcal{B}} P_B/(P\delta_i))|\mathcal{B}|}{\big(\sum_{i\in\mathcal{H}} 1/\delta_i^2\big)t}) = l, & (5.36)\\
& AW(1 - \sum_{i\in\mathcal{B}} \frac{P_B}{P\delta_i})|\mathcal{B}|/\big(\sum_{i\in\mathcal{H}} \frac{1}{\delta_i^2}\big) > l, & (5.37)\\
& \mathcal{H} = \{1,\cdots,K\}\backslash\mathcal{B}.
\end{aligned}$$

Similar as in problem **P5.1**, the LHS of (5.36) is monotonically increasing in t, and therefore t can be solved numerically using e.g. the bisection method. The difference

is that here $t = \max_{k\in\mathcal{H}} t_k$ only needs to be evaluated once for given $\mathcal{B}$, while in **P5.1** we need to evaluate t_k for all $k \in \mathcal{H}$. Problem **P5.3**' is again a combinatorial problem and the size of the search space is $\mathcal{O}(2^K)$. We make the following assumption on problem **P5.3**'.

Assumption 2. *We assume that the reader transmit power P/M is sufficient to enable all transmitters operating in the BS mode, i.e., $P \geq \sum_{i=1}^{K} P_B/\delta_i$.*

Here since $\beta_k^* = P_B/(P\delta_k)$ for $k \in \mathcal{B}$, and $\sum_{i=1}^{K} \beta_k \leq 1$, which results in $P \geq \sum_{i=1}^{K} P_B/\delta_i$. Assumption 2 guarantees that $\mathcal{B}$ can take any subset of $\{1, \cdots, K\}$ including the entire set itself. Unlike the case of Assumption 1 for **P5.1**, if Assumption 2 does not hold, then **P5.3** cannot be reduced to an equivalent problem with Assumption 2 satisfied since the power allocation on the reader makes the problem much more complicated. However Assumption 2 is a weak assumption, and when it holds we can show the following theorem. The proof is given in Appendix 5.8.9.

Theorem 8. *Under the optimal solution to problem **P5.3**', $\delta_j \geq \delta_i$ should hold for $j \in \mathcal{H}, i \in \mathcal{B}$.*

Theorem 8 guarantees that the $\mathcal{H}$ transmitters must have greater δ_k values than the $\mathcal{B}$ transmitters. Thus we propose Alg. 5.2 to solve **P5.3**'. Alg. 5.2 first sorts all transmitters according to δ_k. At iteration i the groups are set as shown in Step 1, and the algorithm checks the feasibility constraint in (5.37) based on β given in Step 1. It then evaluates and stores the total transmission time based on the group assignment. The minimum transmission time and optimal grouping can be found from these evaluations. Alg. 5.2 has linear time complexity $\mathcal{O}(K)$ which is significantly improved from the exhaustive search.

5.5.3 Massive MIMO with Realistic Transmitters

Now we study the system with massive MIMO reader and realistic transmitters, where the power consumption model in (5.4) is considered for the HTT transmit-

Algorithm 5.2 - Algorithm for Solving P5.3 (and P5.4)

Input: $\{\delta_1, \cdots, \delta_K\}$;

Initialization: Sort the transmitters by $\delta_1 \leq \cdots \leq \delta_K$; $t_{total} = [0, \cdots, 0]$;

For $i = 1$ **to** $K - 1$ **Do:**

1: Let $\mathcal{B} = \{1, \cdots, i\}$ and $\mathcal{H} = \{i + 1, \cdots, K\}$;

2: **If** (5.37) is satisfied (or (5.42) for **P5.4**):

3: Calculate $t_{total}[i] = i \times \tau + t$ where t satisfies (5.36) (or (5.48) for **P5.4**);

End

3: find $t_{min} = \min(t_{total})$ and $i^* = \text{argmin}(t_{total})$;

Output: $\mathcal{B} = \{1, \cdots, i^*\}, \mathcal{H} = \{i^* + 1, \cdots, K\}$, minimum time t_{min}, β_k^* given by (5.34) (or (5.45) for **P5.4**) for $k \in \mathcal{H}$, and $\beta_k^* = P_B/(P\delta_k)$ for $k \in \mathcal{B}$.

ters. Redefine $A_k = \frac{\eta\tau PM\delta_k^2}{WN_0}$, $C_k = \frac{a\delta_k M}{WN_0}$, $D_k = \frac{v_k\delta_k M}{WN_0}$. Based on (5.28) and (5.4), the available power for active transmission is $\rho_k = (P\eta\tau\delta_k\beta_k|\mathcal{B}| - ar_kt_k - v_kt_k) = WN_0(A_k\beta_k|\mathcal{B}| - C_kr_kt_k - D_kt_k)$, and r_k should satisfy the following equation

$$r_k = W\log(1 + \frac{A_k\beta_k|\mathcal{B}|}{t_k} - C_kr_k - D_k). \tag{5.38}$$

Define $\tilde{g}_k(t_k) = t_kr_k$. We have the following result. The proof is similar to that of Prop. 2 and thus omitted.

Proposition 4. *$\tilde{g}_k(t_k)$ is concave in t_k for $t_k > 0$, and it has a unique maximizer $t_k^* > 0$ which satisfies*

$$\frac{1}{C_kW} - \tilde{U}_k(t_k^*) + \frac{\tilde{U}_k(t_k^*)}{1 + \tilde{U}_k(t_k^*)}\frac{A_k\beta_k|\mathcal{B}|}{C_kWt_k^*} - C_kD_k = 0, \tag{5.39}$$

where $\tilde{U}_k(t_k) = W_0[\frac{1}{C_kW}\exp\{\frac{1}{C_kW}(1 + \frac{A_k\beta_k|\mathcal{B}|}{t_k} - D_k)\}]$.

Hence the problem formulation under the realistic case is given by

$$\mathbf{P5.4}: \min_{\mathcal{B}\subset\{1,\cdots,K\},\{\beta_1,\cdots,\beta_K\}} |\mathcal{B}|\tau + \max_{k\in\mathcal{H}} t_k \tag{5.40}$$

$$\text{s.t.} \quad \tilde{g}_k(t_k) = l, \quad k \in \mathcal{H}, \tag{5.41}$$

$$\tilde{g}_k(t_k^*) > l, t_k < t_k^*, \quad k \in \mathcal{H}, \tag{5.42}$$

$$P\beta_k\delta_k \geq P_B, \qquad k \in \mathcal{B},$$

$$\sum_{i=1}^{K} \beta_i = 1, \quad \mathcal{H} = \{1,\cdots,K\}\backslash\mathcal{B}.$$

Same as the ideal case in Section 5.5.2, the optimal power allocation for BS transmitters is given by $\beta_k = P_B/(P\delta_k)$, and the $\mathcal{H}$ transmitters will share the rest $\beta_H = 1 - \sum_{i\in\mathcal{B}} P_B/(P\delta_i)$ portion of power. In the next theorem we present the result on optimal power allocation for $\mathcal{H}$ transmitters. The proof is given in Appendix 5.8.10.

Theorem 9. *To minimize the maximum transmission time for given $\mathcal{H}$ transmitters, all transmitters should have the same transmission time t. The optimal transmission rate of all $\mathcal{H}$ transmitters is given by*

$$r^*(t) = W(-\frac{\Omega}{\Theta} - W_0[\frac{\Phi}{\Theta}\exp\{-\frac{\Omega}{\Theta}\}]), \tag{5.43}$$

where

$$\Omega = \sum_{k\in\mathcal{H}} \frac{D_k - 1}{A_k|\mathcal{B}|} - \frac{\beta_H}{t}, \quad \Theta = W\sum_{k\in\mathcal{H}} \frac{C_k}{A_k|\mathcal{B}|}, \quad \Phi = \sum_{k\in\mathcal{H}} \frac{1}{A_k|\mathcal{B}|}. \tag{5.44}$$

The optimal power allocation is given by

$$\beta_k^*(t) = \frac{t(C_k r^*(t) + D_k + e^{\frac{r^*(t)}{W}} - 1)}{A_k|\mathcal{B}|}. \tag{5.45}$$

Based on Theorem 9, **P5.4** can be simplified. Define $\hat{g}(t) = tr^*(t)$, and similar to Prop. 2 and Prop. 4, it can be shown that $\hat{g}_k(t)$ has unique maximizer t^* which satisfies $r^*(t^*) - t^*W\frac{1-\beta_H}{\Theta(t^*)^2}(1 + W_0[\frac{\Phi}{\Theta}\exp\{-\frac{\Omega}{\Theta}\}])^{-1} = 0$. Therefore the problem

becomes

$$\mathbf{P5.4}': \quad \min_{\mathcal{B}\subset\{1,\cdots,K\}} \quad |\mathcal{B}|\tau + t \tag{5.46}$$

$$\text{s.t.} \quad \hat{g}(t) = l, \tag{5.47}$$

$$\hat{g}(t^*) > l, t < t^*, \tag{5.48}$$

$$\mathcal{H} = \{1, \cdots, K\}\backslash\mathcal{B}.$$

In **P5.4**' t is the root of (5.47) and can be solved numerically. Due to the complexity of $\hat{g}(t)$, it is hard to analyze it or verify if Theorem 8 still holds for the realistic case. Nevertheless, we can employ the linear search based Alg. 5.2 to solve **P5.4**'. This is because **P5.4**' has very similar formulation as **P5.3**', and the main difference is just the constraint on t. The only change that needs to make is to modify Step 2 where t now satisfies (5.47), and the algorithm solves **P5.4**' in linear time.

5.6 Simulation Results

5.6.1 Results for Single Antenna Reader

The simulation setup is given as the following. The default number of transmitters is $K = 30$, and their distances to the reader d_k are uniformly distributed between 10 to 15 meters. The transmitters operate in the UHF band with carrier frequency $f_C = 915$ MHz, and the system bandwidth is $W = 10$ kHz for HTT transmission. The path loss is given by $\delta_k = (\frac{\lambda}{4\pi d_k})^2$, where $\lambda = c/f_C$. The input power is $P_C = 5$ W and the energy conversion efficiency is $\eta = 0.2$. The default data packet size is 20 kb, and the backscattering transmission rate is $r_B = 80$ kbps, which results in the length of time slot to be $\tau = 0.25$ s. The tag sensitivity is set as $P_B = 1 \times 10^{-7}$ W. For the realistic transmitter case, the power consumption coefficients are $a = 1 \times 10^{-9}$ W/bit and $v_k = 1 \times 10^{-5}$ mW. All the results are averaged over 100 realizations of transmitter location distribution.

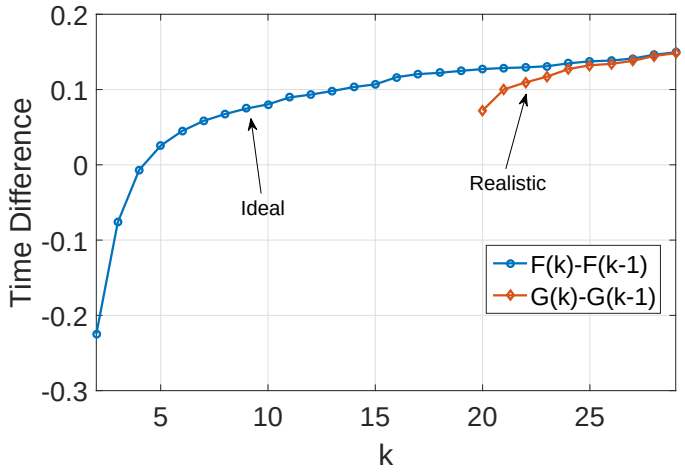

Figure 5.3: Illustration of Theorem 4 and 6.

We first illustrate Theorems 4 and 6 via simulations. In Fig. 5.3, we plot $F(k) - F(k-1)$ for the ideal case and $G(k) - G(k-1)$ for the realistic case for a specific realization, where $F(k)$ and $G(k)$ are defined in (5.17) and (5.27) respectively. It can be seen that both curves increase as k increases, as stated by Theorems 4 and 6. In this example, the optimal k for the ideal case is 4 since $F(4) - F(3) < 0$ and $F(5) - F(4) > 0$, i.e., transmitters 1 to 4 are in the BS group while the remaining transmitters are in the HTT group. On the other hand, the optimal k for the realistic case is 20, and for smaller k the corresponding problem **P5.2** is infeasible.

In Fig. 5.4 we plot the total transmission time against the input power, and two values of τ are compared as well. It can be observed that in all cases the total transmission time decreases as the input power increases. This is because higher input power enables higher power transfer and energy harvesting, which then lead to higher transmission rate and shorter time for the HTT transmission. Moreover, the gaps between ideal cases and realistic cases become smaller as P_C increases. This is because when the input power is low, higher portion of the harvested energy is spent on rate dependent and other fixed power consumptions, and the power available for active transmission is low. Hence the gap is large for low input power. As P_C becomes

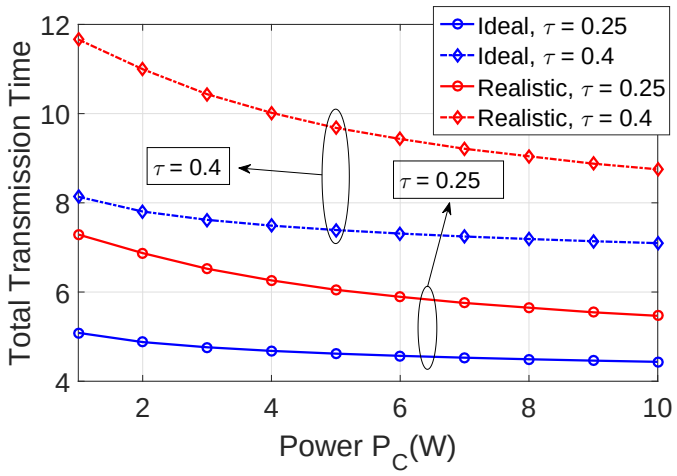

Figure 5.4: Total transmission time versus input power.

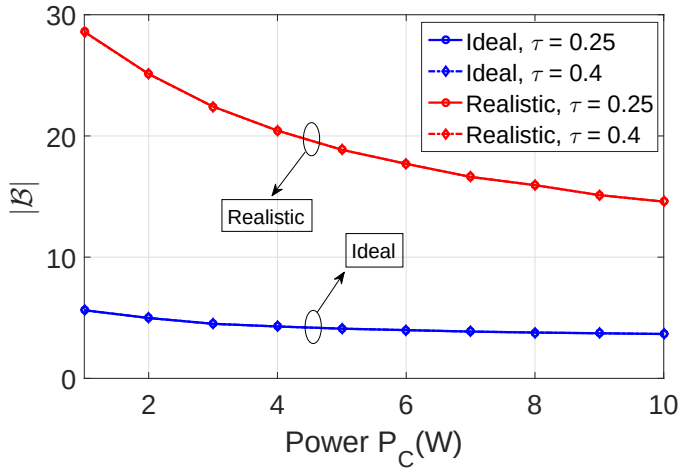

Figure 5.5: Number of BS transmitters versus input power.

higher, the portion of power for active transmission increases, hence the difference between the realistic case and ideal case becomes smaller. On the other hand, the transmission time for $\tau = 0.4$ is longer than that for $\tau = 0.25$ as expected, since when $\tau = 0.4$ the transmitters have larger packages to transmit, hence it takes longer time. It can be observed that the total transmission time for $\tau = 0.4$ is about 1.6 times longer than that for $\tau = 0.25$, which is the ratio of the corresponding τ's as $0.4/0.25 = 1.6$. From another point of view, we plot the number of BS transmitters $|\mathcal{B}|$

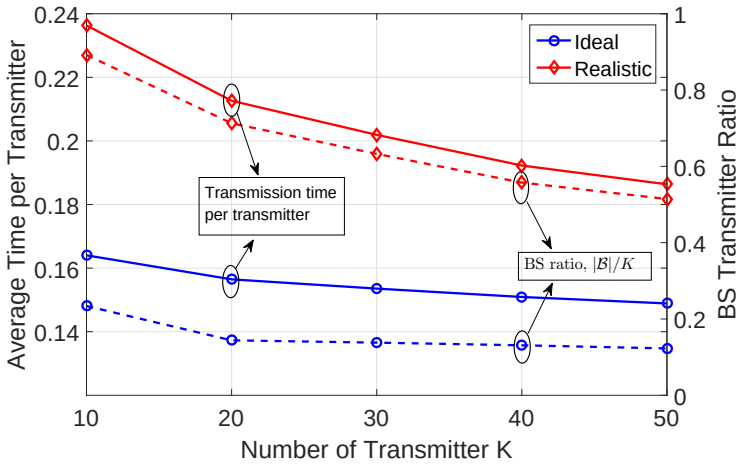

Figure 5.6: System performance versus number of transmitters.

versus the input power in Fig. 5.5. It shows that $|\mathcal{B}|$ is almost the same for $\tau = 0.4$ and $\tau = 0.25$ for both ideal and realistic cases. This result illustrates that $\mathcal{B}$ is insensitive to the size of the transmission packages, and explains why the total transmission time is proportional to τ. On the other hand, $|\mathcal{B}|$ decreases as P_C increases. This is because when the input power becomes large, the HTT transmitters can harvest "too much" energy for the same $\mathcal{B}$, and the system performance can be improved if we move some transmitters from the BS group to the HTT group, since these switched transmitters now take shorter transmission time than τ while the transmission times of the other HTT transmitters remain the same.

In Fig. 5.6, we evaluate the average transmission time per transmitter, which is defined as the total transmission time divided by K, versus number of transmitters. It can be observed that the average transmission time per transmitter decreases as K increases. This is because the ratio of the BS transmitter $|\mathcal{B}|/K$ decreases when K becomes large, which can also be observed in Fig. 5.6. Due to Lemma 4, the HTT transmitters always have shorter transmission time, hence lower ratio results in lower average transmission time. Therefore in practice, the system shows better performance per transmitter when K is large, where the HTT phase takes the majority

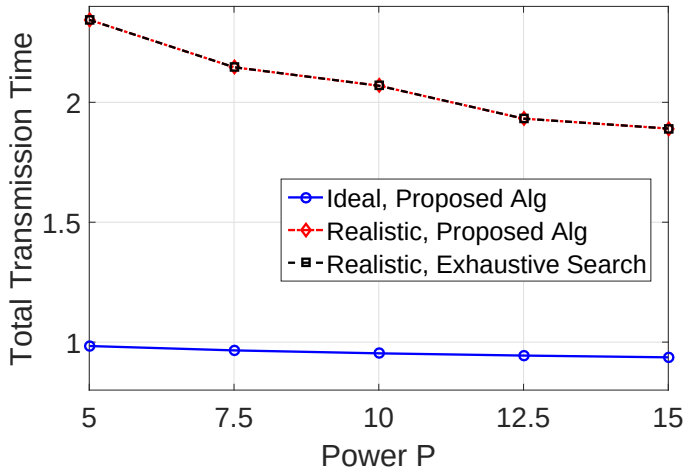

Figure 5.7: Total transmission time versus input power for massive MIMO reader.

of the time, while the BS mode is dominant when K is small.

5.6.2 Results for Massive MIMO Reader

In the massive MIMO setting, the backscatter transmission rate is 100 kbps, and the package size is 25 kb. The system bandwidth is 2 kHz. For realistic transmitters, we have $a = 2 \times 10^{-10}$. The number of antennas is $M = 200$. All the remaining parameters are the same as those in Section 5.6.1.

We first show the result on the total transmission time versus the input power in Fig. 5.7. In this simulation, the number of transmitters is $K = 8$. Similar to the single antenna case, we also observe that for both ideal and realistic transmitters, the total transmission time decreases as P increases. The difference of both cases decreases as P increases, since when P is large higher portion of its harvested power can be utilized for transmission, resulting in performance that is closer to that of the ideal transmitter. To check the optimality of the Alg. 5.2 for realistic transmitters, we also find the optimal transmission time using the exhaustive search. It can be seen that the result of the proposed algorithm overlaps with that found by exhaustive search, indicating that Alg. 5.2 is a near-optimal algorithm to solve **P5.4**.

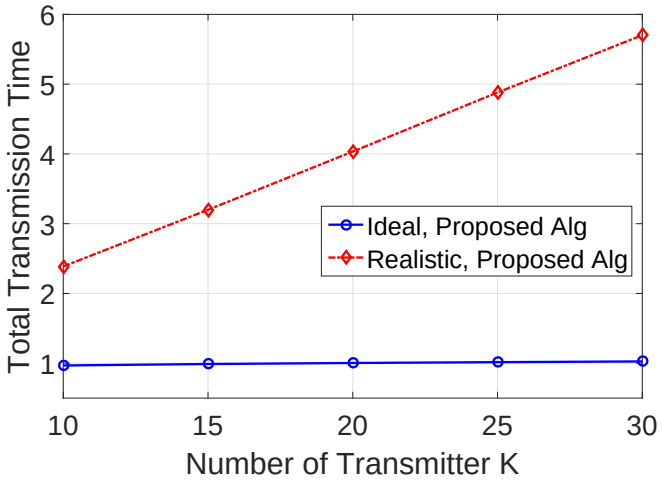

Figure 5.8: Total transmission time versus number of transmitters for massive MIMO reader.

We then show the total transmission time versus number of transmitters in Fig. 5.8. In this simulation the input power is $P = 10$ W. It can be seen that the transmission time increases almost linearly as K increases. However, the average transmission time per transmitter decreases as K increases, especially for ideal transmitters. Specifically, when $K = 10$ the average transmission time is 0.097 and 0.239 second for the ideal and realistic cases respectively. They decease to 0.034 and 0.19 second when $K = 30$. Hence, for the system with massive MIMO reader increasing K can also improve the per-transmitter efficiency.

5.7 Conclusions

This paper studied the transmission time minimization problem for systems with hybrid backscatter-HTT transmitters. The transmitters in this network can operate in either the backscatter mode or the harvest-then-transmit (HTT) mode. Both ideal and realistic transmitter power consumption models are considered. We proved that, under both models, the optimal transmission time of each HTT transmitter can be

calculated, and it is convex and decreasing in the number of backscatter transmitters. We then proved that the difference in the objective function is increasing. Based on these results, we proposed a bisection based algorithm to find the optimal transmitter grouping and total transmission time. Finally we extended the results to the case of massive MIMO reader.

5.8 Appendices

5.8.1 Proof of Proposition 1

We have the first- and second-order derivatives of $f_k(t_k)$ in (5.12) as $f_k'(t_k) = W(\log(1+\frac{A_k|\mathcal{B}|}{t_k}) - \frac{A_k|\mathcal{B}|}{t_k+A_kW|\mathcal{B}|})$, and $f_k''(t_k) = W(\frac{A_k|\mathcal{B}|}{(t_k+A_k|\mathcal{B}|)^2} - \frac{A_k|\mathcal{B}|}{t_k(t_k+A_k|\mathcal{B}|)})$. It can be easily seen that $f_k''(t_k) < 0$ for $t_k > 0$ with given $A_k > 0$, hence $f_k'(t_k)$ is monotonically decreasing for $t_k > 0$. Also by L'Hopital's rule, $\lim_{t_k\to+\infty} \frac{\log(1+\frac{A_k|\mathcal{B}|}{t_k}))}{\frac{A_k|\mathcal{B}|}{t_k+A_k|\mathcal{B}|}} = \lim_{t_k\to+\infty}(\frac{A_k|\mathcal{B}|/(A_k|\mathcal{B}|t_k+t_k^2)}{A_k|\mathcal{B}|/(t_k+A_k|\mathcal{B}|)^2} = \frac{t_k+A_k|\mathcal{B}|}{t_k}) > 1$. Thus, $\lim_{t_k\to+\infty} f_k'(t_k) > 0$, and we have $f_k'(t_k) > 0$ for $t_k > 0$, which means that $f_k(t_k)$ is monotonically increasing.

On the other hand, $\lim_{t_k\to0} f_k(t_k) = \lim_{t_k\to0} W\frac{\log(1+A_k|\mathcal{B}|/t_k)}{1/t_k} = \lim_{t_k\to0} W\frac{A_k|\mathcal{B}|t_k}{t_k+A_k|\mathcal{B}|}$, thus $\lim_{t_k\to0} f_k(t_k) = 0$. Similarly $\lim_{t_k\to+\infty} f_k(t_k) = \lim_{t_k\to+\infty} W\frac{\log(1+A_k|\mathcal{B}|/t_k)}{1/t_k} = A_kW|\mathcal{B}|$ by L'Hopital's rule. Hence $f_k(t_k)$ increases from 0 and converges to $A_kW|\mathcal{B}|$.

5.8.2 Proof of Lemma 6

Given $\varrho_k(t,x) = l$, we can express x in terms of t as

$$x = \varphi_k(t) = \frac{(e^{l/(tW)}-1)t}{A_k}. \tag{5.49}$$

Taking the first- and second-order derivatives of $\varphi_k(t)$ and after some manipulations, we have

$$\varphi_k'(t) = \frac{1}{A_k}(e^{l/(tW)}(1-\frac{l}{tW})-1), \tag{5.50}$$

$$\varphi_k''(t) = \frac{l^2}{A_kt^3W^2}e^{l/(tW)}. \tag{5.51}$$

It can be seen that $\varphi_k''(t) > 0$, hence $\phi_k(t)$ is convex and $\varphi_k'(t)$ is monotonically increasing. We can further show that $\lim_{t\to+\infty} \varphi_k'(t) = \lim_{t\to+\infty} \frac{1}{A_k}(-\frac{l}{tW}e^{l/(tW)}) = \lim_{t\to+\infty} -\frac{1}{A_k}e^{l/(tW)} = -\frac{1}{A_k}$ by L'Hopital's rule. Hence, $\varphi_k'(t) < 0$ for all t and $\varphi_k(t)$ is monotonically decreasing. Using this result, it can further be shown that its inverse function, $\phi_k(x) = \varphi_k^{-1}(x) = t$, has $\phi_k'(\varphi_k(t)) = 1/\varphi_k'(t) < 0$ and $\phi_k''(t) = -\varphi_k''(t)/(\varphi_k'(t))^3 > 0$. Hence ϕ_k is convex and decreasing in x.

On the other hand, in the proof of Lemma 5 we have shown that, for $|h_k|^2 > |h_{k'}|^2$, $t_k < t_{k'}$ where $f_k(t_k) = f_{k'}(t_{k'}) = l$. Since $f_k(t_k) = \varrho_k(t_k, |\mathcal{B}|)$, it follows that $\phi_k(|\mathcal{B}|) = t_k < t_{k'} = \phi_{k'}(|\mathcal{B}|)$.

5.8.3 Proof of Theorem 4

By Lemma 6, we can express the objective function in (5.14) as a function of k, the number of transmitters in $\mathcal{B}$, as shown (5.17). Then, we have

$$\begin{aligned} F(k+1) - F(k) &= (k+1)\tau + \sum_{i=k+2}^{K} \phi_i(k+1) - k\tau - \sum_{i=k+1}^{K} \phi_i(k) \\ &= \tau - \phi_{k+1}(k) + \sum_{i=k+2}^{K} (\phi_i(k+1) - \phi_i(k)), \qquad (5.52) \\ F(k) - F(k-1) &= k\tau + \sum_{i=k+1}^{K} \phi_i(k) - (k-1)\tau - \sum_{i=k}^{K} \phi_i(k-1) \\ &= \tau - \phi_k(k-1) + \phi_{k+1}(k) - \phi_{k+1}(k-1) + \\ &\quad \sum_{i=k+2}^{K} (\phi_i(k) - \phi_i(k-1)), \qquad (5.53) \end{aligned}$$

and we want to show that the difference of the RHS of (5.53) and (5.52) is greater than 0. By Lemma 6, $\phi_i(x)$ is convex in x, hence $\frac{1}{2}(\phi_i(k+1) + \phi_i(k-1)) \geq \phi_i(k)$, i.e., $\phi_i(k+1) - \phi_i(k) \geq \phi_i(k) - \phi_i(k-1)$, and thus

$$\sum_{i=k+2}^{K} (\phi_i(k+1) - \phi_i(k)) \geq \sum_{i=k+2}^{K} (\phi_i(k) - \phi_i(k-1)). \qquad (5.54)$$

On the other hand,

$$\tau-\phi_{k+1}(k)-(\tau-\phi_k(k-1)+\phi_{k+1}(k)-\phi_{k+1}(k-1)) = \phi_k(k-1)-\phi_{k+1}(k)-(\phi_{k+1}(k)-\phi_{k+1}(k-1)). \tag{5.55}$$

By Lemma 6, $\phi_i(x)$ is monotonically decreasing, and $\phi_{k+1}(k) - \phi_{k+1}(k-1) < 0$. Also by Lemma 6, given $|h_{k+1}|^2 > |h_k|^2$, we have $\phi_k(k-1) \geq \phi_{k+1}(k-1) \geq \phi_{k+1}(k)$. These lead to the conclusion that (5.55) is always negative. Hence, substituting this result and (5.54) into (5.52) and (5.53), yields $F(k+1) - F(k) > F(k) - F(k-1)$. This completes the proof.

5.8.4 Proof of Theorem 5

Transforming (5.9) into

$$r_k = \frac{\alpha_k(q_k - v_k)}{a}, \tag{5.56}$$

and equating the RHS of (5.56) and (5.6), we have

$$W\log(1+\frac{(1-\alpha_k)(A_k|\mathcal{B}|-D_kt_k)}{t_k}) = \frac{\alpha_k(A_k|\mathcal{B}|-D_kt_k)WC_k}{t_k}.$$

After some manipulations, we have

$$\begin{aligned} C_k(1+\frac{(1-\alpha_k)(A_k|\mathcal{B}|-D_kt_k)}{t_k})\exp\{C_k(1+\frac{(1-\alpha_k)(A_k|\mathcal{B}|-D_kt_k)}{t_k})\} \\ = C_k\exp\{C_k(1+\frac{A_k|\mathcal{B}|}{t_k}-D_k)\}. \end{aligned} \tag{5.57}$$

According to the definition of the Lambert function, we have

$$W_0[C_k\exp\{C_k(1+\frac{A_k|\mathcal{B}|}{t_k})-D_k\}] = C_k(1+\frac{(1-\alpha_k)(A_k|\mathcal{B}|-D_kt_k)}{t_k}). \tag{5.58}$$

Solving (5.58) for α_k yields (5.18). Substituting (5.18) into (5.6) gives

$$r_k = W\log\big(\frac{1}{C_k}W_0[C_k\exp\{C_k(1+\frac{A_k|\mathcal{B}|}{t_k}-D_k)\}]\big). \tag{5.59}$$

Using the property that $\log(W_0(x)) = \log(x) - W_0(x)$, (5.59) can be rewritten as

$$\begin{aligned} r_k &= W\big(\log(1/C_k) + \log(C_k) + C_k(1 + \frac{A_k|\mathcal{B}|}{t_k} - D_k) - \\ &\quad W_0[C_k \exp\{C_k(1 + \frac{A_k|\mathcal{B}|}{t_k} - D_k)\}]\big) \\ &= W\big(C_k(1 + \frac{A_k|\mathcal{B}|}{t_k} - D_k) - W_0[C_k \exp\{C_k(1 + \frac{A_k|\mathcal{B}|}{t_k} - D_k)\}]\big), \end{aligned}$$

which is (5.19).

5.8.5 Proof of Proposition 2

Using (5.20) and (5.21), and the derivative expression of the Lambert function $W_0'(x) = \frac{W_0(x)}{x(1+W_0(x))}$ [110], we can write the first- and second-order derivatives of $g_k(t_k)$ as

$$g_k'(t_k) = W(C_k - C_kD_k - U_k(t_k) + \frac{U_k(t_k)}{1+U_k(t_k)}\frac{A_kC_k|\mathcal{B}|}{t_k}), \tag{5.60}$$

$$\begin{aligned} g_k''(t_k) &= W(\frac{U_k(t_k)}{1+U_k(t_k)}\frac{A_kC_k|\mathcal{B}|}{t_k^2} - \frac{U_k(t_k)}{1+U_k(t_k)}\frac{A_kC_k|\mathcal{B}|}{t_k^2} - \frac{U_k(t_k)}{(1+U_k(t_k))^3}\frac{A_k^2C_k^2|\mathcal{B}|^2}{t_k^3}), \\ &= -\frac{A_k^2C_k^2|\mathcal{B}|W}{t_k^3}\frac{U_k(t_k)}{(1+U_k(t_k))^3}. \end{aligned}$$

Since $U_k(t_k) > 0$, $g_k''(t_k) < 0$ for $t_k > 0$, and hence $g_k(t_k)$ is concave in t_k for $t_k > 0$.

The function $g_k(t_k)$ is maximized when its first order derivative is 0. To show that $g_k'(t_k) = 0$ exists for $t_k > 0$, we will show that $\lim_{t_k\to 0} g_k'(t_k) > 0$ and $\lim_{t_k\to\infty} g_k'(t_k) < 0$. Since $\lim_{t_k\to 0} \frac{A_k|\mathcal{B}|}{t_k} - D_k \to \infty$ by (5.20), $\lim_{t_k\to 0} U_k(t_k) \to \infty$, thus $\lim_{t_k\to 0} U_k(t_k)/(1+U_k(t_k)) \to 1$. Also because $W_0(x)$ is monotonically increasing, $\lim_{t_k\to 0} U_k(t_k) < \lim_{t_k\to 0} W_0[(C_k(1 + \frac{A_k|\mathcal{B}|}{t_k} - D_k)) \exp\{C_k(1 + \frac{A_k|\mathcal{B}|}{t_k} - D_k)\}]$. Then we have

$$\begin{aligned} \lim_{t_k\to 0} g_k'(t_k) &= \lim_{t_k\to 0} W(C_k + \frac{A_kC_k|\mathcal{B}|}{t_k} - C_kD_k - U_k(t_k)) \\ &> \lim_{t_k\to 0} W(C_k + \frac{A_kC_k|\mathcal{B}|}{t_k} - C_kD_k - W_0[(C_k(1 + \frac{A_k|\mathcal{B}|}{t_k} - D_k)) \times \\ &\quad \exp\{C_k(1 + \frac{A_k|\mathcal{B}|}{t_k} - D_k)\}]) \\ &= \lim_{t_k\to 0} W(C_k + \frac{A_kC_k|\mathcal{B}|}{t_k} - C_kD_k - C_k(1 + \frac{A_k|\mathcal{B}|}{t_k} - D_k)) \qquad (5.61) \\ &= 0, \end{aligned}$$

where (5.61) is due to the identity $W_0(xe^x) = x$ for $x > 0$. On the other hand, $\lim_{t_k\to\infty} \frac{A_k|\mathcal{B}|}{t_k} - D_k < 0$ and $\lim_{t_k\to\infty} U_k(t_k) > \lim_{t_k\to 0} W_0[(C_k(1 + \frac{A_k|\mathcal{B}|}{t_k} - D_k)) \exp\{C_k(1 + \frac{A_k|\mathcal{B}|}{t_k} - D_k)\}]$. Also, since $U_k(t_k)/(1 + U_k(t_k)) < 1$, we have

$$\begin{aligned}
\lim_{t_k\to\infty} g_k'(t_k) &< \lim_{t_k\to\infty} W(C_k + \frac{A_k C_k|\mathcal{B}|}{t_k} - C_k D_k - U_k(t_k)) \\
&< \lim_{t_k\to\infty} W(C_k + \frac{A_k C_k|\mathcal{B}|}{t_k} - C_k D_k - W_0[C_k(1 + \frac{A_k|\mathcal{B}|}{t_k} - D_k) \times \\
&\quad \exp\{C_k(1 + \frac{A_k|\mathcal{B}|}{t_k} - D_k)\}]) \\
&= 0.
\end{aligned}$$

Therefore $g_k'(t_k) = 0$ exists for $t_k > 0$ and this completes the proof.

5.8.6 Proof of Lemma 7

We write r_k^* in (5.19) as a function of $|h_k|^2$, i.e.,

$$r_k^*(|h_k|^2) = W(\frac{\tilde{C}}{|h_k|^2} + \tilde{A}_k|h_k|^2 - \tilde{D}_k - \tilde{U}_k(|h_k|^2))$$

where $\tilde{A}_k = \frac{\eta\tau P_C|\mathcal{B}|}{at_kW}$, $\tilde{C} = N_0/a$, $\tilde{D}_k = \frac{v_k}{aW}$, and $\tilde{U}_k(|h_k|^2) = W_0[\frac{\tilde{C}}{|h_k|^2}\exp\{\frac{\tilde{C}}{|h_k|^2} + \tilde{A}_k|h_k|^2 - \tilde{D}_k\}]$. Take the derivative of r_k^* we have

$$\begin{aligned}
r_k^{*\prime}(|h_k|^2) &= W(-\frac{\tilde{C}}{|h_k|^4} + \tilde{A}_k - \frac{\tilde{U}_k(|h_k|^2)}{1 + \tilde{U}_k(|h_k|^2)}(-\frac{1}{|h_k|^2} - \frac{\tilde{C}}{|h_k|^4} + \tilde{A}_k)) \\
&= \frac{W}{|h_k|^2(1 + \tilde{U}_k(|h_k|^2))}(\tilde{U}_k(|h_k|^2) - \frac{\tilde{C}}{|h_k|^2} + \tilde{A}_k|h_k|^2). \qquad (5.62)
\end{aligned}$$

Since $q_k = \tilde{A}_k|h_k|^2aW > v_k = \tilde{D}_kaW$ in (5.24), we have $\tilde{A}_k|h_k|^2 - \tilde{D}_k > 0$, and hence

$$\begin{aligned}
\tilde{U}_k(|h_k|^2) &= W_0[\frac{\tilde{C}}{|h_k|^2}\exp\{\frac{\tilde{C}}{|h_k|^2}\}\exp\{\tilde{A}_k|h_k|^2 - \tilde{D}_k\}] \\
&> W_0[\frac{\tilde{C}}{|h_k|^2}\exp\{\frac{\tilde{C}}{|h_k|^2}\}\}] \qquad (5.63) \\
&= \frac{\tilde{C}}{|h_k|^2}, \qquad (5.64)
\end{aligned}$$

where (5.63) holds because $\exp\{\tilde{A}_k|h_k|^2 - \tilde{D}_k\} > 1$ and $W_0(x)$ is monotonically increasing. Substitute (5.64) into (5.62) and we have $r^{*\prime}(|h_k|^2) > \frac{W\tilde{A}_k|h_k|^2}{|h_k|^2(1+\tilde{U}_k(|h_k|^2))} > 0$. Therefore r_k^* is monotonically increasing in $|h_k|^2$.

Apply this result and follow the proof of Lemma 5, it can be shown that $t_i \leq t_j$ for $|h_i|^2 \geq |h_j|^2$, and under the optimal solution of problem **P5.2**' we have $|h_i|^2 \geq |h_j|^2$ with $i \in \mathcal{H}, j \in \mathcal{B}$.

5.8.7 Proof of Lemma 8

The implicit function theorem [111] states that for (t, x) that satisfies $\kappa_k(t, x) = l$ and if $\partial\mu(t, x)/\partial t \neq 0$, then t can be expressed as a continuous function of x. In problem **P5.2**', we have $\partial\mu_k(t, x)/\partial t = C_k - V_k(t, x) + \frac{V_k(t,x)}{1+V_k(t,x)}\frac{A_kC_kx}{t} - C_kD_k$, and t should satisfy $\partial\mu_k(t, x)/\partial t > 0$ according to (5.25). Then by the implicit function theorem, t can be expressed as a continuous function of x, $\psi_k(x)$. Intuitively the result in this case can be understood as the following. Function $\mu_k(t, x)$ is monotonically increasing in t, and it is not hard to verify that $\mu_k(t, x)$ is increasing in x as well. Thus there is a one-to-one mapping between t and x, and t can be considered as a function of x. In fact the proof of Lemma 6 can be regarded as a special case of the implicit function theorem, where we are able to find the analytic expression of t in terms of x due to the simple functional form of the ideal model.

Now we replace t with $\psi_k(x)$ in $\mu_k(t, x)$ and find its first order implicit derivative by taking derivative w.r.t. x on both sides of $\mu_k(\psi_k(x), x) = l$. After some manipulations, we have

$$\begin{aligned} 0 \;=\; & \frac{\partial\psi_k(x)}{\partial x}\big(C_k - C_kD_k - V_k(\psi_k(x), x) + \frac{V_k(\psi_k(x), x)}{(1 + V_k(\psi_k(x), x))}\frac{A_kC_kx}{\psi_k(x)}\big) + \\ & A_kC_k(1 - \frac{V_k(\psi_k(x), x)}{(1 + V_k(\psi_k(x), x))}). \end{aligned} \tag{5.65}$$

Solving for $\partial\psi_k(x)/\partial x$ yields

$$\frac{\partial\psi_k(x)}{\partial x} = \frac{-A_kC_k}{(1+V_k(\psi_k(x),x))(C_k - C_kD_k - V_k(\psi_k(x),x) + \frac{V_k(\psi_k(x),x)}{(1+V_k(\psi_k(x),x))}\frac{A_kC_kx}{\psi_k(x)})} < 0, \tag{5.66}$$

since the denominator is always positive by (5.25). Hence $\psi_k(x)$ is monotonically decreasing. Similarly taking the second-order implicit derivative and after some manipulations, we have

$$\begin{aligned} & (\frac{A_kC_k}{\psi_k(x)} - \frac{A_kC_kx}{(\psi_k(x))^2}\frac{\partial\psi_k(x)}{\partial x})\big(\frac{V_k(\psi_k(x),x)A_kC_k}{(1+V_k(\psi_k(x),x))^3}(\frac{x}{\psi_k(x)}\frac{\partial\psi_k(x)}{\partial x} - 1)\big) \\ = & -\frac{\partial^2\psi_k(x)}{\partial x^2}(C_k - C_kD_k - V_k(\psi_k(x),x) + \frac{V_k(\psi_k(x),x)}{(1+V_k(\psi_k(x),x))}\frac{A_kC_kx}{\psi_k(x)}). \end{aligned}$$

Solving for $\partial^2\psi_k(x)/\partial x^2$ yields

$$\frac{\partial^2\psi_k(x)}{\partial x^2} = \frac{V_k(\psi_k(x),x)A_k^2C_k^2\psi_k(x)(\frac{1}{\psi_k(x)} - \frac{x}{\psi_k(x)^2}\frac{\partial\psi_k(x)}{\partial x})^2}{(1+V_k(\psi_k(x),x))^3(C_k - C_kD_k - V_k(\psi_k(x),x) + \frac{V_k(\psi_k(x),x)}{(1+V_k(\psi_k(x),x))}\frac{A_kC_kx}{\psi_k(x)})} > 0. \tag{5.67}$$

Hence $\psi_k(x)$ is convex.

On the other hand, by Lemma 7 we can show that, for $|h_k|^2 > |h_{k'}|^2$, $t_k < t_{k'}$ where $g_k(t_k) = g_{k'}(t_{k'}) = l$. Since $g_k(t_k) = \mu_k(t_k, |\mathcal{B}|)$, it follows that $\psi_k(|\mathcal{B}|) = t_k < t_{k'} = \psi_{k'}(|\mathcal{B}|)$.

5.8.8 Proof of Theorem 7

For given $\mathcal{H}$, to minimize the maximum transmission time for the $\mathcal{H}$ transmitters, the transmission time of all transmitters should be the same, i.e., $t_i(\beta_i) = t, \forall i \in \mathcal{H}$. This can be proved by contradiction. Suppose there is an optimal solution $\{\tilde{\beta}_k : k \in \mathcal{H}\}$ such that $t_i < t_j, i \neq j$, where $\tilde{f}_i(t_i, \tilde{\beta}_i) = \tilde{f}_j(t_j, \tilde{\beta}_j) = l$. By Prop. 3 $\tilde{f}_k(t_k, \beta_k)$ increases in β_k for given t_k, then for $\Delta > 0$ we have $\tilde{f}_i(t_i, \tilde{\beta}_i - \Delta) < l$. Also since $\tilde{f}_k(t_k, \beta_k)$ increases in t_k for given β_k, there exists $\epsilon_i > 0$ such that $\tilde{f}_i(t_i, \tilde{\beta}_i - \Delta) < \tilde{f}_i(t_i + \epsilon_i, \tilde{\beta}_i - \Delta) = l$, as long as $\tilde{f}_i$ is feasible for $\tilde{\beta}_i - \Delta$, i.e., $AW(\tilde{\beta}_i - \Delta)|\mathcal{B}| > l$. Similarly, we also have $\tilde{f}_j(t_j, \tilde{\beta}_j + \Delta) > \tilde{f}_j(t_j - \epsilon_j, \tilde{\beta}_j + \Delta) = l$ for a $\epsilon_j > 0$, and it

leads to

$$\tilde{f}_i(t_i, \tilde{\beta}_i - \Delta) < \tilde{f}_i(t_i + \epsilon_i, \tilde{\beta}_i - \Delta) = l = \tilde{f}_j(t_j - \epsilon_j, \tilde{\beta}_j + \Delta) < \tilde{f}_j(t_j, \tilde{\beta}_j + \Delta).$$

Therefore, the new power allocation $\beta_i^* = \tilde{\beta}_i - \Delta$ and $\beta_j^* = \tilde{\beta}_j + \Delta$ will result in a lower maximum transmission time as $t_j - \epsilon_j$, which contradicts with the assumption that $\{\tilde{\beta}_i, \tilde{\beta}_j\}$ are optimal power allocation coefficients. Hence, the optimal transmission time of all transmitters should be the same.

Then, it can be seen that to achieve the same t_k for all $k \in \mathcal{H}$, all HTT transmitters should receive the same amount of power, i.e., $AW\delta_i^2\beta_i|\mathcal{B}| = AW\delta_j^2\beta_j|\mathcal{B}|,\ i \neq j$. Hence, by solving the linear system

$$\begin{aligned} \delta_k^2\beta_k &= \delta_i^2\beta_i, \quad i,k \in \mathcal{H} \\ \sum_{i\in\mathcal{H}} \beta_i &= \beta_H, \end{aligned}$$

it can be shown that $\beta_i = \delta_k^2\beta_k/\delta_i^2$, and it further leads to the optimal power allocation in (5.34).

5.8.9 Proof of Theorem 8

Let j be the transmitter with the lowest channel gain in the HTT group, i.e., $\delta_j \leq \delta_{j'}, j, j' \in \mathcal{H}$. We show that if there is $i \in \mathcal{B}$ such that $\delta_i > \delta_j$, then switching the groups of i and j will result in a shorter transmission time. Using (5.35) and (5.36), the total transmission time before switching their groups is given by $|\mathcal{B}|\tau + t_1$ where t_1 satisfies $Wt_1\log(1 + \frac{A\beta_1|\mathcal{B}|}{t_1}) = l$ and

$$\beta_1 = \frac{1 - \sum_{k\in\mathcal{B}} P_B/(E\delta_k)}{\sum_{k\in\mathcal{H}} 1/\delta_k^2} = \frac{\Lambda - P_B/(E\delta_i)}{\Upsilon + 1/\delta_j^2}, \tag{5.68}$$

where $\Lambda = 1 - \sum_{k\in\mathcal{B},k\neq i} P_B/(E\delta_k)$ and $\Upsilon = \sum_{k\in\mathcal{H},k\neq j} 1/\delta_k^2$. After switching their groups, the total transmission time is $|\mathcal{B}|\tau + t_2$ where t_2 satisfies $Wt_2\log(1 + \frac{A\beta_2|\mathcal{B}|}{t_2}) = l$ and

$$\beta_2 = \frac{\Lambda - P_B/(E\delta_j)}{\Upsilon + 1/\delta_i^2}. \tag{5.69}$$

After switching, the time difference is $t_2 - t_1$. By Prop. 3, $\tilde{f}_k(t_k, \beta_k)$ increases in t_k and β, hence it can be shown that t_k decreases as β_k increases when (t_k, β_k) satisfy $\tilde{f}_k(t_k, \beta_k) = l$. Since $\tilde{f}_k(t_k, \beta_k)$ and $t\log(1 + \frac{A\beta|\mathcal{B}|}{t})$ has almost the same functional form, they have the same properties as well. Hence t decreases as β increases when (t, β) satisfies $t\log(1 + \frac{A\beta|\mathcal{B}|}{t}) = l$. Thus, here to show $t_2 < t_1$ we just need to prove $\beta_2 > \beta_1$.

$$\begin{aligned}
\beta_2 - \beta_1 &= \frac{\Lambda - P_B/(E\delta_j)}{\Upsilon + 1/\delta_i^2} - \frac{\Lambda - P_B/(E\delta_i)}{\Upsilon + 1/\delta_j^2} && (5.70)\\
&= \frac{\delta_i^2(\Lambda - \frac{P_B}{E\delta_j})}{\delta_i^2\Upsilon + 1} - \frac{\delta_j^2(\Lambda - \frac{P_B}{E\delta_i})}{\delta_j^2\Upsilon + 1} && (5.71)\\
&= \frac{\Lambda(\delta_i^2 - \delta_j^2) - \frac{P_B}{E}\Upsilon\delta_i\delta_j(\delta_i - \delta_j) - \frac{P_B}{E}(\frac{\delta_i^2}{\delta_j} - \frac{\delta_j^2}{\delta_i})}{(\delta_i^2\Upsilon + 1)(\delta_j^2\Upsilon + 1)} && (5.72)\\
&= \frac{\Lambda E\delta_i\delta_j(\delta_i + \delta_j) - P_B\Upsilon\delta_i^2\delta_j^2 - P_B(\delta_i^2 + \delta_i\delta_j + \delta_j^2)}{E\delta_i\delta_j(\delta_i - \delta_j)(\delta_i^2\Upsilon + 1)(\delta_j^2\Upsilon + 1)}. && (5.73)
\end{aligned}$$

Since $\delta_i > \delta_j$, we simply need to show that the numerator in (5.73) is greater than 0, i.e.,

$$\delta_i\delta_j(\delta_i + \delta_j)(E - P_B\sum_{k\in\mathcal{B},k\neq i}\frac{1}{\delta_k}) - P_B\sum_{k\in\mathcal{H},k\neq j}\frac{\delta_i^2\delta_j^2}{\delta_k^2} - P_B(\delta_i^2 + \delta_i\delta_j + \delta_j^2) > 0. \quad (5.74)$$

Because $\delta_j \leq \delta_k$ for $k \in \mathcal{H}$, $\delta_i\delta_j < \delta_i\delta_k < \delta_j\delta_k + \delta_i\delta_k$, and we have $\frac{\delta_i^2\delta_j^2}{\delta_k^2} < \frac{\delta_i\delta_j(\delta_i+\delta_j)\delta_k}{\delta_k^2} = \frac{\delta_i\delta_j(\delta_i+\delta_j)}{\delta_k}$. Also $P_B(\delta_i^2 + \delta_i\delta_j + \delta_j^2) < P_B(\delta_i^2 + 2\delta_i\delta_j + \delta_j^2) = P_B(\frac{1}{\delta_i} + \frac{1}{\delta_j})\delta_i\delta_j(\delta_i + \delta_j)$. Hence,

$$\begin{aligned}
&\delta_i\delta_j(\delta_i + \delta_j)(E - P_B\sum_{k\in\mathcal{B},k\neq i}\frac{1}{\delta_k}) - P_B\sum_{k\in\mathcal{H},k\neq j}\frac{\delta_i^2\delta_j^2}{\delta_k^2} - P_B(\delta_i^2 + \delta_i\delta_j + \delta_j^2)\\
>\ &\delta_i\delta_j(\delta_i + \delta_j)(E - P_B\sum_{k\in\mathcal{B},k\neq i}\frac{1}{\delta_k}) - P_B\sum_{k\in\mathcal{H},k\neq j}\frac{\delta_i\delta_j(\delta_i + \delta_j)}{\delta_k} - P_B(\frac{1}{\delta_i} + \frac{1}{\delta_j})\delta_i\delta_j(\delta_i + \delta_j)\\
=\ &\delta_i\delta_j(\delta_i + \delta_j)\big(E - P_B(\sum_{k\in\mathcal{B},k\neq i}\frac{1}{\delta_k} + \sum_{k\in\mathcal{H},k\neq j}\frac{1}{\delta_k} + \frac{1}{\delta_i} + \frac{1}{\delta_j})\big) && (5.75)\\
=\ &\delta_i\delta_j(\delta_i + \delta_j)\big(E - P_B(\sum_{k=1}^{K}\frac{1}{\delta_k})\big), && (5.76)
\end{aligned}$$

and due to Assumption 2, $E \geq \sum_{k=1}^{K} \frac{P_B}{\delta_k}$, and (5.76) is non-negative. Hence (5.74) holds, and $\beta_2 - \beta_1 > 0$, which means that switching the groups of i and j always brings in shorter transmission time. Therefore for optimal solution to **P5.3**', $\delta_j > \delta_i$ should hold for $j \in \mathcal{H}$ and $i \in \mathcal{B}$. This completes the proof.

5.8.10 Proof of Theorem 9

Using the same approach as in Theorem 5, we have the transmission rate given by

$$r_k = W \log(\frac{W}{C_k} W_0[\frac{W}{C_k} \exp\{1 + \frac{A_k \beta_k |\mathcal{B}|}{t_k} - D_k\}]). \tag{5.77}$$

It can be seen that r_k increases as β_k increases, hence $\tilde{g}_k(t_k, \beta_k) = t_k r_k$ increases in β_k as well. It also can be shown that $\tilde{g}_k$ increases in t_k for $t_k \in (0, t_k^*)$ by following the proof in Prop. 2. Hence, by using the same techniques as the proof of Theorem 7, we can show that all HTT transmitters should have the same transmission time $t_k = t$ when the optimal achieves. In other words, they should have the same transmission rate $r_k = r^*$ for $k \in \mathcal{H}$, where r^* is optimal.

To solve for r^*, we substitute $t_k = t$ and $r_k = r^*$ into (5.38) and it yields (5.45). Taking (5.45) into $\sum_{k \in \mathcal{H}} \beta_k = \beta_H$, and after some manipulations, we have

$$\frac{\Theta}{W} r^* e^{-r^*/W} + \Omega e^{-r^*/W} = -\Phi, \tag{5.78}$$

where Θ, Ω, Φ are given in (5.44), which further leads to

$$(-\frac{\Omega}{\Theta} - \frac{r^*}{W}) e^{-\frac{r^*}{W} - \frac{\Omega}{\Theta}} = \frac{\Phi}{\Theta} e^{-\frac{\Omega}{\Theta}}. \tag{5.79}$$

Taking advantage of the Lambert function, we have

$$W_0[\frac{\Phi}{\Theta} e^{-\frac{\Omega}{\Theta}}] = -\frac{\Omega}{\Theta} - \frac{r^*}{W}. \tag{5.80}$$

Solving (5.80) for r^* yields (5.43).

Chapter 6

Conclusions

Motivated by the rapid development of wireless power transfer (WPT) and backscatter communication technologies the and rising demand of the Internet of Things and wireless sensor networks applications, we focused on designing wireless power transfer and backscatter communications systems to make the best use of the limited RF power resources. In this thesis, we proposed algorithms for the following backscatter communication and WPT systems:

- multi-antenna backscatter reader with blind adaptive beamforming
- wireless power transfer by beamspace MIMO with lens antenna array
- energy allocation and utilization for wireless powered networks
- time scheduling in wireless powered backscatter communication networks

By proposing these systems and algorithms, we aim to make the WPT and backscatter communication system operate in an feasible and efficient way, making the best use of the limited RF and time resource and providing reliable and high-efficient wireless power transfer and communication services.

Bibliography

[1] J. Gozalvez, "New 3GPP standard for IoT [mobile radio]," *IEEE Vehicular Technology Magazine*, vol. 11, no. 1, pp. 14–20, March 2016.

[2] X. Mou and H. Sun, "Wireless power transfer: Survey and roadmap," in *2015 IEEE 81st Vehicular Technology Conference (VTC Spring)*, May 2015, pp. 1–5.

[3] Z. Popović, E. A. Falkenstein, D. Costinett, and R. Zane, "Low-power far-field wireless powering for wireless sensors," *Proceedings of the IEEE*, vol. 101, no. 6, pp. 1397–1409, June 2013.

[4] Z. Ding, C. Zhong, D. W. K. Ng, M. Peng, H. A. Suraweera, R. Schober, and H. V. Poor, "Application of smart antenna technologies in simultaneous wireless information and power transfer," *IEEE Communications Magazine*, vol. 53, no. 4, pp. 86–93, April 2015.

[5] B. Kellogg, A. Parks, S. Gollakota, J. R. Smith, and D. Wetherall, "Wi-Fi backscatter: Internet connectivity for RF-powered devices," in *Proceedings of the 2014 ACM Conference on SIGCOMM*, ser. SIGCOMM '14. New York, NY, USA: ACM, 2014, pp. 607–618. [Online]. Available: http://doi.acm.org/10.1145/2619239.2626319

[6] D. M. Dobkin, *the RF in RFID: Passive UHF RFID in Practice.* Elsevier, 2008.

[7] K. Finkenzeller, *RFID Handbook: Fundamentals and Applications in Contactless Smart Cards and Identification*, 2nd ed. New York: Wiley, 2003.

[8] H. Vogt, "Efficient object identification with passive RFID tags," in *Pervasive Computing*, F. Mattern and M. Naghshineh, Eds. Berlin, Heidelberg: Springer Berlin Heidelberg, 2002, pp. 98–113.

[9] R. Want, "An introduction to RFID technology," *IEEE Pervasive Computing*, vol. 5, no. 1, pp. 25–33, Jan 2006.

[10] V. Liu, A. Parks, V. Talla, S. Gollakota, D. Wetherall, and J. R. Smith, "Ambient backscatter: Wireless communication out of thin air," *SIGCOMM Comput. Commun. Rev.*, vol. 43, no. 4, pp. 39–50, Aug. 2013. [Online]. Available: http://doi.acm.org/10.1145/2534169.2486015

[11] N. Van Huynh, D. T. Hoang, X. Lu, D. Niyato, P. Wang, and D. I. Kim, "Ambient backscatter communications: A contemporary survey," *IEEE Communications Surveys Tutorials*, vol. 20, no. 4, pp. 2889–2922, Fourthquarter 2018.

[12] V. Talla, M. Hessar, B. Kellogg, A. Najafi, J. R. Smith, and S. Gollakota, "LoRa backscatter: Enabling the vision of ubiquitous connectivity," *Proc. ACM Interact. Mob. Wearable Ubiquitous Technol.*, vol. 1, no. 3, pp. 105:1–105:24, Sep. 2017. [Online]. Available: http://doi.acm.org/10.1145/3130970

[13] H. J. Visser and R. J. M. Vullers, "RF energy harvesting and transport for wireless sensor network applications: Principles and requirements," *Proceedings of the IEEE*, vol. 101, no. 6, pp. 1410–1423, June 2013.

[14] P. Blasco, D. Gunduz, and M. Dohler, "A learning theoretic approach to energy harvesting communication system optimization," *IEEE Transactions on Wireless Communications*, vol. 12, no. 4, pp. 1872–1882, April 2013.

[15] H. Dinh Thai, D. Niyato, P. Wang, D. I. Kim, and Z. Han, "The tradeoff analysis in RF-powered backscatter cognitive radio networks," in *2016 IEEE Global Communications Conference (GLOBECOM)*, Dec 2016, pp. 1–6.

[16] D. T. Hoang, D. Niyato, P. Wang, and D. I. Kim, "Optimal time sharing in RF-powered backscatter cognitive radio networks," in *2017 IEEE International Conference on Communications (ICC)*, May 2017, pp. 1–6.

[17] S. Gong, X. Huang, J. Xu, W. Liu, P. Wang, and D. Niyato, "Backscatter relay communications powered by wireless energy beamforming," *IEEE Transactions on Communications*, vol. 66, no. 7, pp. 3187–3200, July 2018.

[18] X. Lu, G. Li, H. Jiang, D. Niyato, and P. Wang, "Performance analysis of wireless-powered relaying with ambient backscattering," in *2018 IEEE International Conference on Communications (ICC)*, May 2018, pp. 1–6.

[19] S. H. Kim and D. I. Kim, "Hybrid backscatter communication for wireless-powered heterogeneous networks," *IEEE Transactions on Wireless Communications*, vol. 16, no. 10, pp. 6557–6570, Oct 2017.

[20] N. V. Huynh, D. T. Hoang, D. N. Nguyen, E. Dutkiewicz, D. Niyato, and P. Wang, "Reinforcement learning approach for RF-powered cognitive radio network with ambient backscatter," in *2018 IEEE Global Communications Conference (GLOBECOM)*, Dec 2018, pp. 1–6.

[21] R. Kishore, S. Gurugopinath, P. C. Sofotasios, S. Muhaidat, and N. Al-Dhahir, "Opportunistic ambient backscatter communication in RF-powered cognitive radio networks," *IEEE Transactions on Cognitive Communications and Networking*, vol. 5, no. 2, pp. 413–426, June 2019.

[22] R. S. Khasgiwale, R. U. Adyanthaya, and D. W. Engels, "Extracting information from tag collisions," in *2009 IEEE International Conference on RFID*, April 2009, pp. 131–138.

[23] J. Park, J. Jung, S. Ahn, H. Roh, H. Oh, Y. Seong, Y. Lee, and K. Choi, "Extending the interrogation range of a passive UHF RFID system with an external continuous wave transmitter," *IEEE Transactions on Instrumentation and Measurement*, vol. 59, no. 8, pp. 2191–2197, Aug 2010.

[24] P. V. Nikitin, D. D. Arumugam, M. J. Chabalko, B. E. Henty, and D. D. Stancil, "Long range passive UHF RFID system using HVAC ducts," *Proceedings of the IEEE*, vol. 98, no. 9, pp. 1629–1635, Sep. 2010.

[25] D. Kim, H. Jo, H. Yoon, C. Mun, B. Jang, and J. Yook, "Reverse-link interrogation range of a UHF MIMO-RFID system in nakagami- m fading channels," *IEEE Transactions on Industrial Electronics*, vol. 57, no. 4, pp. 1468–1477, April 2010.

[26] J. D. Griffin and G. D. Durgin, "Gains for RF tags using multiple antennas," *IEEE Transactions on Antennas and Propagation*, vol. 56, no. 2, pp. 563–570, Feb 2008.

[27] Y. Z. G. Zhang and W. Kang, "Low-complexity channel estimation for fhe UHF MIMO-RFID systems with optimal training," *Int. J. of Advancements in Computing Technology*, vol. 4, no. 1, pp. 387–394, Jan 2012.

[28] E. Denicke, M. Henning, H. Rabe, and B. Geck, "The application of multiport theory for MIMO RFID backscatter channel measurements," in *2012 42nd European Microwave Conference*, Oct 2012, pp. 522–525.

[29] C. Angerer, R. Langwieser, and M. Rupp, "RFID reader receivers for physical layer collision recovery," *IEEE Transactions on Communications*, vol. 58, no. 12, pp. 3526–3537, December 2010.

[30] F. Schoute, "Dynamic frame length ALOHA," *IEEE Transactions on Communications*, vol. 31, no. 4, pp. 565–568, April 1983.

[31] L. Zhu and T. P. Yum, "The optimal reading strategy for EPC gen-2 RFID anti-collision systems," *IEEE Transactions on Communications*, vol. 58, no. 9, pp. 2725–2733, Sep. 2010.

[32] C. Wang, M. Daneshmand, K. Sohraby, and B. Li, "Performance analysis of RFID generation-2 protocol," *IEEE Transactions on Wireless Communications*, vol. 8, no. 5, pp. 2592–2601, May 2009.

[33] W. Chen, "An accurate tag estimate method for improving the performance of an RFID anticollision algorithm based on dynamic frame length ALOHA," *IEEE Transactions on Automation Science and Engineering*, vol. 6, no. 1, pp. 9–15, Jan 2009.

[34] Jae-Ryong Cha and Jae-Hyun Kim, "Novel anti-collision algorithms for fast object identification in RFID system," in *11th International Conference on Parallel and Distributed Systems (ICPADS'05)*, vol. 2, July 2005, pp. 63–67.

[35] H. Wu and Y. Zeng, "Bayesian tag estimate and optimal frame length for anti-collision ALOHA RFID system," *IEEE Transactions on Automation Science and Engineering*, vol. 7, no. 4, pp. 963–969, Oct 2010.

[36] B. C. Banister and J. R. Zeidler, "A simple gradient sign algorithm for transmit antenna weight adaptation with feedback," *IEEE Transactions on Signal Processing*, vol. 51, no. 5, pp. 1156–1171, May 2003.

[37] X. W. K. Dong, N. Prasad and S. Zhu, "Adaptive antenna selection and Tx/Rx beamforming for large-scale MIMO systems in 60 ghz channels," *EURASIP J. Wireless Commun. and Network*, vol. 59, Aug 2011.

[38] E. Inc. EPC radio-frequency identity protocols class-1 generation-2 UHF RFID protocol for communications at 860 mhz – 960 mhz version 1.2.0. [Online]. Available: http://www.epcglobalinc.org

[39] Daeyoung Kim, M. A. Ingram, and W. W. Smith, "Measurements of small-scale fading and path loss for long range RF tags," *IEEE Transactions on Antennas and Propagation*, vol. 51, no. 8, pp. 1740–1749, Aug 2003.

[40] E. G. Larsson, O. Edfors, F. Tufvesson, and T. L. Marzetta, "Massive MIMO for next generation wireless systems," *IEEE Communications Magazine*, vol. 52, no. 2, pp. 186–195, February 2014.

[41] S. Kashyap, E. Björnson, and E. G. Larsson, "On the feasibility of wireless energy transfer using massive antenna arrays," *IEEE Transactions on Wireless Communications*, vol. 15, no. 5, pp. 3466–3480, May 2016.

[42] Y. Zeng and R. Zhang, "Optimized training design for wireless energy transfer," *IEEE Transactions on Communications*, vol. 63, no. 2, pp. 536–550, Feb 2015.

[43] J. Li, H. Zhang, D. Li, and H. Chen, "On the performance of wireless-energy-transfer-enabled massive MIMO systems with superimposed pilot-aided channel estimation," *IEEE Access*, vol. 3, pp. 2014–2027, 2015.

[44] A. Li and C. Masouros, "Energy-efficient SWIPT: From fully digital to hybrid analog–digital beamforming," *IEEE Transactions on Vehicular Technology*, vol. 67, no. 4, pp. 3390–3405, April 2018.

[45] Y. Zeng, B. Clerckx, and R. Zhang, "Communications and signals design for wireless power transmission," *IEEE Transactions on Communications*, vol. 65, no. 5, pp. 2264–2290, May 2017.

[46] L. Wang, M. Elkashlan, R. W. Heath, M. D. Renzo, and K. Wong, "Millimeter wave power transfer and information transmission," in *2015 IEEE Global Communications Conference (GLOBECOM)*, Dec 2015, pp. 1–6.

[47] T. A. Khan, A. Alkhateeb, and R. W. Heath, "Millimeter wave energy harvesting," *IEEE Transactions on Wireless Communications*, vol. 15, no. 9, pp. 6048–6062, Sept 2016.

[48] G. N. Kamga and S. Aïssa, "Wireless power transfer in mmWave massive MIMO systems with/without rain attenuation," *IEEE Transactions on Communications*, pp. 1–1, 2018.

[49] M. Nariman, F. Shirinfar, A. P. Toda, S. Pamarti, A. Rofougaran, and F. D. Flaviis, "A compact 60-GHz wireless power transfer system," *IEEE Transactions on Microwave Theory and Techniques*, vol. 64, no. 8, pp. 2664–2677, Aug 2016.

[50] R. Zhang and C. K. Ho, "MIMO broadcasting for simultaneous wireless information and power transfer," *IEEE Transactions on Wireless Communications*, vol. 12, no. 5, pp. 1989–2001, May 2013.

[51] E. Boshkovska, D. W. K. Ng, N. Zlatanov, and R. Schober, "Practical nonlinear energy harvesting model and resource allocation for SWIPT systems," *IEEE Communications Letters*, vol. 19, no. 12, pp. 2082–2085, Dec 2015.

[52] S. Wang, M. Xia, K. Huang, and Y. Wu, "Wirelessly powered two-way communication with nonlinear energy harvesting model: Rate regions under fixed and mobile relay," *IEEE Transactions on Wireless Communications*, vol. 16, no. 12, pp. 8190–8204, Dec 2017.

[53] R. Zhang and C. K. Ho, "MIMO broadcasting for simultaneous wireless information and power transfer," *IEEE Transactions on Wireless Communications*, vol. 12, no. 5, pp. 1989–2001, May 2013.

[54] F. Yuan, S. Jin, Y. Huang, K. k. Wong, Q. T. Zhang, and H. Zhu, "Joint wireless information and energy transfer in massive distributed antenna systems," *IEEE Communications Magazine*, vol. 53, no. 6, pp. 109–116, June 2015.

[55] X. Chen, Z. Zhang, H. h. Chen, and H. Zhang, "Enhancing wireless information and power transfer by exploiting multi-antenna techniques," *IEEE Communications Magazine*, vol. 53, no. 4, pp. 133–141, April 2015.

[56] G. Yang, C. K. Ho, R. Zhang, and Y. L. Guan, "Throughput optimization for massive MIMO systems powered by wireless energy transfer," *IEEE Journal on Selected Areas in Communications*, vol. 33, no. 8, pp. 1640–1650, Aug 2015.

[57] L. Zhao, X. Wang, and K. Zheng, "Downlink hybrid information and energy transfer with massive MIMO," *IEEE Transactions on Wireless Communications*, vol. 15, no. 2, pp. 1309–1322, Feb 2016.

[58] J. Brady, N. Behdad, and A. M. Sayeed, "Beamspace MIMO for millimeter-wave communications: System architecture, modeling, analysis, and measurements," *IEEE Transactions on Antennas and Propagation*, vol. 61, no. 7, pp. 3814–3827, July 2013.

[59] Y. Zeng and R. Zhang, "Millimeter wave MIMO with lens antenna array: A new path division multiplexing paradigm," *IEEE Transactions on Communications*, vol. 64, no. 4, pp. 1557–1571, April 2016.

[60] O. E. Ayach, S. Rajagopal, S. Abu-Surra, Z. Pi, and R. W. Heath, "Spatially sparse precoding in millimeter wave MIMO systems," *IEEE Transactions on Wireless Communications*, vol. 13, no. 3, pp. 1499–1513, March 2014.

[61] X. Gao, L. Dai, Z. Chen, Z. Wang, and Z. Zhang, "Near-optimal beam selection for beamspace MmWave massive MIMO systems," *IEEE Communications Letters*, vol. 20, no. 5, pp. 1054–1057, May 2016.

[62] X. Gao, L. Dai, S. Han, C. L. I, and X. Wang, "Reliable beamspace channel estimation for millimeter-wave massive MIMO systems with lens antenna array," *IEEE Transactions on Wireless Communications*, vol. 16, no. 9, pp. 6010–6021, Sept 2017.

[63] Y. Zeng, L. Yang, and R. Zhang, "Multi-user millimeter wave MIMO with full-dimensional lens antenna array," *IEEE Transactions on Wireless Communications*, vol. 17, no. 4, pp. 2800–2814, April 2018.

[64] H. Dai, Y. Liu, G. Chen, X. Wu, T. He, A. X. Liu, and H. Ma, "Safe charging for wireless power transfer," *IEEE/ACM Transactions on Networking*, vol. 25, no. 6, pp. 3531–3544, Dec 2017.

[65] H. Zou, T. Hastie, and R. Tibshirani, "Sparse principal component analysis," *Journal of Computational and Graphical Statistics*, vol. 15, no. 2, pp. 265–286, 2006. [Online]. Available: https://doi.org/10.1198/106186006X113430

[66] A. d'Aspremont, L. E. Ghaoui, M. I. Jordan, and G. R. G. Lanckriet, "A direct formulation for sparse PCA using semidefinite programming," *SIAM Review*, vol. 49, no. 3, pp. 434–448, 2007. [Online]. Available: https://doi.org/10.1137/050645506

[67] A. d'Aspremont, F. Bach, and L. E. Ghaoui, "Optimal solutions for sparse principal component analysis," *Journal of Machine Learning Research*, vol. 9, pp. 1269–1294, 2008.

[68] X.-T. Yuan and T. Zhang, "Truncated power method for sparse eigenvalue problems," *Journal of Machine Learning Research*, vol. 14, no. 1, pp. 899–925, Apr. 2013. [Online]. Available: http://dl.acm.org/citation.cfm?id=2502581.2502610

[69] M. Grant and S. Boyd, "CVX: Matlab software for disciplined convex programming, version 2.1," http://cvxr.com/cvx, Mar. 2014.

[70] C. Eckart and G. Young, "The approximation of one matrix by another of lower rank," *Psychometrika*, vol. 1, no. 3, pp. 211–218, Sep 1936. [Online]. Available: https://doi.org/10.1007/BF02288367

[71] R. M. P.-A. Absil and R. Sepulchre, *Optimization Algorithms on Matrix Manifolds*. Princeton, NJ: Princeton University Press, 2007.

[72] S. E. Selvan, U. Amato, K. A. Gallivan, C. Qi, M. F. Carfora, M. Larobina, and B. Alfano, "Descent algorithms on oblique manifold for source-adaptive ICA contrast," *IEEE Transactions on Neural Networks and Learning Systems*, vol. 23, no. 12, pp. 1930–1947, Dec. 2012.

[73] S. Xu, "Smoothing method for minimax problems," *Computational Optimization and Applications*, vol. 20, no. 3, pp. 267–279, 2001.

[74] W. W. Hager and H. Zhang, "A survey of nonlinear conjugate gradient methods," *Pacific Journal of Optimization*, vol. 2, no. 1, pp. 38–58, 2006.

[75] T. Bai and R. W. Heath, "Coverage analysis for millimeter wave cellular networks with blockage effects," in *2013 IEEE Global Conference on Signal and Information Processing*, Dec 2013, pp. 727–730.

[76] T. A. Khan, A. Yazdan, and R. W. Heath, "Optimization of power transfer efficiency and energy efficiency for wireless-powered systems with massive MIMO," *IEEE Transactions on Wireless Communications*, vol. 17, no. 11, pp. 7159–7172, Nov 2018.

[77] S. Sudevalayam and P. Kulkarni, "Energy harvesting sensor nodes: Survey and implications," *IEEE Communications Surveys Tutorials*, vol. 13, no. 3, pp. 443–461, Third 2011.

[78] J. A. Paradiso and T. Starner, "Energy scavenging for mobile and wireless electronics," *IEEE Pervasive Computing*, vol. 4, no. 1, pp. 18–27, Jan 2005.

[79] P. S. Khairnar and N. B. Mehta, "Discrete-rate adaptation and selection in energy harvesting wireless systems," *IEEE Transactions on Wireless Communications*, vol. 14, no. 1, pp. 219–229, Jan 2015.

[80] C. K. Ho and R. Zhang, "Optimal energy allocation for wireless communications with energy harvesting constraints," *IEEE Transactions on Signal Processing*, vol. 60, no. 9, pp. 4808–4818, Sept 2012.

[81] M. Kashef and A. Ephremides, "Optimal packet scheduling for energy harvesting sources on time varying wireless channels," *Journal of Communications and Networks*, vol. 14, no. 2, pp. 121–129, April 2012.

[82] P. Castiglione, O. Simeone, E. Erkip, and T. Zemen, "Energy management policies for energy-neutral source-channel coding," *IEEE Transactions on Communications*, vol. 60, no. 9, pp. 2668–2678, September 2012.

[83] S. Mao, M. H. Cheung, and V. W. S. Wong, "Joint energy allocation for sensing and transmission in rechargeable wireless sensor networks," *IEEE Transactions on Vehicular Technology*, vol. 63, no. 6, pp. 2862–2875, July 2014.

[84] B. Gurakan, O. Ozel, J. Yang, and S. Ulukus, "Energy cooperation in energy harvesting communications," *IEEE Transactions on Communications*, vol. 61, no. 12, pp. 4884–4898, December 2013.

[85] Y. Wu, V. K. N. Lau, D. H. K. Tsang, and L. P. Qian, "Energy-efficient delay-constrained transmission and sensing for cognitive radio systems," *IEEE Transactions on Vehicular Technology*, vol. 61, no. 7, pp. 3100–3113, Sept 2012.

[86] R. V. Bhat, M. Motani, and T. J. Lim, "Energy harvesting communication using finite-capacity batteries with internal resistance," *IEEE Transactions on Wireless Communications*, vol. 16, no. 5, pp. 2822–2834, May 2017.

[87] H. Zhang, S. Huang, C. Jiang, K. Long, V. C. M. Leung, and H. V. Poor, "Energy efficient user association and power allocation in millimeter-wave-based ultra dense networks with energy harvesting base stations," *IEEE Journal on Selected Areas in Communications*, vol. 35, no. 9, pp. 1936–1947, Sept 2017.

[88] S. Chen, S. Zhong, S. Yang, and X. Wang, "A multiantenna RFID reader with blind adaptive beamforming," *IEEE Internet of Things Journal*, vol. 3, no. 6, pp. 986–996, Dec 2016.

[89] P. S. Yedavalli, T. Riihonen, X. Wang, and J. M. Rabaey, "Far-field RF wireless power transfer with blind adaptive beamforming for internet of things devices," *IEEE Access*, vol. 5, pp. 1743–1752, 2017.

[90] K. Huang and X. Zhou, "Cutting the last wires for mobile communications by microwave power transfer," *IEEE Communications Magazine*, vol. 53, no. 6, pp. 86–93, June 2015.

[91] A. O. Ercan, O. Sunay, and I. F. Akyildiz, "RF energy harvesting and transfer for spectrum sharing cellular iot communications in 5g systems," *IEEE Transactions on Mobile Computing*, vol. PP, no. 99, pp. 1–1, 2017.

[92] D. Shaviv, A. Özgür, and H. H. Permuter, "Capacity of remotely powered communication," *IEEE Transactions on Information Theory*, vol. 63, no. 3, pp. 1364–1391, March 2017.

[93] L. R. Varshney, "Transporting information and energy simultaneously," in *2008 IEEE International Symposium on Information Theory*, July 2008, pp. 1612–1616.

[94] J. Razavilar, K. J. R. Liu, and S. I. Marcus, "Jointly optimized bit-rate/delay control policy for wireless packet networks with fading channels," *IEEE Transactions on Communications*, vol. 50, no. 3, pp. 484–494, Mar 2002.

[95] M. L. Puterman, *Markov Decision Processes: Discrete Stochastic Dynamic Programming*. New York, NY: Wiley, 2005.

[96] D. P. Bertsekas, *Dynamic programming and optimal control, Vol. 1*, 3rd ed. Belmont, MA: Athena Scientific, 2005.

[97] K. Murota, "On steepest descent algorithms for discrete convex functions," *SIAM Journal on Optimization*, vol. 14, no. 3, pp. 699–707, 2004. [Online]. Available: http://dx.doi.org/10.1137/S1052623402419005

[98] ——, "Convexity and steinitz's exchange property," *Advances in Mathematics*, vol. 124, no. 2, pp. 272 – 310, 1996. [Online]. Available: http://www.sciencedirect.com/science/article/pii/S0001870896900845

[99] W. Feller, *An Introduction to Probability Theory and its Applications*, 3rd ed. New York, NY: Wiley, 1968, vol. I.

[100] S. Boyd and L. Vandenberghe, *Convex Optimization*. Cambridge, UK: Cambridge University Press, 2004.

[101] N. Van Huynh, D. T. Hoang, D. Niyato, P. Wang, and D. I. Kim, "Optimal time scheduling for wireless-powered backscatter communication networks," *IEEE Wireless Communications Letters*, vol. 7, no. 5, pp. 820–823, Oct 2018.

[102] B. Lyu, D. T. Hoang, and Z. Yang, "User cooperation in wireless-powered backscatter communication networks," *IEEE Wireless Communications Letters*, vol. 8, no. 2, pp. 632–635, April 2019.

[103] D. T. Hoang, D. Niyato, P. Wang, D. I. Kim, and L. B. Le, "Overlay RF-powered backscatter cognitive radio networks: A game theoretic approach," in *2017 IEEE International Conference on Communications (ICC)*, May 2017, pp. 1–6.

[104] E. Björnson, L. Sanguinetti, J. Hoydis, and M. Debbah, "Optimal design of energy-efficient multi-user MIMO systems: Is massive MIMO the answer?" *IEEE Transactions on Wireless Communications*, vol. 14, no. 6, pp. 3059–3075, June 2015.

[105] L. Zhao and X. Wang, "Massive MIMO downlink for wireless information and energy transfer with energy harvesting receivers," *IEEE Transactions on Communications*, vol. 67, no. 5, pp. 3309–3322, May 2019.

[106] B. Clerckx, R. Zhang, R. Schober, D. W. K. Ng, D. I. Kim, and H. V. Poor, "Fundamentals of wireless information and power transfer: From RF energy harvester models to signal and system designs," *IEEE Journal on Selected Areas in Communications*, vol. 37, no. 1, pp. 4–33, Jan 2019.

[107] Y. Li, B. Bakkaloglu, and C. Chakrabarti, "A system level energy model and energy-quality evaluation for integrated transceiver front-ends," *IEEE Transactions on Very Large Scale Integration (VLSI) Systems*, vol. 15, no. 1, pp. 90–103, Jan 2007.

[108] E. Björnson, M. Matthaiou, and M. Debbah, "Massive MIMO with non-ideal arbitrary arrays: Hardware scaling laws and circuit-aware design," *IEEE Transactions on Wireless Communications*, vol. 14, no. 8, pp. 4353–4368, Aug 2015.

[109] T. L. Marzetta, "Noncooperative cellular wireless with unlimited numbers of base station antennas," *IEEE Transactions on Wireless Communications*, vol. 9, no. 11, pp. 3590–3600, November 2010.

[110] R. M. Corless, G. H. Gonnet, D. E. G. Hare, D. J. Jeffrey, and D. E. Knuth, "On the lambertw function," *Advances in Computational Mathematics*, vol. 5, no. 1, pp. 329–359, Dec 1996. [Online]. Available: https://doi.org/10.1007/BF02124750

[111] S. G. Krantz and H. R. Parks, *The Implicit Function Theorem, History, Theory, and Applications*. New York, NY: Birkhäuser Basel, 2013.